Hyperpolarized Gas Polarimetry and Imaging at Low Magnetic Field

Thesis by

Tina Pavlin

In Partial Fulfillment of the Requirements
for the Degree of
Doctor of Philosophy

California Institute of Technology
Pasadena, California

2003
(Defended May 20, 2003)

Not Art and Science serve, alone;
Patience must in the work be shown.
A quiet spirit plods and plods at length;
Nothing but time can give the brew its strength.

Johann Wolfgang von Goethe, Faust.

To my parents, Nataša and Martin

Acknowledgements

First and foremost, I would like to thank my advisor, Emlyn Hughes, for his support and guidance throughout my graduate studies. His insistence on planning and scheduling enabled me to finish my Ph.D. studies in 5 years–before being saturated with the subject matter, thus allowing me to pursue my future career with enthusiasm. I am also very grateful to him for providing me with the opportunity to work at Stanford University, where I met many inspiring people and researchers. Steven Conolly made me a part of the Stanford PMRI group by treating me as one of his own students, well beyond his duty. His kindness and patience helped me explore my full potential, and I owe him most of the ideas behind my research. I was extremely fortunate to have worked with Greig Scott, who not only became a good friend by selflessly supporting me through many ups and downs and by being my biking partner, but devoted much of his morning-coffee routine to answering questions about my research and giving me valuable input and encouragement. His immense knowledge, combined with his modest attitude and his commitment to his work were truly admirable. Finally, I owe many thanks to Blaine Chronik, who was a constant source of inspiration by being a model scientist, researcher and teacher. I am very grateful to him for training me to work in the MRI research, and most of all, for sharing with me his thoughts on countless aspects of the scientific career.

I would like to express my thanks to my Ph.D. committee, J. Pine, S. Frautschi and S. Fraser, as well as to Stanford professors, D. Nishimura, J. Pauly and A. Macovski. I furthermore owe a great deal to my former physics professor and advisor, G. Cates, who believed in me and supported my research endeavors since I left Princeton.

Many other people at Caltech were instrumental in my research and my well-being. I am grateful to Dave Pripstein, who trained me during my first year at Caltech and provided a balance to my stressful schedule by hosting dinner parties for the whole group; to Steffen Jensen for his unforgettable wit, advice and support; and to Ray Fuzesy and Faye

Witharm for making the glass cells for my experiments as well as for their dedication and encouragement. I am fortunate to have had the technical help and expertise of Bob Carr, Jim Pendlay, and the Caltech glassblower, Richard Gerhart. I am much in debt to Georgia Frueh, whose efficient handling of all the administrative work made my stay away from Caltech manageable and whose care and concern were motherly like; to Donna Driscoll for always welcoming me with a smile and reassuring words when I showed up at her office door to register for an exam; to Jo-Ann Ruffolo, whose unforgettable enthusiasm made career counselling a joyous experience; to James Boyk for being the best piano teacher; and to the office of the International Student Programs, its staff, and in particular, its director, Parandeh Kia. Parandeh's generous and sincere concern for all students and her reliable character were a true asset to Caltech.

My years at Caltech would not have been as memorable without my fellow students and friends. Many thanks to Klejda for being my girl-confidant and for providing a balance to otherwise man-dominated field; to Mark for always being willing to listen to my lamenting; to Peter for his humor; and to Wenjin and Guodong for answering all my physics questions. I am very grateful to Claudine for letting me stay with her while I was “homeless” at Caltech; to Yasser for working with me on countless problem sets while being a loyal and non-judgmental friend; as well as to Olga, Michele, Andrew, Jason, and the “Yugo-crowd”. I am equally grateful to my fellow students at Stanford: Ross, Sharon, Nate, Neal, Karla, Jin, Juan, Julie and Jong. Special thanks to Katie Crocker for her kind spirit; to Lara Quint for always being a friend; and to my friends in Providence: Monica for all the support and love, Michelle and Irfan, as well as Amin and Newal.

I am very much indebted to Cristina De Zan for helping me grow as a person during my graduate studies, to the Sisson-Coons family, and especially, to the Coker family for their support. Mrs. Coker's home-cooked Turkish delights and her kindness were of great help during my dissertation writing.

I would not have been able to go through my graduate studies were it not for the unconditional love and unwavering support of my family (aunt Ančka!) and, in particular, my parents. I am deeply grateful to them for believing in me, for standing behind my aspirations and dreams, and most of all, for providing me with a loving, warm, and intellectually fulfilling environment. Lastly, I would like to thank Demirkan, the love of my life, for his understanding, patience, and inspiration. I am truly fortunate to have him as my partner in life.

Abstract

MR imaging with polarized noble gases has shown promise in both, biomedical and material's imaging applications. Its advantage over the conventional proton MRI lies in its ability to produce high signal-to-noise ratio (SNR), high-resolution images at low magnetic field strengths. In this work:

1. We implemented and studied in detail two methods for detecting hyperpolarization levels of ^{129}Xe and ^{3}He: NMR (Nuclear Magnetic Resonance) and EPR (Electron Paramagnetic Resonance). The ^{3}He NMR and EPR data allowed for a comparison of these two polarimetry methods, while ^{129}Xe NMR and EPR data showed promise for the calibration of ^{129}Xe EPR shifts.

2. We investigated the possibility of using a *pulsed* resistive low-field MR scanner for spin echo imaging of hyperpolarized gases. By collecting CPMG spin echo trains containing 4096 echoes and lasting over 30 seconds, we demonstrated a high degree of stability for the pulsed resistive low-field scanner.

3. We developed a single-shot PGSE sequence for measuring diffusion coefficients of hyperpolarized gases which removed the effects of background gradients, thus allowing a separation of the T_2^{CPMG} relaxation from diffusion-induced signal loss. The theoretical estimations of ^{3}He and ^{129}Xe diffusion coefficients which were based on the Lennard-Jones potential agreed well with our measured ^{3}He and ^{129}Xe diffusion coefficients within the experimental errors.

4. We determined the inherent T_2 relaxation times of ^{3}He and ^{129}Xe by varying the interecho time in the conventional CPMG spin echo sequence and by modelling the functional dependence of the T_2^{CPMG} relaxation time on the interecho spacing.

5. We collected first ever ^{3}He gradient echo images on a pulsed resistive low-field scanner.

In addition, we modelled numerically the effects of flip-angle, diffusion and relaxation rates on signal decay during gradient echo imaging with hyperpolarized gases.

6. We show, with simulations and experiments, that central ordering of RARE k-space acquisition significantly reduces diffusion-induced signal loss. The 1-D RARE images of ^{3}He show a factor of a 100 improvement in the SNR (for 1.6 mm resolution) when using centrally ordered phase-encode gradients.

Contents

List of Figures

List of Tables

Chapter 1

Introduction

Magnetic resonance imaging (MRI) of pulmonary ventilation using hyperpolarized noble gases (^{3}He and ^{129}Xe) is a promising new method for assessing and monitoring pulmonary disease [6, 7, 8]. High-quality (high-temporal and high-spatial resolution) MR images of animal and human lung airways and airspaces have been obtained using hyperpolarized ^{3}He, thus enabling identification of chronic pulmonary obstructive disease [9], emphysema [10], asthma [11], cystic fibrosis [12] and apnea [13].

Hyperpolarized ^{3}He gas was first used as a nuclear target in accelerator physics experiments measuring spin composition of neutrons [14, 15]. Soon afterwards the researchers realized the potential of ^{3}He and ^{129}Xe for MR imaging. The non-equilibrium polarization of hyperpolarized noble gases is up to five orders of magnitude larger than the thermal polarization of water [6]. After compensating for the smaller density of gas as compared to that of water one ends up with a tenfold increase in the MR signal. First MR images using polarized noble gas were published in a Nature article in 1994 [16].

The most common method for polarizing noble gases uses a transfer of polarization from an alkali metal (usually Rb) to the noble gas [6]. Rb electrons can be polarized to high values ($\approx 90\%$) using optical pumping of Rb vapor with circularly polarized laser light tuned to the D1 (795 nm) transition in Rb. Polarization of Rb electrons is transferred to the nucleus of the noble gas during collisions between Rb atoms and noble gas atoms [17, 18, 19].

We describe the production of cells containing noble gas and Rb and the optical pumping setup in Chapter 2. Since monitoring the magnetization levels of hyperpolarized gas is important for understanding the physics of hyperpolarized gases, we describe the implementation of NMR (nuclear magnetic resonance) and EPR (electron paramagnetic resonance) polarimetry at Caltech. We present NMR signals of ^{3}He, ^{129}Xe and water, EPR signals of

^{3}He, and preliminary EPR shifts of ^{129}Xe.

An important advantage of hyperpolarized gas MRI over the conventional proton MRI is that the hyperpolarized gas MR signal strength does not depend on the size of the magnetic field used during imaging [20, 21]. Furthermore, if imaging is performed at field strengths at which the sample (body) presents the dominant source of noise, the signal-to-noise ratio of the image is not affected by the field strength [22, 23]. Since low-field systems are easier and cheaper to build, and potentially accessible to a larger sample of population, it may be advantageous to perform hyperpolarized gas imaging at low magnetic field strengths.

Realizing the importance of low-field hyperpolarized gas imaging, we started a collaboration with the group of Dr. Steven Conolly at Stanford University Electrical Engineering Department. Dr. Conolly's group has developed a *pulsed* (or variable) resistive low-field MR scanner for prepolarized MR imaging of water (so-called PMRI). PMRI replaces the static superconductive main field magnet of a conventional MR scanner with two dynamic electromagnets: a polarizing magnet which creates the sample magnetization and thus has to produce a strong but not necessarily homogeneous field, and a readout magnet which needs to produce a homogeneous but not necessarily strong field and which determines the readout frequency [24, 25]. One of the main advantages of the pulsed resistive low-field system is reduction in capital cost. While the superconducting magnets can easily cost \$1 million and in addition have high maintenance costs, the two resistive magnets can be built for less than \$50,000. This cost reduction could significantly increase the access to MRI and thus enable early detection and regular monitoring of pulmonary disease.

The electronics of the pulsed resistive low-field MR scanner and the pulsed sequence used for PMRI of water are described in Chapter 3. In this chapter we also motivate the construction of a hybrid hyperpolarized gas/prepolarized water MR system by examining the SNR properties of conventional MRI, PMRI and hyperpolarized gas MRI.

While the SNR properties of hyperpolarized gas and prepolarized water are similar, there are also essential differences between the two imaging techniques. In particular, two properties of hyperpolarized gas distinguish hyperpolarized MRI sharply from proton MRI: the nonrenewable nature of the gas polarization and the substantially larger diffusion constant of gases as compared to water (^{3}He, for instance, has five orders of magnitude larger diffusion constant than water) [6]. The nonrenewable polarization, coupled with the long T_2 relaxation times of gases, motivate the use of single-shot sequences, such as

RARE [26] and trueFISP [27], which utilize all the available gas magnetization and can thus produce higher image SNR than small flip-angle sequences, such as FLASH [9, 28]. The large diffusion constant of gases causes rapid signal decay, which, however, can be minimized by proper sequence design.

In Chapter 4 we study, in detail, the T_2 relaxation and diffusion processes of hyperpolarized gases. We make a distinction between the reversible and nonreversible T_2 decay, and further divide the nonreversible decay into diffusion losses in the magnetic field gradients and the decay due to spin-spin interactions. The first half of the chapter gives the theoretical background for all these processes, while the second half presents our experimental results. We use Free-Induction-Decay (FID) signals of hyperpolarized ^{3}He, ^{129}Xe and water to compute the polarization of hyperpolarized gas. Furthermore, we collect spin echo trains using a CPMG sequence [29], which also serves as the basis for measurements of diffusion coefficients and the inherent T_2 relaxation times. In the Appendix A we estimate diffusion coefficients of binary gas mixtures using Lennard-Jones potentials [30].

In Chapter 5 we use the experimental values from Chapter 4 to develop a numerical model of signal decay during gradient echo sequence. We divide the effects which decrease the size of hyperpolarized gas signal into three groups: the effect of the excitation flip-angle; T_1 and T_2 relaxation losses; and diffusion losses. The simulation helps us to obtain a gradient echo image of a 1-inch spherical cell filled with hyperpolarized ^{3}He. In addition, we study, through modelling and experiments, the SNR gain in 1-D spin echo projection images when using centrally ordered phase-encode gradients. Our results show promise for 2-D RARE sequences with central ordering of encoding gradients.

Chapter 2

Hyperpolarized Gas Production and Polarimetry

2.1 Background

Optical pumping of alkali-metal atoms was introduced by Kastler [31] and Hawkins [32] at the beginning of the 1950s. Kastler received a Nobel Prize for the discovery and the development of optical methods for studying Hertzian resonances in atoms in 1966. Dehmelt [33] used optical pumping to study T_1 relaxation of polarized sodium atoms. The first published study of spin transfer (then called "dipolar-exchange") from the alkali-metal to ^{3}He was done by Bouchiat *et al.* [34] in 1960, and was extended to include all stable noble gas isotopes by Grover [35] in 1978. In the seventies and eighties, Happer *et al.* published several papers [1, 36, 17, 37] which laid out the theoretical foundations for hyperpolarized gas production using optical pumping and spin-exchange techniques. But it was not until the nineties, when researchers realized the potential of hyperpolarized gases for a wide range of applications, that the field really started to grow.

In the last ten years, hyperpolarized ^{3}He has been used as a target in nuclear physics experiments [14], and as an MR imaging agent for MR ventilation studies of animal and human lungs [38, 39]. Hyperpolarized ^{129}Xe has been used in MR imaging of materials [40] as well as in MR imaging of blood [41, 42] and animal brain [43]. In addition, the production [44, 45] and storage [46] of hyperpolarized gases have been optimized greatly and continue to improve.[1]

The polarization levels of noble gases have primarily been measured using the MR tech-

---

[1] In addition to polarization by spin-exchange with optically polarized alkali-metal, ^{3}He can also be polarized using direct optical pumping of its metastable 2 $^3S_1$ state [47].

nique of Adiabatic Fast Passage (AFP) [48]. However, the NMR-AFP polarimetry requires calibration against a source of known thermal polarization, usually water. In 1989, Schaefer *et al.* [5] introduced an absolute polarimetry technique based on the frequency shift of the electron paramagnetic resonance (EPR) of the alkali-metal. Since then, EPR polarimetry was implemented successfully for measuring polarization of ^{3}He during experiments at the Thomas Jefferson Laboratory in Virginia [49, 50, 51, 52], and at the Stanford Linear Accelerator Center [53].

The precision of the EPR polarimetry depends on the calibration of the EPR frequency shift as a function of the noble gas magnetization. The calibration constant $\kappa_\circ$ has been measured for Rb-^{3}He by Newbury *et al.* [4], and to a greater accuracy by Romalis *et al.* [3]. However, a comparable measurement of $\kappa_\circ$ for Rb-^{129}Xe interaction is still needed for ^{129}Xe EPR polarimetry to be used.

One of the disadvantages of the EPR technique is that it can only be used for measuring the noble gas polarization in the presence of an alkali-metal and a laser beam. As such, it is not suitable for *in vivo* polarimetry applications. Despite this limitation, the method is advantageous for a certain class of application, such as high-precision polarimetry required in hyperpolarized target experiments, or for applications requiring compact, cost-effective and reliable polarimetry setup.

2.2 Hyperpolarized Gas Production

Polarizing noble gases (either ^{129}Xe or ^{3}He) to achieve non-equilibrium polarization levels, which can be up to five orders of magnitude larger than the thermal polarization, is a two step process. First, the outer electron of an alkali-metal (usually, rubidium) is polarized using the technique of optical pumping with circularly polarized laser light tuned to the D1 spectral transition (7850 $\mathring{A}$) in rubidium. Second, the rubidium electron polarization is transferred to the nuclei of the noble gas during spin-exchange collisions via a Fermi contact interaction. We describe optical pumping and spin-exchange processes in the following two sections.

2.2.1 Optical Pumping

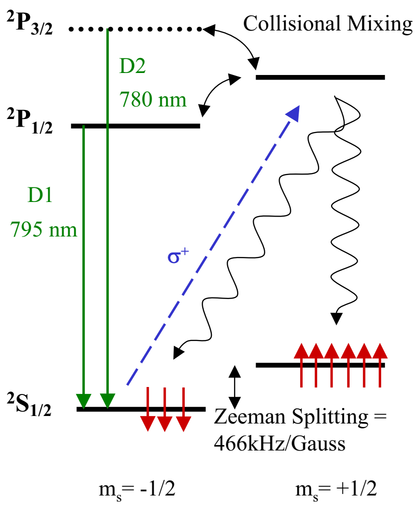

Figure 2.1: Electron levels in ^{85}Rb atom, assuming $I_{Rb} = 0$. The vertical axis is not drawn to scale.

A pictorial view of optical pumping is presented in Figure 2.1. For simplicity, the diagram ignores the rubidium nuclear spin. A more detailed view of the ^{85}Rb magnetic sublevels which takes into account the rubidium nuclear spin ($I = 5/2$ for ^{85}Rb, $I = 3/2$ for ^{87}Rb) is given in Figure 2.2.

When rubidium is placed in a magnetic field, the Zeeman sublevels ($m_S = \pm 1/2$) split. At low fields (20 G) the splitting is proportional to the magnetic field B, so that $\nu = \gamma_{Rb}\, B$, where $\gamma_{Rb} = 466$ kHz/G. Figure 2.1 shows the splitting of the $^2S_{1/2}$ ground level and the

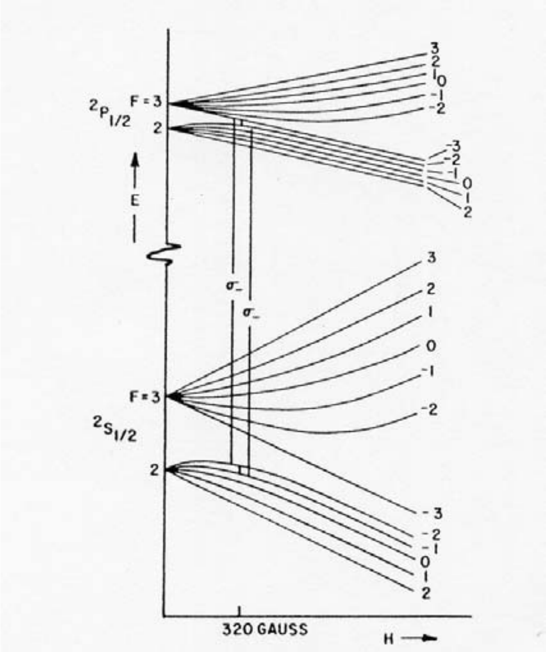

Figure 2.2: ^{85}Rb magnetic sublevels. Taken from a paper by W. Happer [1].

$^2P_{1/2}$ excited level. Initially, the difference in the electron populations between the two m_S sublevels is thermal in nature and thus small. However, a non-equilibrium polarization can be achieved by using circularly polarized light (with either positive or negative angular momentum) tuned to 7950 $\mathring{A}$ to excite selectively transitions from either ($^2S_{1/2}$, $m_S = -1/2$) to ($^2P_{1/2}$, $m_S = +1/2$) or from ($^2S_{1/2}$, $m_S = +1/2$) to ($^2P_{1/2}$, $m_S = -1/2$), but not both. Collisions with the noble gas atoms then rapidly equalize the populations of the excited state sublevels [19]. Normally, the electrons decay back to the ground level by emitting radiation at the D1 and D2 wavelengths.[2] Since this radiation is unpolarized, it would destroy the electron polarization by non-selectively exciting electron transitions from both Zeeman $^2S_{1/2}$ sublevels. To minimize the radiative decay back to the ground level, a buffer gas, such as nitrogen, is used. Electrons then transfer their energy to the rotational and vibrational modes of the nitrogen molecule [53] and decay to both ground-state sublevels with equal probability. Nitrogen densities of 0.1 amagats (approx. 0.1 atm) suffice to eliminate radiation trapping as a source of relaxation [1]. Continuous selective excitation of the electrons will depopulate one of the Zeeman sublevels and leave approximately 80% of electrons in the non-excitable Zeeman sublevel.

---

[2] The transition from $^2P_{1/2}$ level is called D1 transition, while the transition from $^2P_{3/2}$ level is called D2 transition. These transition will be mentioned again in the section on EPR polarimetry.

The Hamiltonian of the rubidium atom in a holding magnetic field $\mathbf{B} = B_\circ \hat{\mathbf{z}}$ is [19]

$$H = A_e \, \mathbf{I} \cdot \mathbf{S} + g_e \, \mu_B \, S_z \, B_z - \frac{\mu_I}{I} \, I_z \, B_z. \tag{2.1}$$

The first term in Eq. 2.1 represents the hyperfine interaction between the alkali-metal nuclear spin I ($I = 5/2$ for ^{85}Rb), and the electron spin S. The strength of this interaction is characterized by the isotropic magnetic-dipole coupling coefficient A_e. The second and third terms describe the coupling of the electron and nuclear spins with the magnetic field $\mathbf{B}$. The constant $g_e = 2.00232$ for the electron, μ_B is the Bohr magneton ($\mu_B = 9.2741 \times 10^{-21}\,\mathrm{erg\,G^{-1}}$), μ_I is the nuclear magnetic moment of the alkali-metal and I is the nuclear-spin quantum number. Since $\mu_B \gg \mu_I$, the Zeeman splitting is dominated by the electron spin. Furthermore, at low fields most commonly used for optical pumping applications (magnetic fields in the range of 1-30 G), the hyperfine interaction dominates over the Zeeman interactions, so the computations can be done in the eigenstates of the total angular momentum $\mathbf{F} = \mathbf{I} + \mathbf{S}$.

The local rubidium polarization P_{Rb} approaches a steady state. It is expressed in terms of the local mean optical pumping rate per unpolarized alkali-metal atom $\gamma_{opt}(\mathbf{r})$, and the electron spin destruction rate Γ_{SD} [18, 6]:

$$P_{Rb} = \frac{\gamma_{opt}(\mathbf{r})}{\gamma_{opt}(\mathbf{r}) + \Gamma_{SD}}. \tag{2.2}$$

The local mean optical pumping rate is

$$\gamma_{opt}(\mathrm{r}) = \int_0^\infty \Phi(\mathrm{r}, \nu) \, \sigma_{op}(\nu - \nu_\circ) \, d\nu, \tag{2.3}$$

where $\Phi(\mathrm{r}, \nu)$ is the laser intensity per unit frequency, while $\sigma_{op}(\nu - \nu_\circ)$ is the cross section for absorption of unpolarized light. The electron spin destruction rate is dominated by collisions of rubidium with other gas particles, rather than by the collisions with the glass walls of the cell. It can be expressed as [54]

$$\Gamma_{SD} = k_{Rb-NG} \, n_{NG} + k_{Rb-Rb} \, n_{Rb} + k_{Rb-N_2} \, n_{N_2}, \tag{2.4}$$

where the spin destruction rates $k_{Rb-x}[\mathrm{cm^3/s}]$ have been measured by Wagshul *et al.* [55], while the gas number densities n_x are a function of the cell composition. Rubidium number density n_{Rb} can be estimated from the Killian formula [4], $\log_{10} n_{Rb} = 26.41 - 4132/T - \log_{10} T$, where the Rb number density is in units of $1/\text{cm}^3$ and temperature is in units of K. In ^{129}Xe experiments, $T \approx 90^\circ$ C, so $n_{Rb} \approx 3 \times 10^{12}$ cm^{-3}, while during ^{3}He experiments, $T \approx 140^\circ$ C, so $n_{Rb} \approx 6 \times 10^{13}$ cm^{-3}.

2.2.2 Spin Exchange

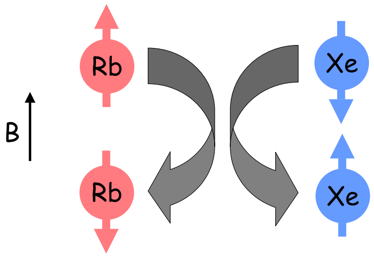

Figure 2.3: Spin transfer between the rubidium electron and the noble gas nucleus.

Spin exchange is the process by which the alkali-metal electrons transfer their polarization to the spin-1/2 nuclei of the noble gas (see Figure 2.3). The interaction Hamiltonian between ^{85}Rb and ^{129}Xe is [17]

$$H = \gamma\,\mathbf{N}\cdot\mathbf{S} + \alpha\,\mathbf{K}\cdot\mathbf{S}. \tag{2.5}$$

The first term in Eq. 2.5 is the spin-rotation interaction between the alkali-metal electron spin **S** and the rotational angular momentum **N** of the alkali-metal–noble-gas molecule. This term represents the loss of the alkali-metal electron polarization to the orbital angular momentum of the alkali-metal–noble-gas pair. The second term describes the isotropic hyperfine interaction (or so-called Fermi-contact interaction) responsible for the spin exchange between the alkali-metal electron spin **S** and the noble gas nuclear spin **K**. γ and α are coupling coefficients which depend on the intermolecular separation and velocity of the unbound colliding pair [17].

The time evolution of the noble gas polarization can be approximated by an exponential equation, given as

$$P_{NG}(t) = \langle P_{Rb}\rangle \frac{\gamma_{SE}}{\gamma_{SE} + \Gamma} \left\{1 - e^{-(\gamma_{SE}+\Gamma)t}\right\}, \tag{2.6}$$

where $\langle P_{Rb} \rangle$ is the average rubidium polarization in the cell and can be determined from Eq. 2.2; Γ is the noble gas nuclear spin relaxation rate in the absence of Rb vapor; and $\gamma_{SE} = k_{SE}\, n_{Rb} = \langle v\sigma_{SE} \rangle\, n_{Rb}$ is the spin-exchange rate. The most recent measurement of the velocity averaged He-Rb spin-exchange cross section was done by Baranga *et al.* [56]: $k_{SE} = (6.7 \pm 0.6) \times 10^{-20}$ cm^3/s. Xe-Rb spin-exchange cross section is still being investigated as a result of two contradictory measurements: Cates *et al.* [57] measured $k_{SE} = (3.70 \pm 0.70) \times 10^{-16}$ cm^3/s, while Jau *et al.* [58] measured $k_{SE} = (1.72 \pm 0.08) \times 10^{-16}$ cm^3/s.

The noble gas nuclear spin relaxation rate in Eq. 2.6 is a function of the spin-relaxation resulting from the dipole interaction between the noble gas atoms, Γ_D; the spin-relaxation resulting from the collisions with the paramagnetic impurities in the walls of the cell, Γ_{Wall}; and the spin loss due to the magnetic field gradients, $\Gamma_{\triangle B}$ [53]:

$$\Gamma = \Gamma_D + \Gamma_{Wall} + \Gamma_{\triangle B}. \tag{2.7}$$

2.2.3 Experimental Setup

The experimental procedure consists of two main steps. After the cells are made at a glassblower shop, they are filled with a noble gas, nitrogen and an alkali-metal on our vacuum-gas system. The noble gas in the cells is then polarized using the optical pumping system.

2.2.3.1 Vacuum System and Cell Production

The noble gas used in our experiments is contained in sealed glass cells. In addition to ^{3}He (or ^{129}Xe), a few milligrams of Rb metal and a small amount of nitrogen gas were also introduced into the cells. Two cells were used in our experiments: a ^{3}He cell and a ^{129}Xe cell. The gas composition of these cells is given in Table 2.1. The cells had two cylindrical chambers and a tubing connecting the two chambers (see Figure 2.4). The top chamber was used for optical pumping and EPR polarimetry, while the bottom chamber was used for NMR polarimetry.[3] The dimensions and the shape of the cells are based on several requirements. First, the surface-to-volume ratio of the pumping chamber has to be minimized in order to decrease the surface relaxation rate of polarized gas nuclei per

---

[3] The two-chamber cell geometry was inherited from SLAC experiments, in which a laser beam was directed onto the top chamber to optically pump the gas, while an electron beam was directed onto the bottom chamber to study the spin structure of the neutron.

unit volume. This means that ideally, the pumping chamber would have to be spherical. However, laser beam reflects and refracts on a curved glass surface, potentially minimizing the efficiency of optical pumping. A cylindrically shaped cell, with nearly flat front and back optical windows is preferable.

	Hyp Gas Pressure (atm)	Nitrogen Pressure (atm)
^{129}Xe Cell	0.10	0.06
^{3}He Cell	8.36	0.08

Table 2.1: The gas content of ^{129}Xe and ^{3}He cells used at Caltech. All pressures measured at room temperature. ^{3}He cell parameters taken from [2].

The ^{3}He cell was filled by Hunter Middleton during his PhD research and was used in the E-142 experiment at SLAC which measured the spin structure of the neutron. A detailed description of cell production technique, including cell parameters, is given in his thesis [2]. In Table 2.2 we summarize the parameter values relevant to our experiments. The ^{129}Xe cell (see Figure 2.4), on the other hand, was filled by Ray Fuzesy who was in charge of cell production for our experiments from 2000-2001. The cell was made from quartz glass tubing in a glass shop in Berkeley, California.[4] Table 2.2 gives the cell dimensions.

Cell		Rb-He	Rb-Xe
Top Cylinder	Diameter [cm]	3.66	3.8
	Length [cm]	8.0	8.2
	Wall thickness [cm]	0.095	0.1
	Volume [cm^3]	70.4	81.4
Bottom Cylinder	Diameter [cm]	2.14	2.2
	Length [cm]	29.5	11.6
	Wall thickness [cm]	0.075	0.1
	Volume [cm^3]	89.2	35.8
Transfer Tube	Diameter [cm]	1.24	1.1
	Length [cm]	5.8	6.3
	Wall thickness [cm]	0.14	0.1
	Volume [cm^3]	4.2	3.9

Table 2.2: Dimensions of ^{3}He cell (taken from [2]) and ^{129}Xe cell.

---

[4] Unlike ^{3}He cells, ^{129}Xe cells do not require specialized glass, because of lower ^{129}Xe permeability of

Figure 2.4: ^{129}Xe cell used for NMR and EPR polarimetry studies.

The Caltech vacuum system was capable of handling low pressures (down to 10^{-8} atm) as well as high pressures (up to 6 atm). This wide range in pressure was achieved with two pumps, a turbo-molecular pump and an ion-pump, as well as valves which were able to withstand high pressures. In addition, a residual gas analyzer enabled the monitoring of the impurities in the gas system. Finally, the vacuum system had two delivery lines, one for the noble gas and one for nitrogen gas.

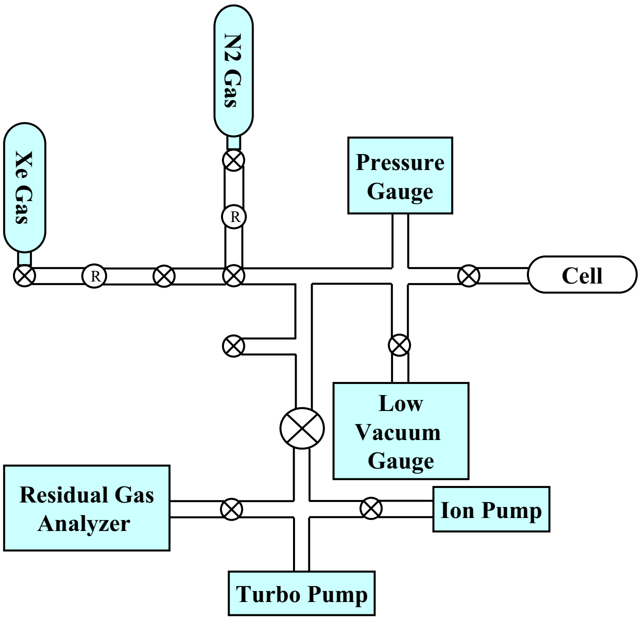

Figure 2.5: A schematics of the vacuum system used for Xe-cell production.

---

^{129}Xe through the glass.

2.2.3.2 Optical Pumping Setup

Optical pumping of ^{3}He and ^{129}Xe was performed with four Titanium-Sapphire (Ti-Sapph) lasers (*Spectra Physics*, model 3900S). Each Ti-Sapph laser was pumped by an Argon laser (*Spectra Physics*, model 2040E) and produced up to 5 W of tunable-wavelength laser light. The Ti-Sapph lasers have on the order of 100 times narrower bandwidth than the most commonly used diode laser, which is advantageous when pumping gas at low pressures with narrow-bandwidth absorption profiles. Figure 2.6 shows the Ti-Sapph lasers (front) and Argon lasers (back).

Figure 2.6: A photograph of the Ti-Sapphire lasers which were used for optical pumping at Caltech.

The Ti-Sapph laser beam was directed through a set of diverging lenses which expanded the beam to the size of the cell's cross section (see Figure 2.7) and then to a set of mirrors which directed the beam onto the cell. Since the laser light produced by the Ti-Sapph lasers was linearly polarized (in the horizontal direction) while optical pumping of Rb requires circularly polarized light, a quarter waveplate was placed between each laser and the cell. After passing through the quarter waveplate, the laser light was $\approx 90\%$ circularly polarized.

The cell containing the hyperpolarized gas was placed in the middle of a constant magnetic field. The field was produced by a set of Helmholtz coils which were controlled by a bipolar operational power supply (*Kepco*, model BOP 36-12M). The pumping chamber of the cell was enclosed in a homemade high-temperature resistant oven. The oven had optical windows on the front and the back for the passage of laser light and on the sides for the monitoring of the laser light absorption/fluorescence with a CCD camera.

A constant flow of hot air through the oven enabled us to heat the cells to the desired

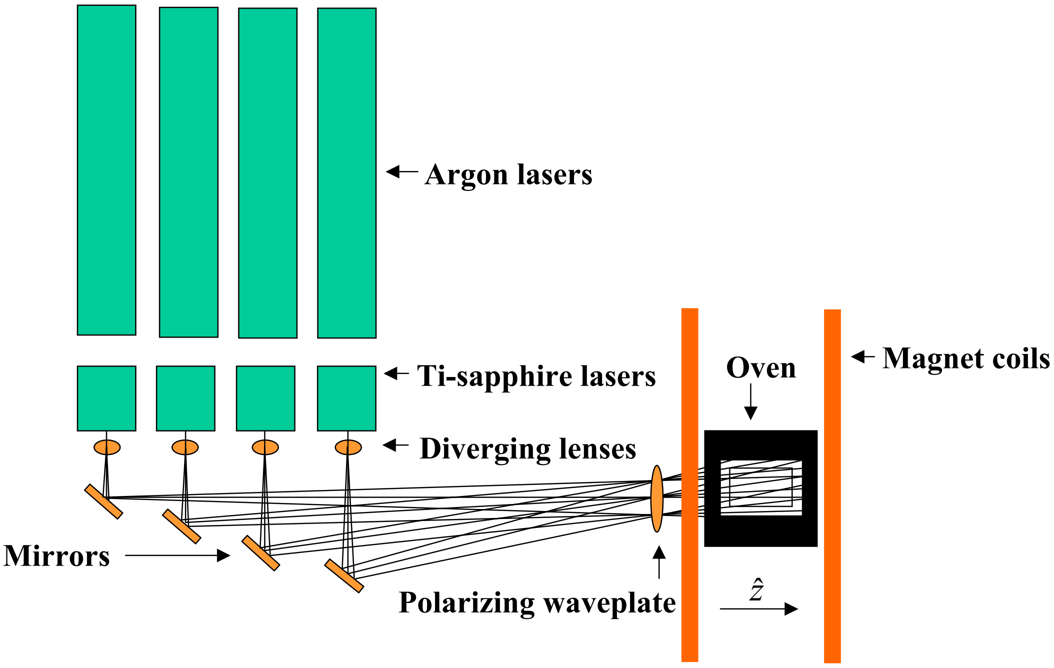

Figure 2.7: A schematics of the optical pumping setup.

temperature, which for ^{129}Xe cells was 80°-100°C, while for ^{3}He cells was 120°-150°C. The temperature was detected with a non-magnetic RTD (resistive temperature device) and monitored with a standard multimeter.

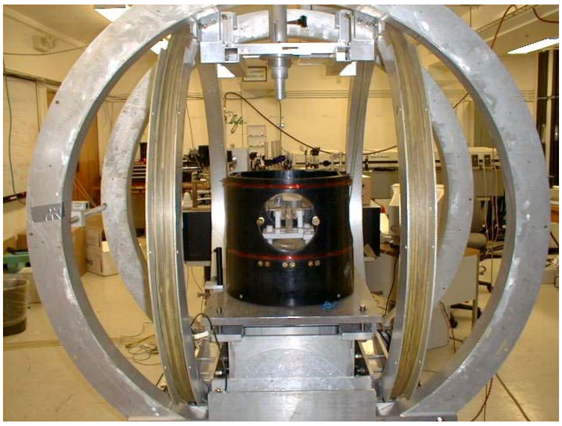

Figure 2.8: A photograph of the Helmholtz electromagnet at Caltech.

2.3 Hyperpolarized Gas NMR Polarimetry

2.3.1 NMR Polarimetry Principles

Nuclear magnetic resonance (NMR) is observed in systems that possess magnetic moment $\boldsymbol{\mu}$and spin angular momentum $\mathbf{I}$ which are related by

$$\boldsymbol{\mu} = \gamma \hbar \mathbf{I}, \tag{2.8}$$

where the constant of proportionality between the two is the gyromagnetic ratio γ. When the magnetic moments are placed in a static magnetic field, they align parallel or anti-parallel to the field to occupy the lowest energy state. The energy of a 1/2 spin particle in a field $\mathbf{B} = B_z \hat{\mathbf{z}}$ is equal to

$$E = -\gamma \hbar B_z m_z, \tag{2.9}$$

where $m_z = \pm 1/2$.

The tendency of the magnetic moments to align with the field is counter-balanced by the thermal motion which randomizes the alignment of the spins. The extent of thermal motion depends on the temperature of the sample and follows the laws of statistical mechanics. The ratio of the magnetic moments in the high energy state, $N_\downarrow$, and the magnetic moments in the low energy state, $N_\uparrow$, is proportional to the Boltzmann factor

$$\frac{N_\downarrow}{N_\uparrow} = \exp\left(-\frac{\Delta E}{kT}\right). \tag{2.10}$$

The population difference between two energy states produces a polarization of the sample. For a proton spin in a 1.5 T magnetic field and at room temperature (300 K) this thermal polarization is very small, on the order of 10^{-6}. The net macroscopic magnetization of the sample $\mathbf{M}$ is then proportional to the polarization P, the number density of the sample n, and the nuclear magnetic moment $\boldsymbol{\mu}$:

$$\mathbf{M} = \langle \boldsymbol{\mu} \rangle = \boldsymbol{\mu}\, n\, P. \tag{2.11}$$

The principle behind NMR lies in perturbing the macroscopic magnetization from its equilibrium along the z-axis by adding energy to the system in the form of radio frequency

(RF) electro-magnetic radiation, and observing the subsequent relaxation of magnetization towards its equilibrium. The RF field oscillates with rotational frequency ω and can be expressed as

$$\begin{aligned}
\mathbf{B}_1 &= 2\,B_1\,\cos(\omega t)\,\hat{\mathbf{x}} \\
&= B_1\left[\cos(\omega t)\,\hat{\mathbf{x}} + \sin(\omega t)\,\hat{\mathbf{y}}\right] + B_1\left[\cos(\omega t)\,\hat{\mathbf{x}} - \sin(\omega t)\,\hat{\mathbf{y}}\right] \\
&= B_1\,\hat{\mathbf{x}}_{rot} + B_1\,\hat{\mathbf{y}}_{rot}, \\
\hat{\mathbf{x}}_{rot} &= \left[\cos(\omega t)\,\hat{\mathbf{x}} + \sin(\omega t)\,\hat{\mathbf{y}}\right] \\
\hat{\mathbf{y}}_{rot} &= \left[\cos(\omega t)\,\hat{\mathbf{x}} - \sin(\omega t)\,\hat{\mathbf{y}}\right]. \qquad (2.12)
\end{aligned}$$

The second and third line of the above equation show that the RF field can be decomposed into two counter rotating components, each of magnitude B_1.

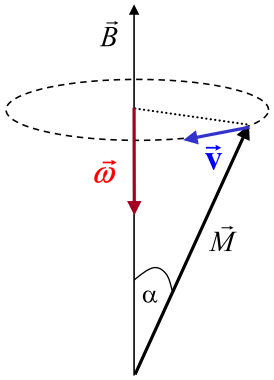

Figure 2.9: Magnetization precessing like a spinning top around the effective magnetic field **B** with a characteristic frequency ω.

The RF field flips (or tips) the magnetization away from the static field axis. When the magnetization is not parallel to the static magnetic field, it experiences a torque which causes it to precess around the net (total) field like a spinning top, with a characteristic Larmor frequency $\boldsymbol{\omega} = \gamma\mathbf{B}$ (see Figure 2.9). The equation of motion of the precessing magnetization (ignoring the relaxation processes) is equivalent to that of a spinning top:

$$\frac{d\mathbf{M}}{dt} = \mathbf{M} \times \gamma\mathbf{B}_{eff}. \qquad (2.13)$$

$\mathbf{B}_{eff}$ is the effective magnetic field, commonly expressed in a frame of reference which is rotating with angular frequency ω around the static field and is defined by rotating coordinates $\hat{\mathbf{x}}_{rot}$ and $\hat{\mathbf{y}}_{rot}$. In this frame, only the component of B_1 field which is co-rotating with the reference frame can affect the magnetization. If the holding field along the z-axis is $B_z\hat{\mathbf{z}}$, then the effective field is

$$\mathbf{B}_{eff} = \left(B_z - \frac{\omega}{\gamma}\right)\hat{\mathbf{z}} + B_1\hat{\mathbf{x}}_{rot}. \tag{2.14}$$

If $B_z = \omega/\gamma$, the effective field has no $\hat{\mathbf{z}}$ component in the rotating frame and the magnetization aligns entirely with the $\mathbf{B_1}$ field. This is the resonance condition. In the laboratory frame, $\mathbf{B_1}$ and $\mathbf{M}$ rotate around the static magnetic field in the xy plane. The magnetic flux created by the precessing magnetization can be detected by a set of NMR receiver coils whose axes are perpendicular to $\hat{\mathbf{z}}$.

In addition to the precession around the effective magnetic field, the magnetization is subjected to the relaxation processes. There are two main types of relaxation: the T_1 relaxation is the relaxation of the longitudinal magnetization component back to thermal equilibrium levels, $M_\circ$, along the z-axis; the T_2 relaxation describes the decay of the transverse magnetization component to zero (Chapter 4 gives a detailed description of T_2 relaxation). When the relaxation processes are included into Eq. 2.13, one obtains the Bloch equations [59]:

$$\frac{d\mathbf{M}}{dt} = \mathbf{M} \times \gamma\mathbf{B}_{eff} - \frac{M_x\hat{\mathbf{i}} + M_y\hat{\mathbf{j}}}{T_2} - \frac{(M_z + M_\circ)\hat{\mathbf{k}}}{T_1}. \tag{2.15}$$

2.3.1.1 Adiabatic Fast Passage

One way to measure the polarization of hyperpolarized gas is to use the NMR technique of Adiabatic Fast Passage (AFP) [48]. In AFP, the magnetization is flipped adiabatically by 180° around x (or y) axis. The magnetization flip is achieved by either sweeping the static magnetic field B_z or the frequency ω through resonance, so that $B_z = \omega/\gamma$.

If the static magnetic field is varied in time, then B_z in Eq. 2.14 is a time-varying field $B_z(t)$. Initially, the static magnetic field is much bigger than ω/γ so that the effective field is essentially aligned with the z-axis. The static field is then varied linearly (and adiabatically) through resonance until $|B_z(t)| \gg \omega/\gamma$. Figure 2.10 schematically shows the magnetization flip.

For minimal losses of polarization to occur during the AFP sweep, two conditions must

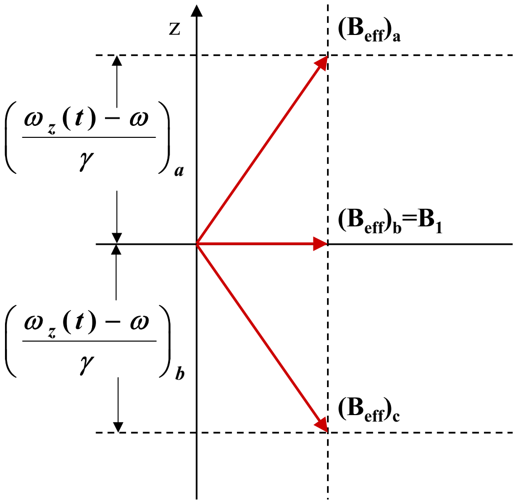

Figure 2.10: Schematics of spin-flip using the technique of the adiabatic fast passage.

be satisfied. First, the sweep must be slow enough for the magnetization to follow the effective magnetic field adiabatically. This is possible only if the rotation of magnetization around the static magnetic field in the laboratory frame (which is characterized by frequency ω) is much faster than the rotation of the effective field B_{eff}. This condition ensures that the initial relationship of magnetization with respect to the effective field remains valid throughout the sweep. Since the maximum field variation occurs on resonance, when $B_z(t) = \omega/\gamma$,

$$\left(\frac{dB_{eff}/dt}{B_{eff}}\right)_{B_z(t)=\omega/\gamma} = \frac{dB_z/dt}{B_{eff}} = \frac{dB_z/dt}{B_1}.$$

The *adiabatic* condition can then be written as

$$\frac{dB_z/dt}{B_1} \ll \omega. \tag{2.16}$$

In our NMR-AFP experiments, $dB_z/dt = 2.3$ G/s (see also Table 2.3), $B_1 \approx 0.1$ G [53], and the resonant frequency is $\omega_{He} = 2\pi f_{He} = 5.78 \times 10^5$ Hz for ^{3}He and $\omega_{Xe} = 2\pi f_{Xe} = 2.07 \times 10^5$ Hz for ^{129}Xe. Therefore, $\frac{dB_z/dt}{B_1} = 23\ \mathrm{s}^{-1} \ll \omega$.

Second, the sweep must be fast enough so that minimal transverse relaxation occurs during the sweep. This condition ensures that the magnetization vector remains constant in length during the sweep. The *fast* condition can be written as [53]

$$\frac{D\,|\nabla B_z|^2}{B_1^2} \ll \frac{dB_\circ/dt}{B_1}, \tag{2.17}$$

where D is the gas diffusion coefficient and $|\nabla B_z|$ is the gradient of the z-component of the magnetic field.[5] Since ^{129}Xe diffusion coefficient is smaller than ^{3}He diffusion coefficient (Appendix A) due to smaller ^{129}Xe mass, it suffices to prove the fast condition for ^{3}He. The field gradients have not been measured in our experiments. However, the data presented in [53] which used our experimental setup, indicates that $|\nabla B_z|$ should at or below G/m levels. If $|\nabla B_z| \approx 1$ G/m, $B_1 \approx 0.1$ G, $D \approx 1.7 \cdot 10^{-4}$ m^2/s, then $\frac{D|\nabla B_z|^2}{B_1^2} \approx 0.017\,\mathrm{s}^{-1} \ll \frac{dB_z/dt}{B_1} = 23\,\mathrm{s}^{-1}$. Consequently, both the *adiabatic* and *fast* conditions are satisfied, so the AFP losses should be minimal (below 0.1% per sweep [53]).

It remains to determine the size of the AFP signal. The AFP signal detected in the NMR receiver coils will be proportional to the transverse magnetization component

$$M_T = M\sin\alpha = M\,\frac{(B_{eff})_T}{B_{eff}} = M\,\frac{B_1}{\sqrt{\left[B_z(t)-\frac{\omega}{\gamma}\right]^2 + B_1^2}}. \tag{2.18}$$

Equation 2.18 tells us that the AFP signal will have a Lorentzian-like shape.[6]

In addition to being proportional to the transverse magnetization, the signal size also depends on the amount of magnetic flux Φ passing through the receiver coils, the gain G^{amp} of the pre-amplifier (see section 2.3.2), and the gain G^Q associated with the Q-curve of the NMR receiver coils. All other system-dependent factors are calibrated from a source of known thermal polarization (e.g., water) and included in the factor β. The hyperpolarized noble gas and water AFP signals are, respectively,

$$\begin{aligned}
S_{NG} &= \beta\, M_T^{NG}\, G_{NG}^{amp}\, \Phi_{NG}\, G_{NG}^{Q} \\
&= \beta \left\{ \mu_{NG}\, n_{NG}\, P_{NG}\, \frac{B_1}{\sqrt{\left[B_z(t)-\frac{\omega}{\gamma}\right]^2 + B_1^2}} \right\} G_{NG}^{amp}\, \Phi_{NG}\, G_{NG}^{Q} \\
&= \alpha\, \mu_{NG}\, n_{NG}\, P_{NG}\, G_{NG}^{amp}\, \Phi_{NG}\, G_{NG}^{Q} \qquad (2.19)
\end{aligned}$$

---

[5] The z-component of the total field includes the static field along $\hat{\mathbf{z}}$, as well as any gradients applied in the $\hat{\mathbf{z}}$ direction.

[6] Unlike the Lorentzian, the signal in Eq. 2.18 has a square root in the denominator.

$$S_{H_2O} \;=\; \alpha\, \mu_p\, n_{H_2O}\, P_{H_2O}\, G^{amp}_{H_2O}\, \Phi_{H_2O}\, G^{Q}_{H_2O}, \tag{2.20}$$

where $\alpha = \beta\, B_1/\sqrt{\left[B_z(t) - \frac{\omega}{\gamma}\right]^2 + B_1^2}$. The thermal polarization of water (see Chapter 4.5.1 for a more detailed derivation) is

$$P \sim \frac{\hbar\gamma B_z}{2kT} = \frac{\mu_p B_z}{kT}. \tag{2.21}$$

If Eq. 2.21 is inserted into Eq. 2.20 and the constant α from Eq. 2.20 into Eq. 2.19, the hyperpolarized gas polarization is

$$P_{NG} = \frac{\mu_p \frac{\omega}{\gamma}}{kT}\, \frac{S_{NG}}{S_{H_2O}}\, \frac{\mu_p}{\mu_{NG}}\, \frac{n_{H_2O}}{n_{NG}}\, \frac{G^{amp}_{H_2O}}{G^{amp}_{NG}}\, \frac{\Phi_{H_2O}}{\Phi_{NG}}\, \frac{G^{Q}_{H_2O}}{G^{Q}_{NG}}. \tag{2.22}$$

2.3.2 NMR Electronics

NMR Parameters	Water	He	Xe
Field Sweep (Gauss)	18.0-28.3	18.9-29.2	21.3-31.6
Sweep Rate (G/s)	2.34	2.34	2.34
Pre-Amp Gain	100	10	100
RF Amp Gain (Volts)	50	50	50
Q-Curve Gain (relative)	1	1	0.09
f_{RF} (kHz)	92	92	33
B_{res} (Gauss)	21.6	28.4	27.8

Table 2.3: Parameter values during the NMR-AFP experiment.

Figure 2.11 shows the schematics of the NMR electronics. A static magnetic field which is produced by a set of Helmholtz coils defines the z-axis. The other two sets of axes are defined by the RF coils and the NMR receiver coils.

The AFP signal from both receiver coils was added up and amplified in a pre-amplifier (*Stanford Research Systems*, model SR560). Because the receiver coils were not perfectly perpendicular to the RF coils, they picked up not only the AFP signal, but also some residual driving RF field, which was produced by amplifying the output of a function generator (amplifier: *EIN*, model 2100L). However, unlike the AFP signal, the RF pick-up signal was nearly 180° phase-shifted in the two NMR coils. By adding the signals from the two coils, the RF pick-up should have cancelled completely. In reality, the cancellation was not

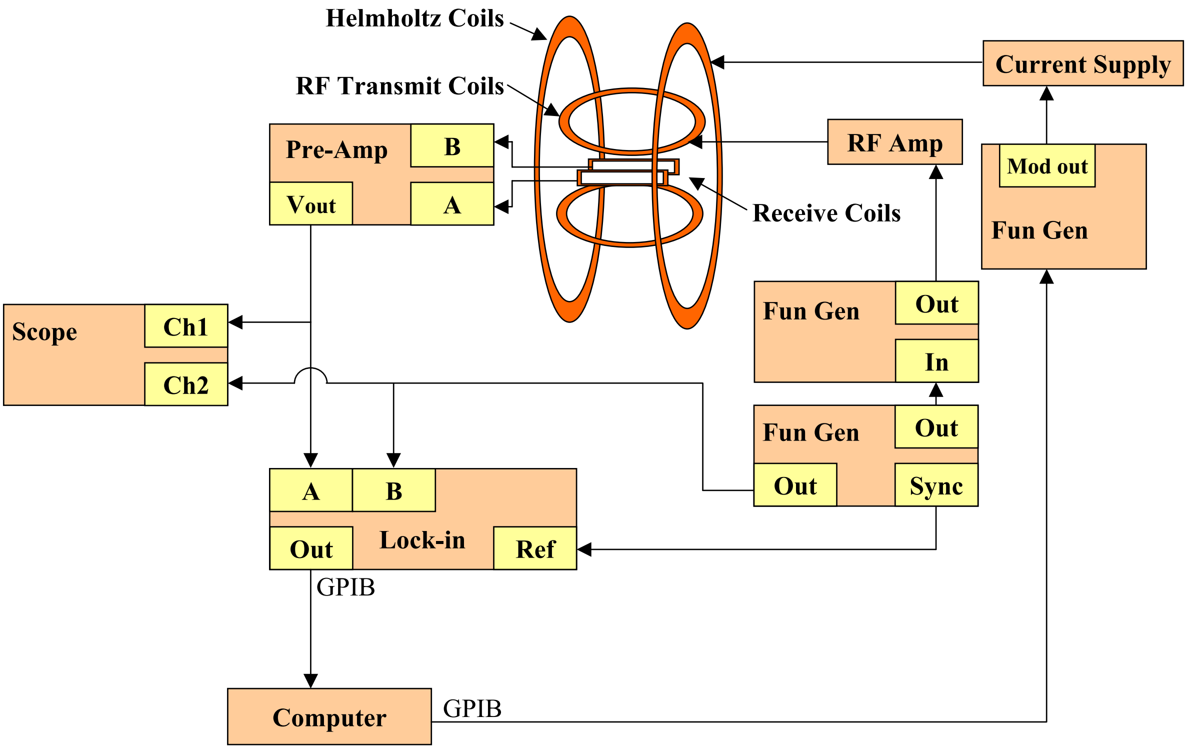

Figure 2.11: Electronic circuitry for NMR detection.

perfect, and there was still a small residual RF signal in the output of the pre-amplifier. A lock-in amplifier (*Stanford Research Systems*, model SR830 DSP), an oscilloscope and a function generator (*Hewlett Packard*, model 33120A) with an adjustable amplitude and phase and with frequency locked to the radio-frequency, were used to cancel the residual RF pick-up field. Values of the main NMR parameters are listed in Table 2.3.

A LabView program and a function generator (*Hewlett Packard*, model 3325B) controlled the field sweep.[7] The holding field was swept ±10.3 G (usually starting at around 18 G) in 8.8 s (at a rate of 2.34 G/s), which resulted in two spin flips and, therefore, two AFP signals (see Figure 2.12). The resulting signal was recorded by the computer and displayed in *LabView*.

---

[7] Note that in the NMR experiment, the AFP sweep can only be performed by sweeping the B_z field through resonance. Sweeping the frequency through resonance is not feasible because the cancellation of the residual RF pick-up can only be performed at a single (constant) frequency.

2.3.3 Water NMR Signals and Water Thermal Polarization

From Eq. 2.20, the water signal is

$$\begin{aligned} S_{H_2O} &= \beta \, \frac{B_1}{\sqrt{\left[B_z(t) - \frac{\omega}{\gamma}\right]^2 + B_1^2}} \, \mu_p \, n_{H_2O} \, P_{H_2O} \, G^{amp}_{H_2O} \, \Phi_{H_2O} \, G^{Q}_{H_2O} \\ &= \beta \, \frac{M \, G^{amp}_{H_2O} \, \Phi_{H_2O} \, G^{Q}_{H_2O}}{\sqrt{\left[\frac{B_z(t) - \frac{\omega}{\gamma}}{B_1}\right]^2 + 1}} . \end{aligned} \tag{2.23}$$

Therefore, if we fit the AFP signals with a function of the form

$$\frac{A}{\sqrt{\left[\frac{x - x_\circ}{\Delta x}\right]^2 + 1}} + a\,x^2 + b\,x + c,$$

then $A = \beta \; M_{H_2O} \; G^{amp}_{H_2O} \; \Phi_{H_2O} \; G^{Q}_{H_2O}$, $x = B_z(t)$, $x_\circ = B_{res} = \omega/\gamma$, $\Delta x = B_1$. The quadratic function in x was added to account for the changing background during the AFP flip. Computing water thermal polarization using Eq. 2.21 at the resonant field values we can then find the calibration constant β. In addition, the width of the resonance gives a measure of the B_1 strength. Table 2.4 gives values of the parameters used in the calibration of β for ^{3}He and ^{129}Xe and the corresponding uncertainties.

Water Parameter	^{3}He NMR-AFP calibration		^{129}Xe NMR-AFP calibration	
	Value	Uncertainty	Value	Uncertainty
μ_p (eV/G)	$8.803\times10^{-12} = 2.7928\mu_N$	-	$8.803\times10^{-12} = 2.7928\mu_N$	-
γ (Hz/G)	4258	-	4258	-
kT@25°C (eV)	0.0257	2%	0.0257	2%
f_{RF} (kHz)	92	0.5%	92	0.5%
n_{H2O} @25°C (amg)	2489.4	0.5%	2489.4	0.5%
A_{H2O} (from fit)	3.85×10^{-5}	2.5%	4.8×10^{-5}	2.5%
G^{amp}_{H2O}	100	0.5%	100	0.5%
G^{Q}_{H2O} (r.u)	1	-	1	-
$\Phi_{H2O} \propto r^2_{H2O}$ (cm)	$(0.9)^2$	2.5%	1	2.5%

Table 2.4: Parameters related to water AFP signal.

Note that the above analysis ignores T_1 and T_2 water relaxation during the AFP flip. To account for the relaxation processes the AFP resonances should be modelled using the Bloch equation (Eq. 2.15), as was done in [53, 54]. The results in these works show that the two APF resonances (the resonance during the up-ramp and the resonance during the down-ramp of the magnetic field) have slightly different amplitudes. However, to first order, it suffices to approximate the amplitude of the water thermal signal with the average amplitude of the two AFP resonances and the thermal water polarization with the average thermal polarization at the two resonant field values [2].

Figure 2.12 shows water AFP signals and the corresponding fits that were used in the calibration of ^{3}He and ^{129}Xe polarization.

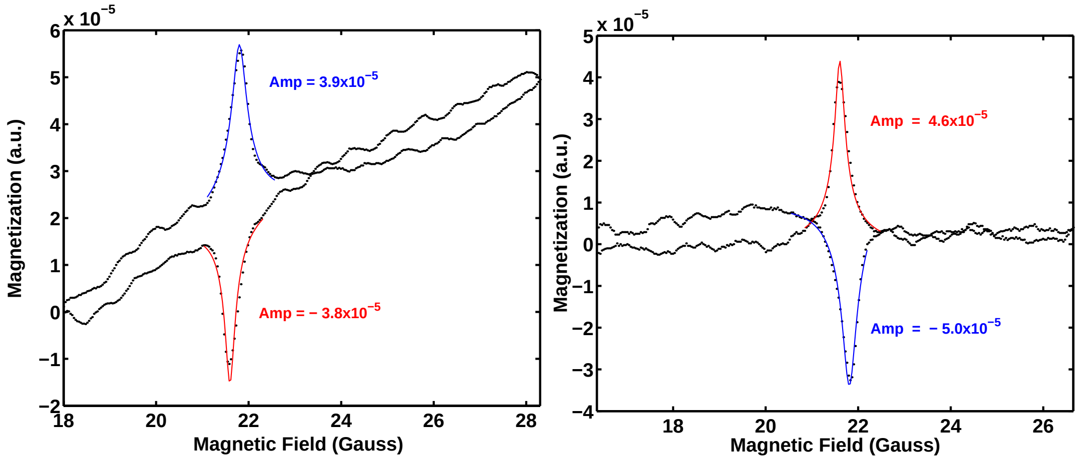

Figure 2.12: Water AFP signals used for calibration of ^{3}He polarization (left) and ^{129}Xe polarization. Left: $A_1 = 3.9 \times 10^{-5}$, $B_{res} = 21.8$ G, $\Delta B_1 = 0.15$ G; $A_2 = -3.8 \times 10^{-5}$, $B_{res} = 21.6$ G, $\Delta B_2 = 0.10$ G. Right: $A_1 = 4.6 \times 10^{-5}$, $B_{res} = 21.6$ G, $\Delta B_1 = 0.1$ G; $A_2 = -5.0 \times 10^{-5}$, $B_{res} = 21.8$ G, $\Delta B_2 = 0.15$ G.

2.3.4 ^{3}He and ^{129}Xe NMR Polarimetry

Before we can compute ^{3}He and ^{129}Xe polarizations, Eq. 2.22 has to be adjusted slightly. To account for the fact that the top cylinder is heated, while the bottom one is not, we need to replace the gas number density n_{NG} with the number density in the bottom cylinder n_b where the NMR signal is measured. We can do so by multiplying n_{HG} with

$$\frac{n_b}{n_{HG}} = \frac{V}{V_b + (V - V_b)\frac{T_b}{T_t}}, \tag{2.24}$$

where V is the total volume of the cell, V_b is the volume of the bottom cylinder, T_b is the temperature in the bottom cylinder (≈ 50°C for ^{3}He and ≈ 40°C for ^{129}Xe), while T_t is the temperature in the top cylinder (150°C for ^{3}He and 100°C for ^{129}Xe). Similarly, the noble gas number density in the top cylinder can be adjusted by computing the factor n_t/n_{HG}, where

$$\frac{n_t}{n_{HG}} = \frac{V}{V + V_b\left(\frac{T_t}{T_b} - 1\right)}. \tag{2.25}$$

Finally, the ratio of the water and noble gas magnetic fluxes through the NMR pick-up coils is proportional to the ratio of the diameters of the bottom cylinders [2]:

$$\frac{\Phi_{H_2O}}{\Phi_{NG}} \propto \frac{r^2_{H_2O}}{r^2_{NG}}. \tag{2.26}$$

^{3}He and ^{129}Xe polarizations can now be computed from Eq. 2.22 using water parameters from Table 2.4 and ^{3}He and ^{129}Xe parameters from Tables 2.5 and 2.6, respectively. For the ^{3}He data displayed in Figure 2.13 we obtain

$$P^{NMR}_{He} = 10.4\%.$$

Similarly, for the ^{129}Xe data displayed in Figure 2.14 the ^{129}Xe polarization is

$$P^{NMR}_{Xe} = 6.5\%.$$

The uncertainties in the parameters are given in Tables 2.4, 2.5 and 2.6. The main sources of systematic uncertainty for water are: the temperature at which the thermal polarization is being evaluated (room temperature of 25°C is assumed), the thickness of the cell's glass and thus the radius of the bottom cylinder, and the amplitude of the signal from the fit. For ^{3}He and ^{129}Xe the main source of systematic uncertainty comes from the fit. An additional error when calibrating the ^{129}Xe signal is due to the adjustment in the Q-curve gain. When all the systematic uncertainties are added in quadrature, we obtain $\approx 7\%$ uncertainty in the ^{3}He and ^{129}Xe NMR polarization measurement.

Helium Parameter		
	Value	Uncertainty
μ_{He}	$-2.12762\mu_N$	-
γ (Hz/G)	3243	-
T_{pump} (^oC)	150	1.2%
f_{RF} (kHz)	92	0.5%
n_{He} (amg)	7.66	1%
n_b/n_{He}	1.11	2.5%
A_{He} (from fit)	0.1675	4%
$G^{amp}{}_{He}$	10	0.5%
$G^{Q}{}_{He}$	1	-
$\Phi_{He} \propto r^2{}_{He}$	$(0.99)^2$	2%

Table 2.5: Parameters related to helium AFP signal.

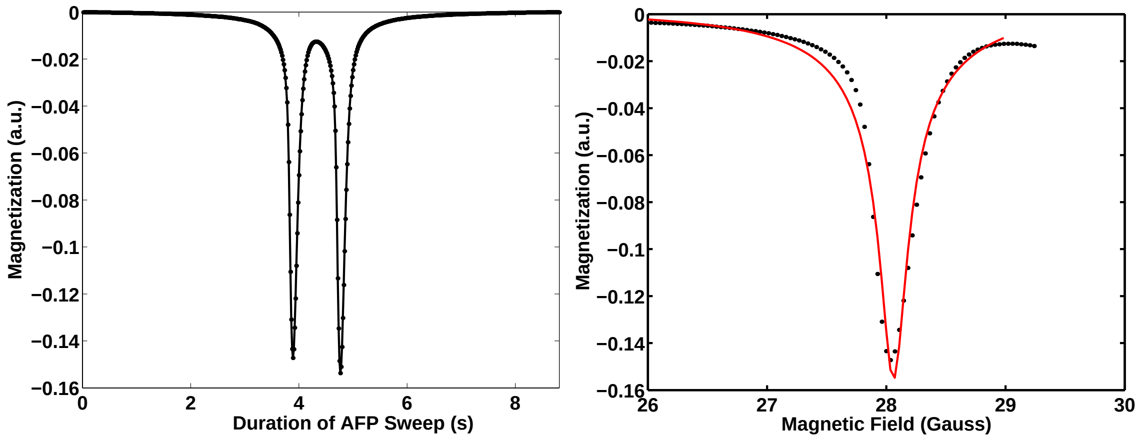

Figure 2.13: Left: ^{3}He AFP signal as a function of time. Right: AFP resonance during the ramp-up time and best fit to the data, $A_1 = -0.1639$, $B_{res} = 28.6$ G, $\Delta B_1 = 0.11$ G.

Xenon Parameter		
	Value	Uncertainty
μ_{Xe}	$-0.7768\mu_N$	-
γ (Hz/G)	1186	-
T_{pump} (^oC)	100	1.3%
f_{RF} (kHz)	33	0.5%
n_{Xe} (amg)	0.024	1%
n_b/n_{Xe}	1.12	2.5%
A_{Xe} (from fit)	1.12×10^{-4}	4%
$G^{amp}{}_{Xe}$	100	0.5%
$G^Q{}_{Xe}$	0.09	2%
$\Phi_{Xe}\propto r^2{}_{Xe}$	$(1)^2$	2%

Table 2.6: Parameters related to xenon AFP signal.

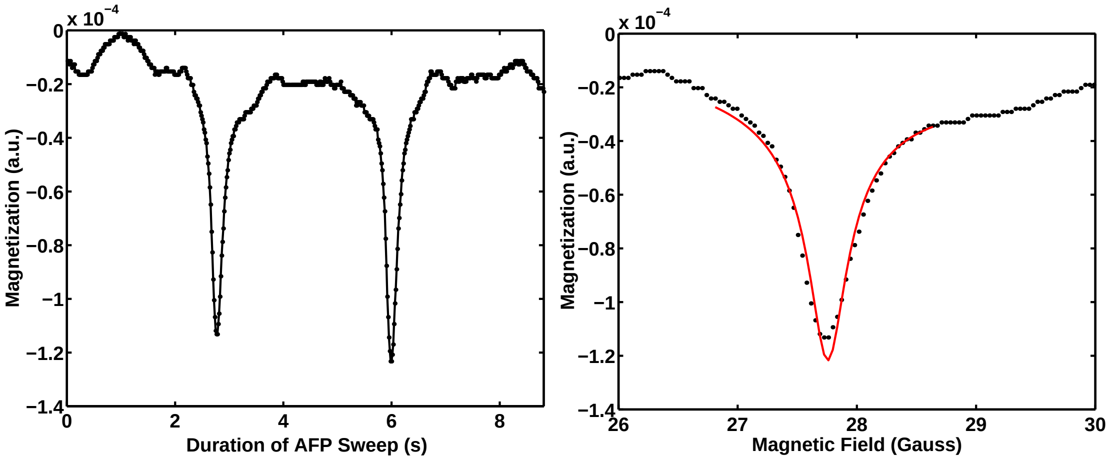

Figure 2.14: Left: ^{129}Xe AFP signal as a function of time. Right: AFP resonance during the ramp-up time and best fit to the data, $A_1 = -1.08 \times 10^{-4}$, $B_{res} = 27.8$ G, $\Delta B_1 = 0.15$ G.

2.4 Hyperpolarized Gas EPR Polarimetry

2.4.1 EPR Polarimetry Principles

Another method for determining the polarization of noble gases is based on the frequency shift of the ^{85}Rb Zeeman resonance (or electron paramagnetic resonance – EPR), which results from the buildup of noble gas polarization. This polarimetry method was first explored on hyperpolarized ^{129}Xe by Schaefer *et al.* [5] and further developed into a robust method for measuring polarization levels of ^{3}He by Newbury *et al.* [4], Barton *et al.* [60] and Romalis *et al.* [3].

The Zeeman resonance is dependent on the background field experienced by the atom. For the $F = I + 1/2$, $m = \pm F$ state, the dependence is expressed in the Breit-Rabi equation [61],

$$\frac{d\nu_{EPR}(F,m)}{dB} = \frac{\mu_B g_e}{h(2I+1)}\left(1 + \frac{8I}{(2I+1)^2}\,\frac{\mu_B g_e B}{hA}\right), \tag{2.27}$$

where μ_B is the Bohr magneton, $g_e = 2.00232$ for the electron and h is the Planck constant. For ^{85}Rb, $I = 5/2$ and $A = 1023$ MHz [3]. In the limit of low magnetic fields (below 10 G [53]), the EPR frequency is proportional to the magnetic field (the constant of proportionality is $\gamma_{Rb}/2\pi = \mu_B g_e/h[2I+1]$). At higher magnetic fields, the contribution from the quadratic term will become progressively more significant.

Apart from the static holding magnetic field, two additional factors influence the background field. First, the magnetization of the noble gas produces a dipole field, B_{dipole}, which adds to the holding field.[8] This classical magnetic field is proportional to the magnetization of the noble gas, $B = C\,M$, where C is a dimensionless constant when using the Gaussian unit system. For a spherical geometry $C = 8\pi/3$. Therefore, the EPR frequency shift due to the classical magnetic field produced by the gas magnetization M is

$$\Delta\nu_M = \frac{d\nu(F,m)}{dB}\,B_{dipole} = \frac{d\nu(F,m)}{dB}\,\frac{8\pi}{3}\,M. \tag{2.28}$$

The second contribution to the background field originates from the Fermi contact interaction which produces spin exchange between the ^{85}Rb electron and the nucleus of the

---

[8] Only the component of the dipole field parallel to the holding field contributes to the EPR shift to a significant degree [3].

noble gas. The EPR frequency shift due to the spin exchange is equivalent to [3]

$$\Delta\nu_{SE} = \frac{d\nu(F,m)}{dB} B_{SE} = \frac{d\nu(F,m)}{dB} \frac{2\,\hbar\, K_{SE}\, \langle v\, \sigma_{SE} \rangle\, n_{NG}}{g_e \mu_B} K_z, \tag{2.29}$$

where K_{SE} is the ratio of the imaginary and real parts of the spin-exchange cross section [3], n_{NG} is the hyperpolarized gas number density, K_z is the z-component of the nuclear spin, and $\langle v\, \sigma_{SE} \rangle$ is the velocity average of the real part of the spin-exchange cross section, σ_{SE}.

The classical (Eq. 2.28) and spin-exchange (Eq. 2.29) contributions to the EPR frequency shift are both proportional to the noble gas polarization $P = K_z/K$, and number density n_{NG}. They can therefore be combined into a single expression,

$$\Delta\nu_{EPR} = \Delta\nu_M + \Delta\nu_{SE} = \frac{8\pi}{3} \frac{d\nu(F,m)}{dB} \kappa_\circ\, \mu_{NG}\, n_{NG}\, P, \tag{2.30}$$

where μ_{NG} is the magnetic moment of the noble gas and $\kappa_\circ$ is a dimensionless constant that depends on temperature, but not on the density or the polarization of the noble gas. Note that if the EPR frequency shift was solely due to the classical field produced by the noble gas magnetization in a spherical geometry, $\kappa_\circ = 1$. Therefore, a value of $\kappa_\circ$ which is bigger than one represents an enhancement resulting from the spin exchange between the Rb electron and the noble gas nucleus.[9] Table 2.7 gives theoretical and experimental $\kappa_\circ$ values for ^{3}He and ^{129}Xe (from [3, 4, 5]).

$\kappa_\circ$ Values	Rb-He	Rb-Xe
Experimental	4.52 + 0.00934 T[°C]	644 ± 260
Theoretical	2.7-8.8	726

Table 2.7: Experimental and theoretical values of $\kappa_\circ$ for Rb-He and Rb-Xe interaction. Rb-He experimental value taken from [3]; Rb-He theoretical value taken from [4]; Rb-Xe experimental and theoretical values taken from [5].

Finally, if we substitute Eq. 2.27 into Eq. 2.30 and express the noble gas polarization in

---

[9] $\kappa_\circ$ is often called the *enhancement* factor.

terms of the EPR frequency shift in a spherical cell, we obtain

$$P_{NG} = \Delta\nu_{EPR} \left\{ \frac{8\pi}{3} \frac{\mu_B g_e}{h(2I+1)} \left(1 + \frac{8I}{(2I+1)^2} \frac{\mu_B g_e B}{hA} \right) \kappa_\circ \, \mu_{NG} \, n_{NG} \right\}^{-1} . \tag{2.31}$$

2.4.2 EPR Electronics

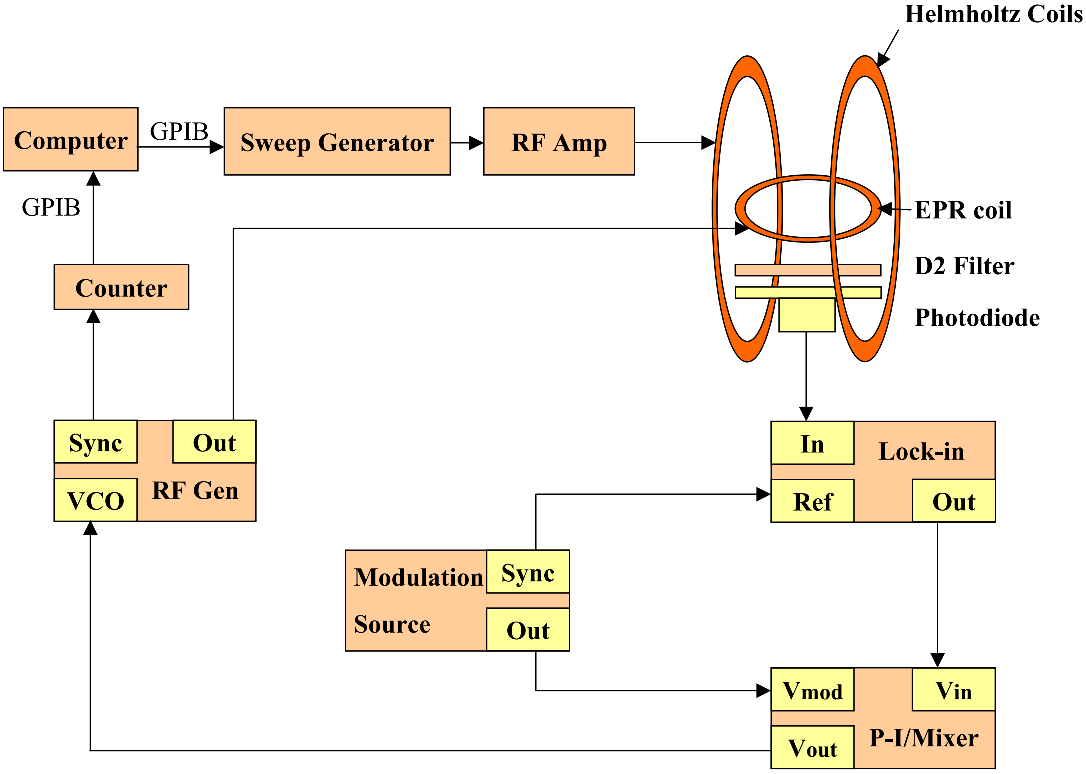

Figure 2.15: Electronic circuitry for EPR detection.

The EPR electronics setup is schematically presented in Figure 2.15. The circuitry detects Rb electron paramagnetic resonance and traces shifts in the central resonant frequency which result from the variations in the background magnetic field.

During optical pumping, most of rubidium vapor is polarized (between 60% and 90% [53]). This means that laser light can penetrate deep into the cell without being absorbed. However, if the level of rubidium polarization is suddenly reduced, the efficiency of optical pumping increases. We made use of this causal relationship during the EPR detection. Rubidium polarization was decreased using a solenoid surface coil (EPR coil) which excited the transitions of rubidium's atoms from the $(F = 3, m_F = 3)$ state to the $(F = 3, m_F = 2)$

state.[10] As the absorption of laser light increases, the decay of atoms back into the ground state increases as well. Most of the atoms are radiationlessly quenched to the ground state by the nitrogen in the cell. However, a small fraction (3-5%) of them [53] decay by emitting either a D1 or D2 fluorescence photon (see Figure 2.1). The D2 fluorescence was detected by a photodiode (*New Focus*, model 2031) and a D2 filter (*Newport*). We chose to detect D2 rather than D1 fluorescence because the laser light, which was also tuned to the D1 transition, could have saturated the photodiode. By monitoring the intensity of D2 transitions as a function of radio-frequency, we would be able to detect the electron paramagnetic resonance.

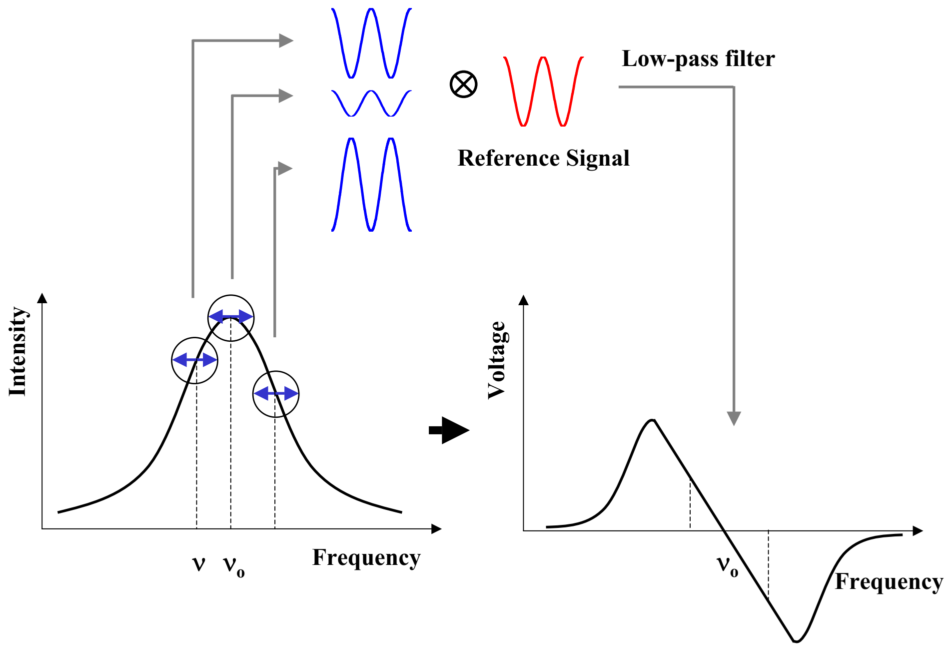

Figure 2.16: Modulation of the Zeeman resonance produces a dispersion curve.

However, instead of monitoring the intensity of D2 fluorescence, we monitored the *changes* in the D2 fluorescence while frequency-modulating the EPR excitation signal. The frequency modulated D2 signal was detected by a lock-in amplifier (*Stanford Research Systems*, model SR830 DSP) which was referenced to the modulation source (*Hewlett Packard*, model 33120A).[11] The lock-in amplifier's output was a DC signal that was proportional

---

[10] Because the magnetic field produced by the EPR coil is linearly polarized along the x-axis, while the Zeeman splitting is along the z-axis, the EPR coil will produce oscillatory transitions from the $m_F = 3 \rightarrow 2$ state as well as from the $m_F = -3 \rightarrow$-2 state. Consequently, the sense of the circular polarization of laser light has no effect on the EPR excitations.

[11] In ^{129}Xe EPR polarimetry experiments, an additional amplifier (*Stanford Research Systems*,

to the RMS (root-mean-square) voltage of the modulated D2 fluorescence[12]. For instance, modulating the central frequency of the EP resonance gives a zero DC signal, while modulating the frequency which is to the left of the central resonance results in a positive DC signal. Consequently, the output of the lock-in amplifier produced a derivative of the D2 resonance, which is a dispersion curve. This is depicted in Figure 2.16. To see this formally, consider a signal intensity I around a frequency point $\nu_\circ$. If the frequency is modulated with a modulation signal of amplitude $\Delta\nu$ and frequency ν_{mod}, then the signal intensity can be written as $I\left(\nu_\circ + \Delta\nu \sin\left(2\pi\nu_{mod}t\right)\right)$. In the limit of small modulation amplitudes, the signal intensity can be expended in a Taylor series:

$$I\left(\nu_\circ + \Delta\nu \sin\left(2\pi\nu_{mod}t\right)\right) \approx I(\nu_\circ) + \frac{dI}{d\nu}\Delta\nu \sin\left(2\pi\nu_{mod}t\right). \tag{2.32}$$

The $I(\nu_\circ)$ term is a DC offset which is removed when using AC coupling on the lock-in amplifier. The second term, $\frac{dI}{d\nu}\Delta\nu \sin\left(2\pi\nu_{mod}t\right)$, is a sine wave of amplitude $\frac{dI}{d\nu}\Delta\nu$ and frequency ν_{mod}. The output of the lock-in will be proportional to the RMS voltage of this signal and, therefore, to the derivative of the resonance $dI/d\nu$. Furthermore, if $\Delta\nu$ is small enough so Eq. 2.32 is a valid approximation, the lock-in output is also proportional to $\Delta\nu$, which means that a bigger EPR signal can be produced by increasing $\Delta\nu$ (see region of linearity near $\nu_\circ$ in the dispersion curve of Figure 2.16). In practice, $\Delta\nu$ was approximately one third of the resonance width (see Table 2.8 for the parameter values used in the EPR measurement).

The derivative of the D2 resonance served as a feedback signal to trace shifts in the central frequency of the EPR curve [5]. When the frequency of excitation matches the EP resonance, the derivative and thus the feedback signal are zero. When the frequency is less than the resonant frequency, the derivative is a positive signal. If this positive signal is converted into a positive frequency shift, the radio-frequency could be shifted back to the resonance.

The feedback was achieved with the proportional integrator shown in Figure 2.17. The

---

model SR560) was used to amplify and filter the signal from the photodiode before detecting it by a lock-in amplifier.

[12] The lock-in amplifier multiplies the input signal with the reference signal of a specific frequency and then passes this product through a low-pass filter which performs the averaging (integration) of the product. After the integration, the only nonzero component results from part of the input signal which was at the same frequency as the reference frequency.

EPR Parameters	He	Xe
Frequency Sweep (kHz)	92-30	43-3
B(Gauss)	18.9	18.9
f_{Res} (kHz)	61.3	22.4
Pre-Amp Gain	-	2
Lock-in Time Constant (s)	0.3	0.3
Modulation Freq. (Hz)	300	300
Modulation Amp. (kHz)	+/- 20	+/- 20
EPR Frequency (MHz)	8.8	8.8
RF Amp Gain (Volts)	50	50

Table 2.8: Parameter values during the EPR-AFP experiment.

output of the mixer which adds the modulation signal and the feedback was sent to a voltage controlled oscillator input of a RF function generator (*Wavetek*, model 80). The VCO converted the amplitude of the input signal into a frequency offset. The output of the RF function generator was therefore: $\nu_{RF} = \nu_{\circ} + \nu_{feedback} + \Delta\nu \sin(2\pi\nu_{mod}t)$, where $\nu_{\circ}$ was set on the function generator, $\nu_{feedback}$ was the frequency shift resulting from the lock-in output and the proportional integrator, and the last term was due to the modulation signal. A counter (*Hewlett Packard*, model 53181A) was used to read off the frequency from the RF function generator, while a LabView program recorded the values on the counter.

To isolate the shift in the EPR frequency due to the magnetization of noble gas, the gas magnetization was flipped by 180° using adiabatic fast passage method described in Chapter 2.3.1.1. However, unlike in the NMR polarimetry, we swept the frequency rather than the magnetic field because the magnetic field had to be stable during the EPR measurement. Figure 2.18 shows, schematically, the change in the EPR frequency when the noble gas magnetization is flipped by 180°. Recording the EPR frequency before and after the AFP flip enables an estimation of the EPR shift and, consequently, the noble gas polarization. Formally, $\Delta\nu_{EPR} \propto \{B_z + M_{NG} - (B_z + M_{NG})\} \propto 2M_{NG}$.

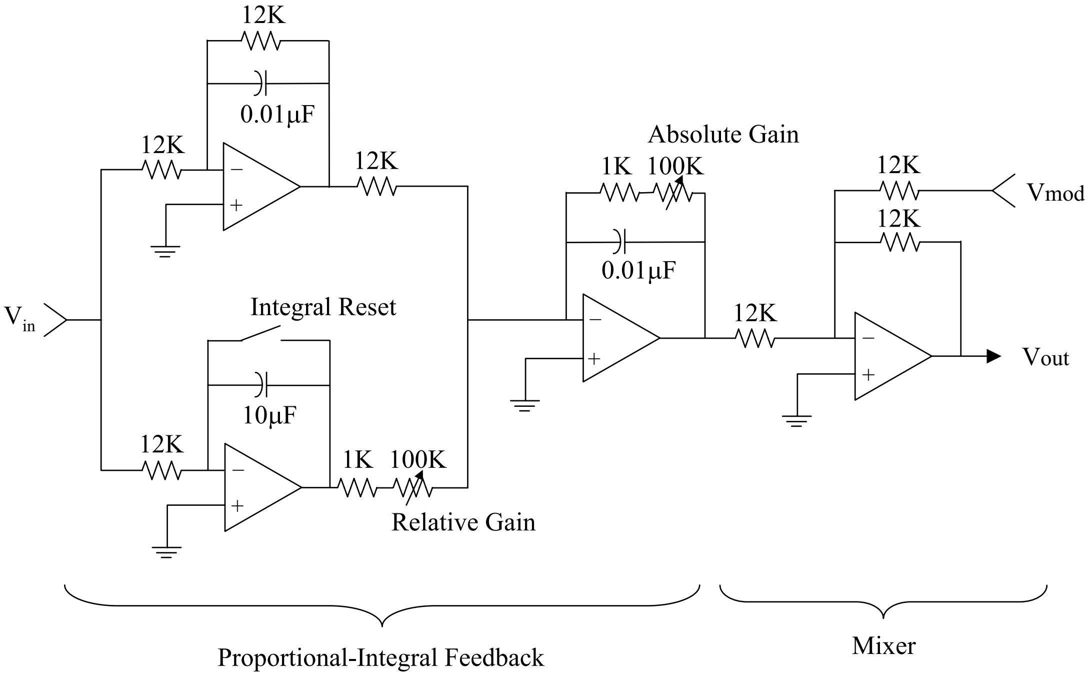

Figure 2.17: Proportional-integral feedback and mixer circuitry.

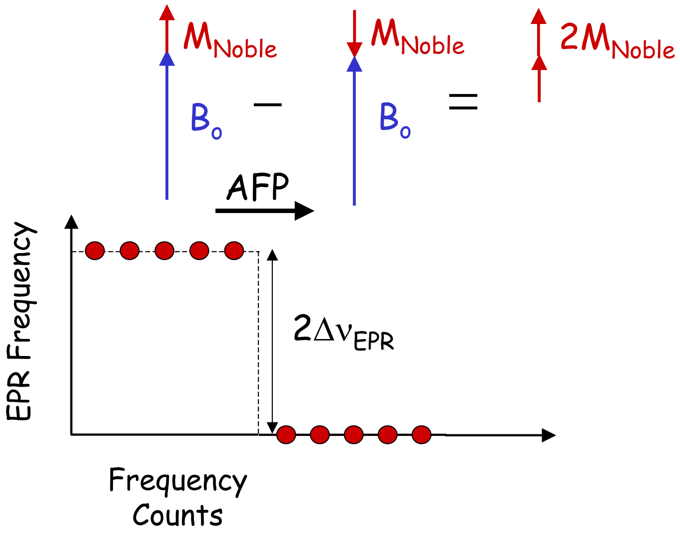

Figure 2.18: Schematics of EPR frequency before and after AFP flip.

2.4.3 ^{3}He and ^{129}Xe EPR Polarimetry

Using the parameter values listed in Table 2.9 we can simplify Eq. 2.31 so that

$$P_{NG} = 0.862 \left[\frac{amg}{kHz}\right] \frac{\Delta\nu_{EPR}}{\kappa_\circ \, n_{NG} \left(\frac{n_t}{n_{NG}}\right)}, \tag{2.33}$$

where we used the fact that $[\text{amg} \cdot \text{erg/G}] = 44.5 \times 10^{-6}\,\text{N}_\text{A}[\text{G}]$, where N_A is the Avogadro constant. Also, since the EPR signal is acquired in the top chamber, the hyperpolarized gas number density had to be adjusted by the factor n_t/n_{HG}.

ERP-related Parameters	Value
μ_B (erg/G)	9.2741×10^{-21}
γ (kHz/G)	466
h (erg s)	6.626×10^{-27}
I(^{85}Rb)	5/2
g_e	2.00232
A (MHz)	1023

Table 2.9: Parameter values related to EPR Polarimetry.

	^{3}He EPR		^{129}Xe EPR	
	Value	Uncertainty	Value	Uncertainty
n_{HG} (amg)	7.66	1%	0.02422	1%
n_t/n_{HG}	0.85	2.5%	0.72	2.5%
μ_{HG} (erg/G)	-1.0746×10^{-23}	-	-3.9230×10^{-24}	-
κ_o	4.52 + 0.00934 T[°C]	1.5% (i) 1.3% (ii)	726	(theory estimation)
$\Delta\nu_{EPR}$	4533	6%	1812	50%

Table 2.10: Helium and xenon parameters used in EPR polarimetry. (i)Uncertainty related to $\kappa_\circ$ measurement. (ii)Uncertainty due to the non-spherical shape of the cell.

The ^{3}He EPR signal is shown in Figure 2.19. This data was collected immediately after collecting ^{3}He NMR-AFP data displayed in Figure 2.13. Therefore, the polarizations obtained with the EPR and NMR methods should agree within the error bars. From the data in Figure 2.19 we find that $\Delta\nu_{EPR} = 4533 \pm 270$ Hz. Using Table 2.10, ^{3}He polarization is

$$P_{He}^{EPR} = 10.2\%.$$

The main uncertainty in the ^{3}He EPR data comes from the estimation of the EPR shift. Due to background field instability, the EPR frequency shifts with time. For the data displayed in Figure 2.19 the standard deviation of frequency shift was ±265 Hz. However, the frequency shift can be even bigger if the feedback does not function properly. In addition, since the cells used in our experiments were cylindrical rather than spherical, the enhancement factor $\kappa_\circ$ has an additional 1.3% uncertainty associated with it [3]. The total uncertainty in the estimation of ^{3}He polarization using the EPR polarimetry method was thus ≈ 7%.

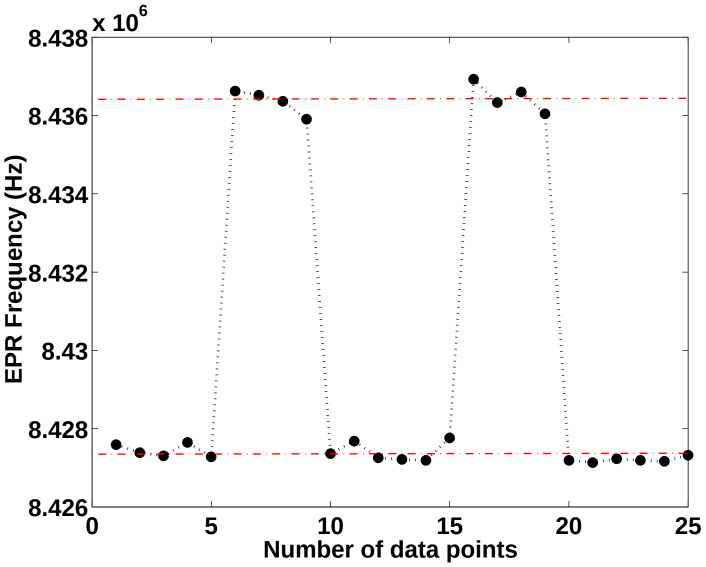

Figure 2.19: Helium EPR frequency shifts after AFP flip.

To analyze our ^{129}Xe EPR data, it is useful to compute the predicted frequency shift due to 6.5% ^{129}Xe polarization, as indicated by the NMR polarimetry data. Using the parameter values listed in Table 2.10 and relying on the theoretical value for Rb-Xe $\kappa_\circ$ constant, we obtain a frequency shift of approximately 500 Hz. Although the total frequency shift after an AFP flip should be around 1 kHz, our measurements gave a shift on the order of 3.5 kHz

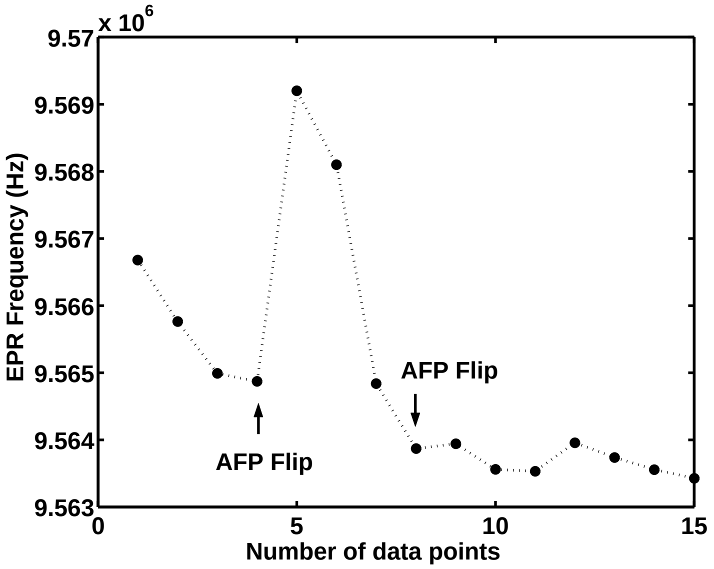

Figure 2.20: A preliminary xenon EPR frequency shift after one AFP flip.

(Figure 2.20). However, the uncertainty in this measurement is large due to the following possible reasons:

1. The background EPR frequency in Figure 2.20 is shifting significantly, either due to the magnetic field instability or due to poor feedback control. The magnetic field instability could be reduced, in the future, by using a magnetic flux magnetometer to monitor the magnetic field and correct for the field jitter (or drift) by employing a feedback loop similar to the one used in the EPR polarimetry. Romalis *et al.* [3] used a flux-gate magnetometer for ^{3}He EPR polarimetry measurements. The feedback control, on the other hand, was challenging due to the small Rb resonance signals generated in the ^{129}Xe cell in contrast to the ^{3}He cell. Because optical pumping of ^{129}Xe cell is performed at 80°C when Rb-^{129}Xe spin-exchange is most effective, while optical pumping of ^{3}He requires temperatures of around 150°C, the rubidium number density in the ^{129}Xe cell is two orders of magnitude smaller than in the ^{3}He cell. Since the intensity (amplitude) of the detected D2 light is proportional to the number of Rb transitions, this reduction in temperature leads to a small Rb resonant signal. In the future, we could try to polarize ^{129}Xe at 80°C, and then increase the temperature to 150°C to detect the Rb resonance. However, since the spin-destruction rate due to Xe-Rb collisions would increase at higher temperature, the relaxation time of hyperpolarized gas would decrease as well.

2. Figure 2.20 also indicates that after the initial AFP flip the ^{129}Xe polarization was lost, as there is no observable shift after the second AFP flip. Furthermore, judging from the decay of the EPR frequency immediately after the initial shift, it appears that the ^{129}Xe magnetization decayed while being anti-aligned with the magnetic field. This could occur, for instance, if the AFP flip was incomplete. If the gas magnetization was partly left in the transverse plane, the gas would be subject to T_2^* decay (i.e., decay due to the field inhomogeneities; see Chapter 4 for further details.). More importantly, if the lifetime (i.e., $1/\Gamma$) of the cell was very short (on the order of one minute), then the gas magnetization would have decayed to zero in time $t = \ln 2/(\gamma_{SE} + \Gamma) \approx 40$ s, where the spin-exchange rate γ_{SE} is on the order of 10^{-4} s^{-1} for ^{129}Xe at 90°C. Since each point in Figure 2.20 was an average over 5 s, the gas magnetization was anti-aligned with the magnetic field for 20 s. For a cell with poor lifetime, this could have been long enough for polarization to decay to zero.

3. An additional obstacle in implementing EPR polarimetry on ^{129}Xe is the fact that ^{129}Xe is best polarized at low gas pressures [45]. Low number density results in low gas magnetization levels and, therefore, in an inherently small average EPR frequency shift. EPR polarimetry is for now best suited for high-pressure ^{3}He targets used in nucleon spin structure function experiments which produce large frequency shifts (10 kHz and more).

2.5 Concluding Remarks

We have successfully implemented the EPR polarimetry for measuring polarizations of hyperpolarized ^{3}He. By measuring the EPR frequency shift in rubidium, we estimated $10.2\% \pm 0.7\%$ of ^{3}He polarization. This result was supported by NMR polarimetry data, which gave a ^{3}He polarization of $10.4\% \pm 0.7\%$. The ^{129}Xe EPR data had large uncertainty associated with it, due, in part, to small rubidium resonance signal and large background field variation. Nevertheless, the preliminary ^{129}Xe EPR shift sets a limit on the Rb-^{129}Xe enhancement factor.

Chapter 3

The Pulsed Resistive Low-Field MR Scanner

3.1 Background

In the remaining part of this work we are going to describe hyperpolarized gas relaxation, diffusion and MR imaging experiments. These experiments were performed on a pulsed resistive low-field scanner that was constructed at Stanford University for low-field high-resolution imaging of water using the "prepolarized MRI" technique (or PMRI). In this chapter, we motivate the construction of a hybrid hyperpolarized gas/proton MRI scanner by exploring signal-to-noise (SNR) properties of hyperpolarized gas and prepolarized water during MRI. In addition, we describe the principles behind prepolarized water MRI, the pulse sequence used in the PMRI experiments and the electronics components of the pulsed resistive low-field scanner.

Conventional MRI techniques require a magnetic field that is both strong and homogeneous. The strength of the field determines the extent of magnetization induced in the sample, while the variation in the field (i.e, inhomogeneity) has to be smaller than the size of the gradients used during imaging. Such fields are usually produced by large and heavy static magnets or by cryogenically cooled and thus expensive superconductors. An alternative approach is the prepolarized MRI technique in which two separate pulsed fields produced by two different magnets–a polarizing magnet and a readout magnet–assume the role of the conventional $B_\circ$ field [62, 25].

In PMRI, the polarizing magnet produces a strong (0.35 T) yet inhomogeneous magnetic field which determines the sample's magnetization, and consequently, the signal-to-noise ratio (SNR) of the MR image. The 20% inhomogeneity of the magnet causes the net magnetization to vary across the sample. However, such variations are gradual and smooth, and since human vision is insensitive to smooth variations of this order, the MR image quality is not affected by the inhomogeneity of the polarizing magnet. In fact, clinicians now routinely image with variations of several hundred percent when using surface coils.

The readout magnet produces a relatively weak (0.025 T) yet homogeneous field which is applied after the spins have been polarized by the polarizing field to produce the Larmor precession of spins needed for MR detection. Unlike the polarizing field, the readout field has to be extremely homogeneous, since dispersion in the Larmor frequency of a spin ensemble leads to spin de-coherence (i.e, dephasing) and thus to MR signal loss. On the other hand, the strength of the readout field has no effect on the SNR of the image, provided the sample completely loads the RF coil. Therefore, the readout field needs only to be large enough to dominate the Earth's field and thus to provide an axis of magnetization for the precessing spins.

In order to combine the polarizing and the readout magnet into a single MR scanner–which would allow for a polarizing and a readout phase in the pulse sequence–the two electromagnets have to operate as pulsed, rather than as static magnets. It is this pulsed (or field-cycled) property of the system that makes building such a system technically challenging [25]. In addition, the energy stored in the polarizing field must be small enough to facilitate field-cycling, so the PMRI concept is most applicable for imaging relatively small samples, such as human extremities (knee, head, hands) [24]. Finally, the excessive power dissipation (greater than 10 kW) poses additional challenges at readout fields above 0.35 T.

One of the potential advantages of the PMRI (i.e, low-field pulsed resistive) system is that the pair of resistive electromagnets can be manufactured at a greatly reduced cost as compared to a single superconducting magnet. This has the potential to make routine imaging, which is necessary in disease control and treatment monitoring, more feasible as well as accessible to a larger fraction of the population. Furthermore, because of the low readout field strengths used, the PMRI system has all the advantages of a low-field scanner, such as smaller susceptibility effects and reduced RF power deposition, without the usual cost in image SNR.

However, it is the field-cycled nature of the polarizing and readout fields that holds the most promise for novel MR applications. Changing the strength of the polarizing pulse enables the investigation of rich T1 dispersion-based MR contrast [63], while varying the strength of the readout pulse makes the system suitable for imaging substances other than water (such as hyperpolarized gases–^{3}He and ^{129}Xe) without the need to re-tune the RF coils.

3.2 Signal-to-Noise Ratio in MRI, PMRI and Hyperpolarized Gas MRI

3.2.1 MR Signal

The source of MR signal is the precession of nuclear magnetization in a $B_\circ$ field. The transverse component of the precessing magnetization induces a voltage at the receiver coil input according to Faraday's law of induction. To quantify this signal, we can look at the magnetization in a voxel of size dV, $\mathbf{M}(t, \mathbf{r})dV$, placed at a point P away from a conductor. The time-varying magnetization induces a voltage V(t) in the conductor. If instead, the conductor carried a current I(t), it would produce a magnetic field of size $\mathbf{B_1}$ at point P. Employing the Lorentz Reciprocity theorem [23, 22], it can be shown that

$$\mathrm{V(t)} \otimes \mathrm{I(t)} = -\int_V \mathbf{B_1} \otimes \frac{\partial \mathbf{M}(t, \mathbf{r})}{\partial t}\, dV \tag{3.1}$$

The solution to the rotating magnetization can be represented in complex notation as

$$\mathbf{M}(t, \mathbf{r}) = \mathbf{M}_\circ \left\{exp(-i\omega t) + \text{other terms}\right\}, \tag{3.2}$$

where $\mathbf{M}_\circ$ is the nuclear magnetization, ω is the Larmor frequency of precession, and "other terms" could represent the T_2 relaxation (decay) of the transverse component, $exp(-t/T_2)$, or precession in an imaging gradient $\mathbf{G}$, $exp(-i\gamma \int \mathbf{G}(\tau) \cdot \mathbf{r} d\tau)$.[1] The nuclear magnetization is given (in SI units) by

$$\mathbf{M}_\circ = N\gamma^2\hbar^2 I(I+1)\mathbf{B}_\circ/3kT, \tag{3.3}$$

where N is the number of spins at resonance per unit volume, γ is the gyromagnetic ratio of nuclei and T is the temperature of the sample. If we insert Eq. 3.2 into Eq. 3.1 and then differentiate with respect to time, we get

$$s(t) = -i\omega B_1 M_\circ\, exp(-i\omega t)\, dV, \tag{3.4}$$

---

[1] These terms are avoided because they are irrelevant in the present derivation.

where we assumed unit current I(t) and replaced the voltage symbol V with $s(t)$ to describe the NMR signal. If the NMR signal is averaged over the acquisition time, then

$$S \propto \omega B_1 M_\circ \, dV \sqrt{T_{acq}}. \tag{3.5}$$

In conventional MRI, the frequency of precession and the magnetization of the sample are both proportional to the applied field $B_\circ$ ($\omega \propto B_\circ$, $M_\circ \propto B_\circ$), so that the NMR signal varies as the square of the $B_\circ$ field,

$$S_{MRI} \propto B_\circ^2 B_1 \, dV \sqrt{T_{acq}}. \tag{3.6}$$

On the contrary, in PMRI, the readout field B_r determines the Larmor frequency of precession, so that $\omega \propto B_r$, while the polarizing field B_p determines the sample's magnetization, $M_\circ \propto B_p$. Therefore, the signal of prepolarized water is linear in both the polarizing and the readout magnetic field strengths:

$$S_{PMRI} \propto B_r B_1 B_p \, dV \sqrt{T_{acq}}. \tag{3.7}$$

Like prepolarized water, hyperpolarized noble gas magnetization is not a function of the readout field strength; rather, it is determined by the efficiency of the optical pumping and the spin-exchange processes which are used to polarize the nuclear spin of the noble gas (see Chapter 2). As in PMRI, Larmor frequency is determined by the strength of the readout field B_r. The hyperpolarized gas MR signal is then proportional to

$$S_{HypGas} \propto B_r B_1 \mu_\circ M_{gas} \, dV \sqrt{T_{acq}}, \tag{3.8}$$

where M_{gas} represents the gas magnetization and $\mu_\circ$ is the permeability of free space.

3.2.2 Noise in MRI

The main source of noise in MR arises from random electrical fluctuations created by Brownian motion of electrons in a conductor. Such noise (also called "resistive" or Johnson noise) is thermal in origin, adds linearly to the signal and can be modelled as Gaussian-distributed.

The mean square voltage induced by the random motion of electrons in a conductor of resistance R, temperature T and bandwidth Δf is[2]

$$\langle \mathrm{V}^2 \rangle = 4kTR\Delta f. \tag{3.9}$$

Because Johnson noise is due to random processes, the average noise voltage is zero. Therefore, to account properly for random noise sources in MR, one has to consider the RMS (root-mean-square) values of noise. When uncorrelated, the noise power from different thermal sources has to be added.

There are two main sources of thermal noise in MRI: the receiver coil (with resistance R_c), and the body (or sample) as seen by the receiver coil (with resistance R_s). In general, the coupling between the body and the receiver coil is inductive as well as capacitive. However, only inductive coupling is required for MR signal detection.[3] The capacitive coupling occurs when quasi-static electric fields produced by the coil penetrate the body. Since capacitive coupling in tissue creates an additional resistive noise source, it should be minimized through proper design and shielding of RF coils.

To determine the variation of noise with frequency, one needs to examine how the coil and the body resistance vary with the frequency of transmission. The body resistance R_s varies as the square of Larmor frequency [22]. The coil resistance, on the other hand, depends on factors such as resistivity of the conductor, coil geometry (coil radius and the number of turns), proximity fields and skin depth of the conductor at the particular radio frequency [23]. Since the coil resistance is inversely proportional to its skin depth, and skin depth is proportional to $f_\circ^{-1/2}$, the coil resistance grows as $f_\circ^{1/2}$. Summarizing,

$$\begin{array}{lllll} N_s & \propto & \sqrt{\langle V^2 \rangle_s} & \propto & \sqrt{f_\circ^2} \\ N_c & \propto & \sqrt{\langle V^2 \rangle_c} & \propto & \sqrt{f_\circ^{1/2}}, \end{array} \tag{3.10}$$

where N_s is the noise induced by the sample, while N_c is the noise induced by the coil.

Apart from the body and coil noise, there are other sources of noise, such as the noise coming from the receiver preamplifier, the matching network, and other electronics. However, under normal operational conditions, these noise sources should be negligible compared to the body and coil noise.

---

[2] Since the power density (i.e., power per bandwidth, $P/\Delta f$) is independent of the frequency band, the noise is often referred to as "white".

[3] The inductive coupling between the body and the coil produces the MR signal.

3.2.3 SNR in PMRI and Hyperpolarized Gas Imaging

The SNR is defined as the ratio between the signal strength and the noise. Since the signal in MR is measured as a potential difference (i.e., voltage) induced in the receiver coil, the SNR becomes the ratio between the signal voltage and noise voltage. For PMRI, the SNR is derived from Eqs. 3.7 and 3.10,

$$SNR_{PMRI} = \frac{S_{PMRI}}{N_s + N_c} \propto \frac{B_\circ B_p}{\sqrt{\alpha B_\circ^2 + \beta B_\circ^{1/2}}}\,, \tag{3.11}$$

where α and β are proportionality constants coming from Eq. 3.10.

Similarly, for hyperpolarized gas MR, the SNR is derived from Eqs. 3.8 and 3.10,

$$SNR_{Hyp\,Gas} \propto \frac{B_\circ \mu_\circ M_{Xe}}{\sqrt{\alpha B_\circ^2 + \beta B_\circ^{1/2}}}\,. \tag{3.12}$$

One needs to compare the above equations with the expression for the SNR obtained with conventional MRI,

$$SNR_{MRI} \propto \frac{B_\circ^2}{\sqrt{\alpha B_\circ^2 + \beta B_\circ^{1/2}}}\,. \tag{3.13}$$

There are two main SNR regimes in MR imaging, depending on whether the body or the coil is the dominant source of noise. If the imaging frequency is high enough to create significant RF eddy currents, then the body can be the dominant source of noise. This noise regime is called "body-noise dominance". On the other hand, in cases such as low-field imaging or small volume imaging, the receiver coil presents the dominant source of noise. The noise regime is then called "coil-noise dominance". In the body-noise and coil-noise dominant regimes, Eqs. 3.13, 3.12 and 3.11 reduce, respectively, to

Body-noise dominance

$$\begin{aligned} SNR_{MRI} &\propto B_\circ \\ SNR_{Hyp\,Gas} &\propto \mu_\circ M_{Xe} \\ SNR_{PMRI} &\propto B_p\,, \end{aligned} \tag{3.14}$$

Coil-noise dominance

$$\begin{aligned} SNR_{MRI} &\propto B_\circ^{7/4} \\ SNR_{Hyp\,Gas} &\propto B_\circ^{3/4} \mu_\circ M_{Xe} \\ SNR_{PMRI} &\propto B_\circ^{3/4} B_p\,. \end{aligned} \tag{3.15}$$

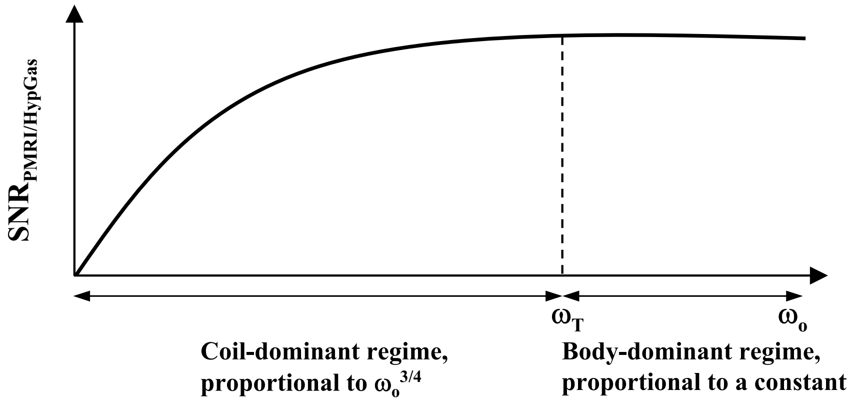

Figure 3.1: SNR as a function of readout frequency for PMRI and hyperpolarized gas MR. The transitional frequency, ω_T, is defined as the frequency at which the coil and the body contribute equal amount of noise. Well below ω_T, the SNR grows as a function of $\omega_\circ^{3/4}$, while well above ω_T, the SNR approaches its asymptotic limit.

The SNR relationships can also be illustrated graphically. Figure 3.1 shows the SNR properties for pre-polarized and hyperpolarized MRI. In the body-noise dominant regime (at readout frequencies at which the noise is dominated by the sample), the SNR of pre-polarized and hyperpolarized gas MRI is independent of the imaging frequency. This means that when body-noise dominance is achieved, there is little benefit to increasing the magnetic field above the transitional frequency (ω_T in the plot).[4] This behavior sharply distinguishes PMRI and hyperpolarized gas MRI from conventional MRI, in which the SNR grows with the strength of the imaging $B_\circ$ field in both noise regimes–a fact which justifies the construction of high-field imaging scanners. In addition, comparing the SNR relationships in Eq. 3.14 for all three imaging modalities, we see that pre-polarized MRI can achieve the same SNR as conventional MRI if the strength of the polarizing field B_p in PMRI is equal to the strength of the imaging field $B_\circ$ in conventional MRI. In other words, the SNR of water which has been pre-polarized with a 0.5 T polarizing pulse should be the same as the SNR of water imaged in a 0.5 T static field scanner.

The strength of the transitional frequency in Figure 3.1 depends on the sample size, conductivity, and the geometry and temperature of the receiver coil. For chest-sized coils

---

[4] 70% of the SNR lies in the region below the transitional frequency.

used in pulmonary imaging, the transitional frequency is believed to be at or below 1 MHz (30 mT for ^{3}He and 85 mT for ^{129}Xe) [20]. Darrasse *et al.* [47], achieved body-noise dominance at 0.1 T using a body-coil. Magnetic fields of 0.1 T are easily achieved with resistive magnets thus making imaging of pre-polarized water and hyperpolarized gas feasible at low magnetic field strengths without the need for expensive superconductive magnets and without the penalty in SNR.

3.3 PMRI Pulse Sequence

Due to the pulsed nature of the polarizing and readout fields, the pulse sequence for PMRI is more complicated than for conventional MRI. Figure 3.2 shows a typical pulse sequence used in pre-polarized MRI.

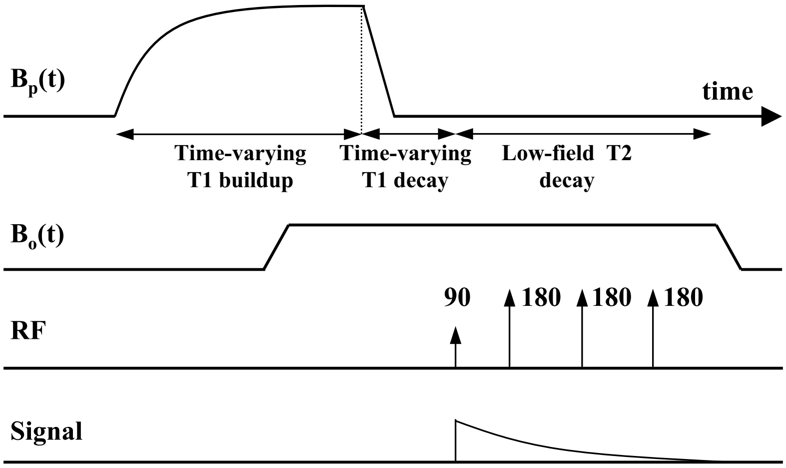

Figure 3.2: Timing diagram illustrating a typical PMRI sequence. B_p is the waveform of the polarizing pulse and $B_\circ$ is the waveform of the readout magnet.

First, a polarizing waveform is applied prior to any RF excitation which governs the build-up of longitudinal magnetization according to the Bloch equation for the z-component of M (written in the rotating frame of reference),

$$\frac{dM_z}{dt} = -\gamma \; M_y \; B_1 + \frac{M_\circ(t) - M_z}{T_1}, \tag{3.16}$$

where $M_\circ(t)$ is the thermal equilibrium polarization at time t defined in Eq. 3.3, but with $B_p(t)$ replacing the $B_\circ$ term; M_z and M_y are the z and y-components of nuclear magnetization at time t; B_1 is the RF field; and T_1 is the longitudinal relaxation time which governs the relaxation of magnetization towards its thermal equilibrium along the z-axis. Equation 3.16 can be simplified by noting that $M_y \approx 0$ throughout the application of the polarizing pulse which is directed along the z-axis. The solution is then

$$M_z = M_\circ(t) + (M_z(0) - M_\circ(t)) \exp\left(\frac{-t}{T_1}\right). \tag{3.17}$$

$M_z(0)$ is the longitudinal magnetization at time $t = 0$, that is, before the onset of the polarizing pulse, when the only magnetic field present is the Earth's field. Since the Earth's field is only 0.5 gauss, $M_z(0)$ is negligibly small and can be ignored.

Note that in PMRI, $M_\circ$ is a function of time, because the polarizing field is a time-varying (i.e., pulsed) field rather than time-independent (i.e., static) field. To solve the above equation exactly, we would need to know the waveform of the polarizing pulse $B_p(t)$. However, if $t >> T_1$, we can assume, to first order, that $M_z = M_\circ(t \rightarrow \infty) \equiv M_p = N\ \mu^2 B_p^{max}/3kT$, where $\mu^2 = \gamma^2\hbar^2\, I(I+1)$. In other words, for sufficiently long polarizing pulses[5], the magnetization achieved can be computed from the maximum (limiting) value of B_p. Since $B_p = 0.5\ T$, the PMRI scanner can achieve a T_1-weighted contrast comparable to mid-field (0.5 T-1.5 T) scanners.

The B_p field must be ramped down to a size smaller than 1 μT (see calculations in Section 3.4.1) before application of the RF pulse and the signal acquisition, otherwise the large (20%) inhomogeneity of the polarizing field will dominate over the imaging gradients, distort the spatial encoding of the object and add phase-shifts. In addition, the quenching of the field must be fast so as to minimize T_1 relaxation during the ramp-down period. Experiments by the Stanford group showed that less than 20% of the magnetization was lost, if the polarizing magnet was ramped down faster than 80 ms [64]. Section 3.4.2 explains how the fast quenching of the field was achieved.

The ramping-down (changing of the current and the magnetic flux) of the polarizing field induces an *emf* (voltage) in the readout magnet, $\epsilon_2 = -\frac{d\Phi_2}{dt} = -M_{21}\frac{dI_1}{dt}$, where ϵ_2 is the *emf* induced in the readout magnet, Φ_2 is the magnetic flux through the readout magnet, M_{12} is the mutual inductance of the magnets ($\approx$ 52 mH), and dI_1/dt is the current change in the polarizing magnet. Since the disturbances in the readout magnet must be below ppm levels (see Section 3.4.1 for detailed calculation), the current in the readout magnet must be controlled precisely using feedback. Switching the readout magnet on before the ramp-down of the polarizing magnet insures that the target field is reached at the end of the ramp-down. Since the self-inductance L of the readout magnet has a stray capacitance C_s and stray resistance R_s associated with it, the disturbances in the readout magnet voltage cause ringing. By implementing critical damping, the ringing time was reduced from 200 ms to less than 15 ms [65].

---

[5] Typically, $t = 3T_1$ was used in PMRI experiments.

The RF pulse, which tips the magnetization away from the z-axis, can only be applied after the transients subside. Signal acquisition can occur when the dual-mode RF circuitry switches from the transmit to the receive mode. During signal acquisition, only the readout field is present, so the frequency of precession (and acquisition) is governed by the low readout field. Furthermore, the readout field determines the T_2 relaxation rate; however, since T_2 is for most nuclei independent of the magnetic field strength, the PMRI scanner achieves T_2-weighted contrast comparable to high field scanners.

3.4 Electronics of the Pulsed Low-Field Resistive System

3.4.1 Readout Magnet and Power Supply

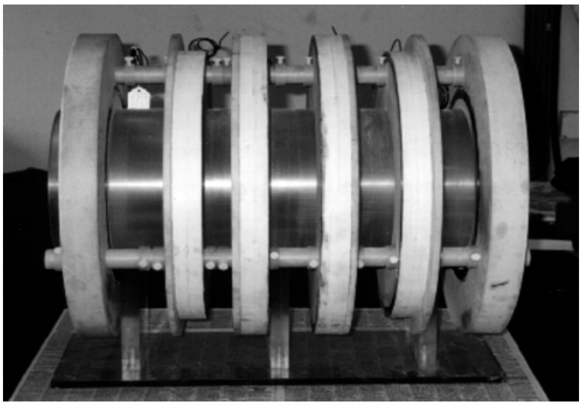

Figure 3.3: Photograph of the homebuild 24 cm bore, 23 mT, 1 kW homogeneous readout magnet for PMRI of extremities. This magnet was used in the hyperpolarized gas experiments.

Ideally, the PMRI readout magnet (Figure 3.3) is designed to operate at a frequency at which the body becomes the dominant source of noise (ω_T in Figure 3.1). The 110 kg homebuild magnet used in the experiments described in this work was designed to operate at 23 mT, but could create a field up to 35 mT, which corresponds to a frequency of 1.49 MHz for water, 415 kHz for ^{129}Xe and 1.14 MHz for ^{3}He. At 23 mT, it required a current of 13 A and dissipated 2 kW of power [25]. Its resistance was 11 Ω, while its self-inductance was 0.34 H. Because the magnet was designed for imaging extremities, it had a 24 cm diameter free bore and a 20 cm spherical homogeneous volume.

As mentioned in Section 3.1, the magnetic field created by the readout magnet must meet stringent stability requirements. In particular, the field must be temporally and spatially stable to ppm levels. The requirement for spatial stability (i.e., magnet homogeneity) is determined by the size of the imaging gradients. For instance, the readout-encoding gradient G needs to be much bigger than the variation in the readout field along the readout (i.e., x) direction:

$$G \gg \frac{\partial\,|B_r(\overrightarrow{r})|}{\partial x}. \tag{3.18}$$

For an imaging frequency of f_r=1 MHz, receiver bandwidth Δf=10 kHz and field-of-view FOV_x=10 cm, the per pixel bandwidth, dx, is 100 Hz/mm. To achieve less than 1 mm spatial distortion, the readout frequency must deviate by less than 100 Hz, or 100 ppm over the field-of-view.

Similarly, temporal stability of the readout magnet limits the variation in phase to less than π: $\Delta\phi < \pi$. Using the Nyguist theorem, $\Delta x = \pi/\gamma G T_{read}$, this requirement reduces to

$$\Delta B_r < G\Delta x. \tag{3.19}$$

For a 10 kHz receiver bandwidth, a 10 cm FOV_x, and a resolution in x, Δx, of 1 mm, the maximum variation in the readout frequency should be below 100 ppm. However, in addition to field drift, random noise causes phase noise (or field jitter), which can lower the SNR and can often dominate over all other constraints.

While the magnet homogeneity is achieved by a proper magnet design and by utilizing shimming gradients, the temporal stability is a harder condition to fulfill due to the resistive nature of the magnet. When the magnet heats up, the copper wire expands outwards thus changing the magnetic field in the center of the magnet bore and causing a drift in the resonance frequency of the system. When imaging water at 20% duty cycle, the readout frequency drifted 60-80 Hz. To minimize heating, the readout magnet is pulsed on at the end of the polarizing pulse and is pulsed off after the acquisition interval, even though in theory it could be left on during the polarizing phase. The heating of the system can be reduced partially by water-cooling the cooper wires (so called edge-cooling), which will be implemented in the next generation of magnets designed by the Stanford group. Another option, which is easy to implement on the current system, is to design a feedback system which would enable the RF transmitter (and receiver) to follow the frequency drift due to heating.

The pulsed readout magnet power supply is a current source capable of delivering up to 100 A of current. It was built from two *Techron 8607* MRI gradient amplifiers operating in a master-slave mode. The magnet current is sensed and controlled with a *Danfysik Ultrastab* current transducer. In addition, a series resistor-capacitor network in the feedback compensation was adjusted to achieve a critically-damped response to pulsed transients.

Figure 3.4: Photograph of the 13 cm bore, 0.4 T, 10 kW polarizing magnet used for polarizing protons in water in the PMRI experiments.

3.4.2 Polarizing Magnet and Power Supply

The PMRI polarizing magnet used for water experiments described in this work (Figure 3.4), was designed to produce a field strength of 0.4 T while drawing 100 A of current and dissipating 10 kW of power [25]. It weighed 42 kg, had a resistance of 1 Ω and a self-inductance of 65 mH. The diameter of the inner bore was fixed by the size of the object to be imaged, while the outer bore and length were two design variables. For wrist imaging, the inner bore was chosen to be 13 cm, so the magnet was designed to have an outer diameter of 22 cm and a length of 21 cm.

The polarizing magnet has to provide as strong a magnetic field as possible. The field strength is limited by power dissipation. For a magnet of resistance R, carrying a current I, the power P dissipated in the magnet is simply $P = I^2R$. Alternatively, the power can be expressed in terms of the energy U stored in the magnet, where $U = \frac{1}{2}LI^2$, and L is the inductance of the magnet: $P = \frac{2RU}{L}$. The energy stored in the magnet varies with the magnetic field, so that

$$U = \frac{1}{2\mu_\circ} \int_V |\mathbf{B_p}(\mathbf{r})|^2 \, dV, \tag{3.20}$$

where $|\mathbf{B_p}(\mathbf{r})|$ is the magnitude of the polarizing field at position $\mathbf{r}$, and V is the volume containing the field. Substituting Eq. 3.20 into the power equation, yields

$$P = \frac{R}{L}\frac{1}{\mu_\circ} \int_V |\mathbf{B_p}(\mathbf{r})|^2 \, dV. \tag{3.21}$$

Equation 3.21 tells us that the power dissipated in a magnet depends quadratically on the magnetic field amplitude, linearly on the volume of the magnetic field, and inversely on the magnet time constant L/R. Since the time constant varies with the magnet dimension, the power dissipated will also be a function of magnet size.

Unlike the readout magnet current source, the polarizing magnet current source does not need to supply a precisely regulated current, because the homogeneity requirement for the polarizing magnet is relaxed (see Section 3.1). However, since the current source needs to provide fast high power pulses, it is essential to use fast-switching electronics. The hardest condition to satisfy is the fast ramp-down of the magnetic field. To lose less than 20% of thermal magnetization, the 325 Joules of energy stored in the magnetic field need to be completely dissipated in less than 100 ms [64]. To achieve this, a power switching circuit was designed (Figure 3.5) which effectively transfers the coil energy to a capacitor [66]. When the switch in Figure 3.5 is enabled, current flows into the coil (inductor) and the magnet ramps up. When the switch is disabled, the circuit becomes effectively a parallel resonance RLC circuit. Normally, the energy would oscillate between the inductor and the capacitor with a time constant $T = 2\pi/\omega_\circ = 2\pi\sqrt{LC}$. However, the diodes in the circuit prevent reversal of the current, so the energy gets trapped in the capacitors.

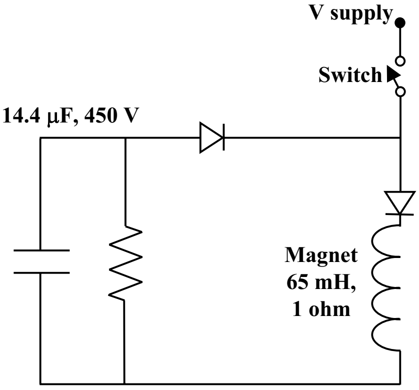

Figure 3.5: The pulsing/switching circuit. The circuit was used to transfer power stored in the conductor into the capacitor.

3.4.3 Transmit-Receive Circuit

PMRI uses low frequency signal detection, which is significantly more challenging than MR signal detection at high frequency. This is in part due to the fact that a higher readout frequency broadens the intrinsic coil bandwidth and in this way relaxes design constraints on the receiver components [24].

Consider a coil which is characterized by its quality factor Q. The Q-factor is equal to the ratio between the energy stored in the coil and the energy dissipated per unit cycle. The smaller the damping, the larger the Q-factor. A high Q coil has a long time response because the damping is small. In terms of the coil's inductance L_c and the series resistance R the Q-factor is

$$Q = \frac{\omega_\circ L_c}{R} \approx \frac{\omega_\circ}{|\Delta\omega|}, \tag{3.22}$$

where $\Delta\omega$ is the width of the resonance and the approximation is true if $\frac{\Delta\omega}{\omega_\circ} \ll 1$. The series resistance R is either equal to R_s when the sample is the dominant source of noise, or R_c when the coil is the dominant source of noise. Therefore, from the above equation it follows that

$$\begin{aligned} \Delta\omega &\propto \omega_\circ^2 \ \text{ when } R \approx R_s \\ \Delta\omega &\propto \omega_\circ^{1/2} \text{ when } R \approx R_c \,. \end{aligned} \tag{3.23}$$

Whether the dominant source of noise is the coil or the sample, the width of the resonance, and thus the bandwidth of the receiver, grows with MR frequency.[6]

The PMRI system uses a dual-mode transmit/receive coil. The transmit and receive modes differ by the function they perform in the MR circuitry. The transmit mode has to produce a high power (max 200 W) oscillating magnetic field in the direction perpendicular to the z-axis. This field causes the magnetization to tip away from the z-axis and, consequently, to precess like a spinning top around the readout field B_r. The transmit coil must have low Q (large $\Delta\omega$) so that it can recover quickly between subsequent RF pulses. To minimize distortion, the transmit coil's bandwidth has to be broader than the bandwidth of selective RF excitation pulses.

The receive mode of the RF circuitry has to detect and then amplify an *emf* signal on the order of a mV. Due to the small size of the detected signal, the receive coil must have a high Q for maximum SNR during acquisition and requires a low (typically 10 μW) power rating. In addition, the receive electronics must add minimum noise to the MR signal. To achieve this, an ultralow noise preamplifier is required. A tuned coil presents an impedance to the preamplifier that yields a low noise factor over 10 kHz bandwidth.

---

[6] This is valid only when resistance is in series with the inductor.

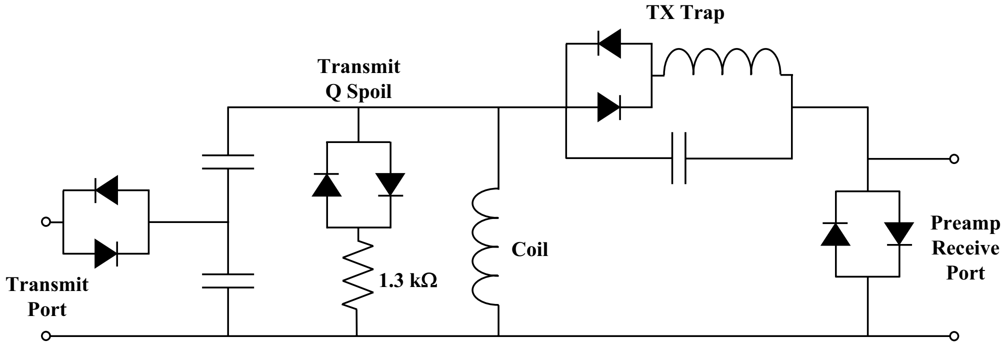

Figure 3.6: Dual transmit-receive circuit. The cross diodes present a short circuit in the transmit mode and an open circuit in the receive mode.

Figure 3.6 shows the schematics of the RF circuitry. The cross diodes can be regarded as switches that are *on* for voltages greater than 0.5 V, and *off* for other voltages. Since the transmitted signal is bigger than 0.5 V while the received signal is much smaller than 0.5 V, the diodes conduct in the transmit mode only, but present an open circuit in the receive mode. The pre-amplifier is thus protected from high voltages in the transmit mode. In addition, the coil's Q-factor is lowered during transmit mode by the presence of the 1.3 kΩ parallel resistor. For a resistor in parallel with the coil, the Q-factor is

$$Q = \frac{R}{\omega_\circ L} \, . \tag{3.24}$$

Contrary to Eq. 3.22, the Q-factor is now proportional to the total resistance. Since adding a resistor in parallel with the coil and sample resistances lowers the total resistance, the Q-factor is reduced.

Two type of coils were used in the prepolarized water and hyperpolarized gas experiments. A 9 cm diameter 4-turn litz wire saddle coil and a 3 cm diameter copper wire solenoid coil. Figure 3.7 shows the saddle coil, while Figure 3.8 shows the solenoid coil.

An RF slotted copper shield was added around the RF coils to shield them from the external magnetic fields which could degrade the coil's Q-factor. The shield slots, located where the coils RF image currents are zero, prevent gradient and polarizing coil eddy currents.

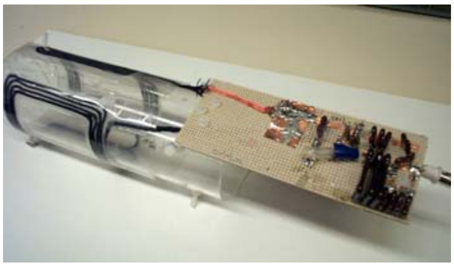

Figure 3.7: Saddle coil and the receiver-transmit circuitry used for hyperpolarized gas and water imaging at 1.1 MHz.

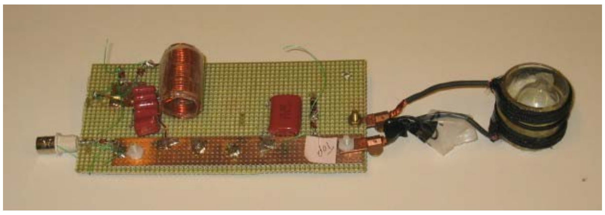

Figure 3.8: Solenoid coil and receiver-transmit circuitry used for hyperpolarized gas and water imaging at 397 kHz.

3.4.4 Gradients

The PMRI system, like the conventional MRI system, requires a 3-axis gradient coil to distinguish spin location in space. Due to the small bore required in PMRI imaging of the extremities, PMRI does not require high power gradient coils. The first gradient coil set was constructed using inexpensive cooper tape layered over an acrylic tube. The coils were 22.5 cm in diameter, 29 cm long, and at 10 A of current produced a gradient of 2.6 mT/m [25].

3.4.5 Techmag Console System - Data Acquisition and Control System

A commercial *Techmag Apollo* low-field imaging console was used in the experiments described in this work. *NTNMR* (version 1.3) software was used with the *Techmag* console. The software allowed the construction of various pulse sequences, such as gradient echo and spin echo sequences.

3.5 Hyperpolarized Gas Pumping Setup at Stanford

Figure 3.9: The pumping setup at Stanford.

The optical pumping setup at Stanford is displayed in Figure 3.9. The 1 inch cells were placed in the center of a 30 gauss field produced by a Helmholtz coil and heated by a heat gun to a temperature 120°C-150°C for ^{3}He and 80°C-90°C for ^{129}Xe. Optical pumping of Rb metal was achieved with approximately 7 W of circularly polarized laser light from a diode laser (15 W, *Optopower*, Tuscon, Arizona) that was tuned to the Rb D1 resonance (795 nm). The laser beam was first passed though a converging lens to prevent dispersion of the beam beyond the edges of the cell. It was then passed through a linear polarizer (i.e., beam-splitting cube) and through a quarter waveplate to produce circularly polarized laser light. Spin-exchange collisions between Rb electrons and the noble gas nuclei resulted in the hyperpolarization of the noble gas in the cell. The cell was then rapidly cooled in ice water to remove the Rb vapor by condensation onto the cell walls and so prevent depolarization of the hyperpolarized gas through collisions with unpolarized Rb atoms. Finally, the cell was carried into the low-field pulsed resistive scanner.

3.6 Concluding Remarks

Prepolarized MRI is a promising new MR technique which utilizes two variable electromagnets to produce low-field MR proton images, with SNR comparable to mid-field (0.5 T) scanners. The pulsed resistive low-field scanner has already produced high quality PMRI water images of human wrist anatomy [25].

In both, prepolarized MRI and hyperpolarized gas MRI, the amount of nuclear magnetization is independent of the readout field strength. There is thus no SNR advantage in increasing the readout field strength above the critical value at which the body becomes the dominant source of noise. The similarity of the prepolarized water and hyperpolarized gas SNR properties motivates the construction of a hybrid prepolarized water/hyperpolarized MR scanner [67].

In the next Chapter we are going to examine, among other things, whether the pulsed MR scanner is compatible with hyperpolarized gas imaging. In particular, we would like to know if the magnetic field is sufficiently stable for using spin echo based sequences, such as RARE, and whether the pulsing of the magnetic field destroys the hyperpolarized gas magnetization.

Chapter 4

T_2 Relaxation and Diffusion Measurements of Hyperpolarized ^{129}Xe and ^{3}He in the Pulsed Low-Field Resistive MR Scanner

4.1 Background

The transverse relaxation time T_2 characterizes the rate of magnetization decay in the plane perpendicular (or transverse) to the static magnetic field $B_\circ$ after the magnetization has been tipped away from the $B_\circ$ field by an RF pulse. The transverse magnetization decay results as spins lose their coherence while they precess with slightly different Larmor frequencies in the transverse plane. The dispersion in frequencies in turn occurs when the spins precess in different magnetic fields. There are three causes for this field variation [29]. First, the external field is not perfectly homogeneous and therefore varies slightly across the sample. Second, each spin creates a magnetic dipole field that affects the neighboring spins. This is commonly referred to as spin-spin interaction. Depending on the spin density distribution, the fields seen by the spins at different positions can be slightly different. Lastly, if spins move (diffuse) within the sample in the presence of background magnetic gradients[1], they experience a time varying field. The end result of the three scenarios is that some of the spins acquire extra phase, which leads to de-phasing and consequently, loss of MR signal.

In conventional MR, the transverse relaxation rate determines the amount of time available for imaging between each 90-degree RF excitation pulse. In spin echo imaging of water,

---

[1] The background gradients can either be due to field inhomogeneities or due to the externally applied gradients.

for instance, one acquires one or two lines of k-space [59] after each 90-degree RF excitation.[2] Therefore, the T_2 relaxation rate of water presents a limit on the time available for imaging one line of k-space. Once the transverse polarization of water is lost, the longitudinal thermal polarization is allowed to *grow* towards its thermal equilibrium value. A new 90-degree RF pulse flips the magnetization again into the transverse plane so that a new line of k-space is collected.

In contrast, the transverse relaxation rate of hyperpolarized gas determines the *total* time available for imaging in a spin echo sequence due to the nonrenewable nature of gas hyperpolarization. The longitudinal magnetization of hyperpolarized gas *decays* (rather than *grows*) with a time constant T_1 towards its thermal equilibrium. Hence, it does not pay off to wait after the transverse magnetization has decayed; the longitudinal magnetization will not recover to its initial hyper-value. To deal with the problem of nonrenewable polarization, small flip-angle pulse-sequences have primarily been used [6, 68]. However, such pulse sequences make poor use of the available magnetization as each acquisition only uses a small fraction ($\sin\alpha$, where α is the flip-angle) of the available magnetization. Since the inherent transverse relaxation times of gases[3] are an order of magnitude longer than for liquids [59], the entire k-space could be sampled using a single-shot (i.e, single 90-degree pulse) spin echo sequence. Such sequences should give a superior SNR compared to small flip-angle sequences because they use all the available magnetization ($\alpha = 90°$) to encode the image-domain data (see Section 4.6 for more details). In fact, imaging with the entire magnetization vector versus a 12-degree projection of the initial magnetization increases the SNR by a factor of around 5 ($\sin 90°/\sin 12° \approx 5$). This is equivalent to increasing the initial ^{129}Xe hyperpolarization from 5% to 25%–a goal that has proven to be very difficult to achieve.

Our aim was to implement a single-shot spin echo imaging sequence (also called CPMG sequence, after Carr-Purcell-Meiboom-Gill [69, 70], on the pulsed low-field resistive MR scanner. In particular, we wanted to investigate whether the resistive pulsed system was stable enough to maintain the stringent phase stability required during the CPMG condition. Studying T_2^{CPMG} relaxation enabled us to estimate the phase stability of the resistive scanner and to identify other potential problems of using the resistive system for spin echo

---

[2] K-space (or time-domain space) is the Fourier transform of image-domain space.

[3] The inherent transverse relaxation times should be understood as the transverse relaxation times resulting exclusively from spin-spin interactions.

imaging.

Furthermore, by varying the interecho spacing in the CPMG spin echo sequence, we were able to differentiate between the T_2^{CPMG} relaxation times and the inherent T_2 relaxation of gases. The T_2^{CPMG} relaxation characterizes the decay of a spin echo train in a particular magnetic environment and thus includes diffusion losses in the background gradients, while the inherent T_2 relaxation times of gases are purely the property of the gas mixture used. The inherent T_2 times of ^{129}Xe and ^{3}He mixtures used in the hyperpolarized gas experiments are a useful measure of the absolute limit on the imaging time when using a CPMG sequence. To the best of our knowledge, past experiments measuring the transverse relaxation times of ^{129}Xe and ^{3}He [47, 71, 72, 26, 73, 28, 74, 75, 76, 77] did not remove the effects of diffusion losses in the static background (remnant) gradients. The values of T_2 relaxation times quoted in the literature are thus comparable to what we call T_2^{CPMG} relaxation, and not to the inherent T_2 relaxation.

Apart from the non-renewable nature of the noble gas polarization, large diffusion of gases is another factor that makes imaging of hyperpolarized gas difficult, and more importantly, dictates pulse-sequence design. Diffusion of spins through magnetic field gradients causes loss of NMR signal and limits the maximum achievable resolution. The reduced susceptibility effect and smaller magnetic field heterogeneities at low fields should help decrease signal loss due to diffusion in our low-field system. However, in order to predict MR signal loss during imaging with spin echo and/or gradient echo sequences, we had to evaluate the diffusion coefficient of hyperpolarized gases on our system. Diffusion coefficients for ^{129}Xe and ^{3}He *in vitro* have been measured. Patyal *et al.* [78] performed measurements of ^{129}Xe diffusion coefficient while Bock *et al.* [79] and Schmidt *et al.* [80] measured diffusion coefficient of ^{3}He. However, all these measurements were done using low flip-angle techniques (gradient echo, DANTE) which suffer from poor SNR and are limited by T_1 relaxation. Some fast sequences, such as BURST from Wolber *et al.* [81] and Peled *et al.* [82] avoided the problem of T_1 relaxation, but had a complicated spin dynamics. Mair *et al.* [83] and Zhao *et al.* [77] established the advantage of high SNR techniques based on multiple spin echo sequences (RARE, CPMG). These techniques enable the use of multiple diffusive attenuations within a single sequence and thus allow the measurement of time-dependant (or restricted) gas diffusion [83]. However, to remove diffusion losses in the background gradients from the total signal decay, the experiments in [83] and [77] required two shots (i.e., two separate CPMG trains) as well as the normalization of the echo train against the first echo. Two (or multi) shot spin echo sequences are impractical in the case of hyperpolarized gases because of the non-renewable gas polarization.

Our single-shot CPMG sequence for measuring diffusion coefficient uses all the available magnetization and thus has inherently high SNR. In addition, the chosen sequence enabled us to separate T_2^{CPMG} relaxation of the gas from diffusive loses in the external gradients. Finally, by comparing the experimental measurement of ^{3}He, ^{129}Xe and water diffusion coefficients with theoretical estimations, we were able to determine the precision of our single-shot CPMG sequence for measuring diffusion coefficients.

4.2 Theory of Transverse (T2) Relaxation

As mentioned in Section 4.1, the transverse component of magnetization decays due to magnetic fluctuations which cause spreading in the Larmor frequency of the spin ensemble and, consequently, dephasing. The rate of decay of the transverse component M_{xy} is proportional to the instantaneous value of the transverse magnetization,

$$\frac{dM_{xy}}{dt} = -\frac{M_{xy}}{T_2^*}, \tag{4.1}$$

where the transverse relaxation coefficient T_2^* includes the relaxation due to static magnetic field inhomogeneities, $T_{\Delta B_z}$, the inherent relaxation due to spin-spin interactions, T_2, and relaxation due to the diffusion of spins in the magnetic field gradients, T_D.[4] To summarize:

$$\frac{1}{T_2^*} = \frac{1}{T_{\Delta B_z}} + \frac{1}{T_2} + \frac{1}{T_D}. \tag{4.2}$$

Later in the chapter we will show how to separate the $1/T_{\Delta B_z}$ term from the rest of relaxation using spin echoes. Once that is accomplished, we proceed to identify the $1/T_D$ term and distinguish it from the inherent $1/T_2$ relaxation of hyperpolarized gases (^{129}Xe ad ^{3}He).

The solution to Eq. 4.1, after a 90-degree excitation ($M_{xy}(0) = M_\circ$), is

$$M_{xy} = M_\circ e^{-t/T_2^*}. \tag{4.3}$$

Equation 4.3 describes the macroscopic behavior of the transverse component of the magnetization. However, to understand how the above relationship arises as a result of the microscopic motion of magnetic moments, one has to consider the equations of motion of the individual spins and then average over the spin population.

The magnetic field seen by the jth spin is $\mathbf{B}_j = (B_\circ + b_j)\mathbf{k}$, where $B_\circ\mathbf{k}$ is the static magnetic field pointing in the z-direction and $b_j\mathbf{k}$ is the z component of the field fluctuations seen by the jth spin.[5] For mobile (i.e., diffusing) spins, b_j is time-varying. The equation of

---

[4] It should be pointed out that most books on the subject of MR relaxation define Eq. 4.1 in terms of T_2 and not T_2^* as is done here.

[5] This discussion assumes that only those fluctuations in b_j that are parallel to $B_\circ$ cause variations in Larmor frequency and therefore transverse relaxation. This approximation is invalid when dealing with longitudinal relaxation or non-adiabatic transverse relaxation.

motion for the jth magnetic moment is

$$\dot{\boldsymbol{\mu}}_j = \gamma \boldsymbol{\mu}_j \times \mathbf{B}_j = \gamma \boldsymbol{\mu}_j \times [B_\circ + b_j(t)]\mathbf{k}. \tag{4.4}$$

Combining the x and y transverse components of the magnetic moment into a single complex μ, such that $\mu_j = \mu_{j,x} + \mu_{j,y}$, the equations of motion become

$$\dot{\mu}_j(t) = -i\gamma[B_\circ + b_j(t)]\mu_j(t). \tag{4.5}$$

After integration, the above equation gives

$$\mu_j(t) = \exp\left(-i\gamma B_\circ t\right) \exp\left[-i\gamma \int_0^t b_j(\tau)d\tau\right]\mu_j(0), \tag{4.6}$$

where $\mu_j(0)$ is the initial magnetization of the jth spin. To get the total transverse magnetization, we have to sum over N particles in the system:

$$\begin{aligned} \mathbf{M} &= \frac{1}{V}\sum_{j=1}^{N} \boldsymbol{\mu}_j & (4.7) \\ &= \frac{1}{V}\sum_{j=1}^{N} \exp\left[-i\gamma B_\circ t - i\gamma \int_0^t b_j(\tau)d\tau\right]\mu_j(0). & (4.8) \end{aligned}$$

Since the initial value of the magnetic moment $\mu_j(0)$ is independent of its local field b_j the initial magnetization can be factored out:

$$M(0) = \frac{1}{V}\sum_{j=1}^{N} \mu_j(0). \tag{4.9}$$

By also factoring out the exponential representing the precession around $B_\circ$ field, the complex transverse magnetization is finally given by

$$M(t) = \exp\left(-i\gamma B_\circ t\right) \left\{ \frac{1}{N}\sum_{j=1}^{N} \exp\left[-i\gamma \int_0^t b_j(\tau)d\tau\right] \right\} M(0). \tag{4.10}$$

Equation 4.10 describes the behavior of the transverse magnetization, also called the Free-Induction-Decay (FID). The first term represents the oscillatory part of the FID–the oscillation of magnetization around $B_\circ$, with the characteristic Larmor frequency $\omega_\circ = \gamma B_\circ$, where γ is the gyromagnetic ratio of the spin. The last term is the initial value of magnetization. The term in the curly brackets is the envelope of the FID–the relaxation of the transverse magnetization.

Let us look more closely at the relaxation part of the FID. The time integral over the magnetic fluctuations seen by the jth particle in Eq. 4.10 can be related to the accumulated phase angle $\phi_j(t)$, where

$$\phi_j(t) = -\gamma \int_0^t b(\tau) d\tau. \tag{4.11}$$

The average over the population of particles can then be written as

$$\begin{aligned} F(t) &= \frac{1}{N} \sum_{j=1}^{N} \exp\left[-i\phi(t)\right] = \langle \exp\left[-i\phi(t)\right] \rangle && (4.12) \\ F(t) &= \int P[\phi(t)] \exp\left[i\phi(t)\right] d\phi, && (4.13) \end{aligned}$$

where $P[\phi(t)]d\phi$ is the probability that a spin had accumulated a phase between ϕ and $\phi + d\phi$ in a time t. To solve Eq. 4.13, we have to assume a functional form for the probability function. Since the spin samples many different fields over a short time, we can invoke the Central Limit Theorem [29]. The probability distribution of phase angles can thus be described using a Gaussian function, with zero mean angle and a mean square width of $\langle \phi^2 \rangle$:

$$P(\phi) = \frac{1}{(2\pi\langle\phi^2\rangle)^{\frac{1}{2}}} \exp\left(-\frac{\phi^2}{2\langle\phi^2\rangle}\right). \tag{4.14}$$

The relaxation of the FID signal, using a Gaussian distribution for the spin phase angles, is

$$F(t) = \frac{1}{(2\pi\langle\phi^2\rangle)^{\frac{1}{2}}} \int_{-\infty}^{\infty} \exp\left(-\frac{\phi^2}{2\langle\phi^2\rangle}\right) \exp\left(i\phi\right) d\phi. \tag{4.15}$$

The integral above can be evaluated by completing the square of the arguments of the exponentials. The result is

$$F(t) = \exp\left[-\frac{\langle\phi^2(t)\rangle}{2}\right] \equiv \exp\left[-\frac{t}{T_2^*}\right]. \tag{4.16}$$

To make further progress on the equation above would require us to know the mean square width of the phase angles sampled by the spins. Nevertheless, by starting with the equation of motion for the individual spins (Eq. 4.4) and then averaging over the spin population, we were able to show that the transverse magnetization can be expressed as

$$M(t) = M(0) \exp{(-i\omega_{\circ} t)} F(t), \tag{4.17}$$

where F(t) is given by Eq. 4.16. We will return to this equation as well as Eq. 4.10 in the following chapters when describing the effects of magnetic field inhomogeneities and the effect of diffusion on transverse relaxation.

4.3 Reversible T2 Decay

Equation 4.2 tells us that part of the transverse relaxation is due to the inhomogeneities in the main magnetic field. Spins at different positions in the sample dephase because they see a different field. Fortunately, the magnetization lost due to dephasing in an inhomogeneous magnet can be recovered using the technique of spin echoes.

4.3.1 Magnet Inhomogeneities and Spin Echoes

The easiest way to understand the occurrence of a spin echo is to draw on the analogy between the spins precessing in an inhomogeneous magnetic field and runners running with different speeds on a track course. Imagine the runners started running at the same time and place on the track. After some time t into the run, the runners will be spread along the course of the run, with the fastest runner furthest away from the start and the slowest one the closest. If at time t, the runners are made to turn back (i.e., reverse direction of running by 180°) and if they continue to run at the same speed, they will all reach the start at the same time, namely, at time $2t$. The distance by which the fastest runner was ahead of the slowest one before time t, he gets behind after time t; what used to be an advantage turned into a disadvantage. Similarly, the spins in a higher magnetic field precess faster than the spins in the lower magnetic field. After a time t, the fast spins will have gained an additional $\Delta\phi$ of phase relative to the slow spins. If the sense of spin precession is reversed at time t (with a 180-degree pulse), then the spins will again have the same phase at time $2t$. In other words, the coherence of spins will be fully restored at time $2t$.

To demonstrate the concept of spin echoes formally, we return to Eq. 4.10, representing the behavior of transverse magnetization at time t, where $b_j(t)$ is the magnetic field variation seen by the jth particle. It is best to transform this equation to the rotating frame of reference. In the rotating frame, the Larmor precession is not detectable. Thus,

$$M(t) = \frac{1}{N}\sum_{j=1}^{N} \exp\left[-i\gamma \int_0^t b_j(\tau)d\tau\right] M(0). \tag{4.18}$$

If a π pulse is applied at time t about an axis in the transverse plane, all spins will be rotated through a 180-degree angle and the net complex magnetization vector M will

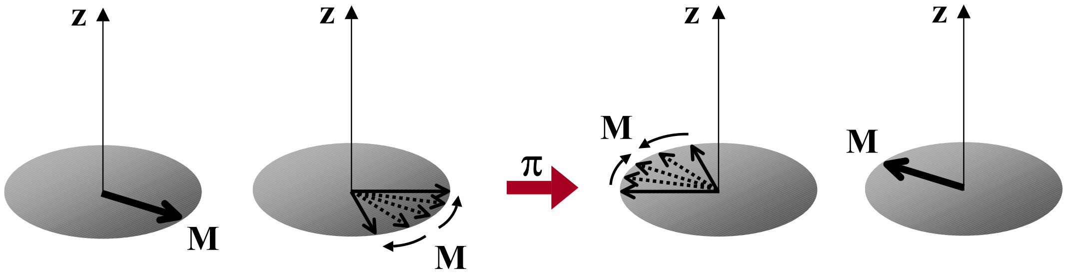

Figure 4.1: Creation of a spin echo.

be transformed into its complex conjugate M^* (Figure 4.1).[6] Therefore, after a 180-degree rotation, the transverse magnetization vector at time t will be

$$M(t) = \frac{1}{N}\sum_{j=1}^{N} \exp\left[+i\gamma \int_0^t b_j(\tau)d\tau\right] M^*(0). \tag{4.19}$$

If the spins continue to precess in the same sense they did before the application of the π pulse (in the runners' case, this would correspond to saying that the runners continue to run *forward* after they have turned around at time t), then, after an additional time t_1, they will acquire an extra phase, $\exp\left(-i\gamma \int_t^{t+t_1} b_j(\tau)d\tau\right)$, and the complex transverse magnetization in the rotating frame will be

$$M(t+t_1) = \frac{1}{N}\sum_{j=1}^{N} \exp\left[-i\gamma \int_t^{t+t_1} b_j(\tau)d\tau\right] \exp\left[+i\gamma \int_0^t b_j(\tau)d\tau\right] M^*(0). \tag{4.20}$$

For diffusing spins, the integrals over the field from 0 to t and from t to $t+t_1$ will not cancel out because spins diffuse randomly in the magnetic field. However, for stationary[7] spins, the integrals reduce to $\exp(-i\gamma b_j t_1)$ and $\exp(+i\gamma b_j t)$. Then,

$$M(t+t_1) = \frac{1}{N}\sum_{j=1}^{N} \exp\left[-i\gamma b_j(t_1 - t)\right] M^*(0). \tag{4.21}$$

---

[6] This can most easily be seen by fixing the axis of rotation and looking at the transformation of magnetization components under the 180-degree rotation. If the magnetization is rotated by 180° around the x-axis, for instance, then: $M_x \to M_x, M_y \to -M_y, M_z \to -M_z$. From this transformation we see that the complex transverse magnetization $(M_x + iM_y)$ transforms into its conjugate $(M_x - iM_y)$ under a 180-degree rotation around x, similarly for a 180-degree rotation around y-axis.

[7] Stationary spins are spins that do not move out of a voxel of size $(\Delta a)^3$, where Δa is the resolution of MR imaging system.

If $t = t_1$, then $M(2t) = M^*(0)$. This means that for stationary spins, the initial magnetization has been fully recovered at time $2t$. For diffusing spins, however, the echoes will still occur, but with progressively smaller amplitudes. The decay of the echoes due to diffusion will be examined in the next chapter.

In addition to signal loss due to diffusion of spins, the 180-degree pulses in the echo sequence do not refocus the effects of spin-spin interaction. To see this, we return to Eq. 4.18. For spin-spin interaction (see Section 4.4.2), the source of magnetic field b_j are the magnetic dipoles rather than the external field. By rotating the magnetization 180°, the magnetic dipoles and, therefore, the sources of the field inhomogeneity, are rotated as well. This means that in addition to converting the magnetization in Eq. 4.18 into its conjugate, the sign of b_j needs to be inverted. Consequently, the two exponentials do not cancel out–and the magnetization which was lost through the local fields of dipolar origin cannot be recovered [29].

Using the technique of spin echoes one can thus distinguish between the relaxation due to instrumentational limitations (i.e., inhomogeneous holding magnetic field) and relaxation inherent to the system (i.e., spin-spin interaction and diffusion). In other words, the $1/T_{\Delta B_z}$ term can be factored out of Eq. 4.2, so that

$$\frac{1}{T_2^*} = \frac{1}{T_{\Delta B_z}} + \frac{1}{T_2^{CPMG}}, \tag{4.22}$$

where the T_2^{CPMG} time constant describes the rate of spin echo decay resulting from the inherent T_2 relaxation and diffusion losses[8],

$$\frac{1}{T_2^{CPMG}} = \frac{1}{T_2} + \frac{1}{T_D}. \tag{4.23}$$

---

[8] CPMG stands for Carr-Purcell-Meiboom-Gill [69, 70].

4.4 Irreversible T2 Decay

The T2 relaxation which occurs due to magnetic field inhomogeneities can be removed using spin echo techniques. We call such relaxation a *reversible* T_2 decay. The spin-spin interactions and diffusion, on the other hand, contribute to an *irreversible* T2 decay, which will be examined in detail in this section.

4.4.1 Diffusion

We present two alternative approaches in deriving an expression for signal decay due to diffusion of spins in the field gradients. The first approach is statistical, based on the random walk of spins [59]. This approach illustrates the statistical nature of spins, but is cumbersome and limited to the case of constant gradients. The second approach is based on the generalized Bloch equation, which has two extra terms as compared to the standard Bloch equation–a term describing the transport of magnetization due to flow and a term describing the random transport of magnetization due to diffusion [59]. This approach is less intuitive, but has the advantage of being elegant and applicable to an arbitrary gradient form.

4.4.1.1 Statistical Approach to Signal Decay due to Diffusion in Constant Gradients

The goal is to find the average square phase shift $\overline{\Delta\theta^2}$ (Eq. 4.16) for spins diffusing randomly through a constant gradient. If the motion is limited to one dimension, then the frequency of precession of such spins is $\omega(t) = \gamma B_\circ + \gamma G x$, where x is the average distance that a particle travels in time t. If time t is divided into n steps, each of duration τ_s, then $t = n\tau_s$. During each step, the particle jumps either left or right with equal probability, so that $a_i = \pm 1$. If the root-mean-square (r.m.s.) displacement in one dimension is ξ, then the distance z travelled by the molecule after n jumps is

$$z(n\tau_s) = \sum_{i=1}^{n} \xi a_i, \tag{4.24}$$

$$\overline{z^2(n\tau_s)} = \sum_{i=1}^{n}\sum_{j=1}^{n} \xi^2 a_i a_j = \sum_{i=1}^{n}\sum_{j=1}^{n} \xi^2 \delta_{ij} = \sum_{i=1}^{n} \xi^2 = n\xi^2. \tag{4.25}$$

Defining the diffusion constant as

$$D = \frac{\xi^2}{2\tau_s}, \tag{4.26}$$

we get

$$\overline{z^2(t)} = 2tD. \tag{4.27}$$

The above equation relates the macroscopic mean square displacement of a diffusing particle $\overline{z^2}$ and the diffusion constant D. For three-dimensional molecular motion, the factor 2 in Eq. 4.27 should be replaced by 6.

Let us go back to the equation describing the frequency of precession. Replacing x with $z(n\tau_s)$, we have

$$\omega(n\tau_s) = \gamma B_\circ + \gamma G \sum_{i=1}^{n} \xi a_i. \tag{4.28}$$

The cumulative angle after time $t = n\tau_s$ is

$$\phi(t) = \gamma B_\circ n\tau_s + \sum_{m=1}^{n} \gamma G\tau_s \sum_{i=1}^{m} \xi a_i = \phi_\circ + \Delta\phi. \tag{4.29}$$

Note that $\sum_{m=1}^{n} \gamma G\tau_s \sum_{i=1}^{m} \xi a_i = \sum_{i=1}^{n}(n+1-i)\xi a_i \gamma G\tau_s$. Therefore,

$$\begin{aligned}
\overline{\Delta\phi^2(n\tau_s)} &= \gamma^2 G^2 \tau_s^2 \xi^2 \sum_{i=1}^{n}\sum_{j=1}^{n}(n+1-i)(n+1-j)a_i a_j \\
&= \gamma^2 G^2 \tau_s^2 \xi^2 \sum_{i=1}^{n}\sum_{j=1}^{n}(n+1-i)(n+1-j)\delta_{ij} \\
&= \gamma^2 G^2 \tau_s^2 \xi^2 \sum_{i=1}^{n}(n+1-i)^2 = \gamma^2 G^2 \tau_s^2 \xi^2 \sum_{j=1}^{n} j^2 \\
&= \frac{1}{3}\gamma^2 G^2 \tau_s^2 \xi^2 n^3 \\
&= \frac{2}{3}\gamma^2 G^2 D \tau_s^3 n^3 \\
\overline{\Delta\phi^2(t)} &= \frac{2}{3}\gamma^2 G^2 D t^3,
\end{aligned} \tag{4.30}$$

where on line 3 of the above equation we used the equality $\sum_{i=1}^{n}(n+1-i)^2 = \sum_{j=1}^{n} j^2$.

If the average square phase shift is inserted into Eq. 4.16, we obtain an expression for the relaxation of the FID signal which results exclusively from the diffusion of spins in a constant gradient:

$$F(t) = \exp\left(-\frac{1}{3}\gamma^2 G^2 D t^3\right). \tag{4.31}$$

If a 180-degree RF pulse reverses the orientation of spins in the magnetic field gradients at time t, the spins begin to re-phase, until they are fully re-phased and an echo is formed at time $2t$ (see Section 4.3.1). The re-phasing of spins decreases the net effect of diffusion losses. In other words, if spins were allowed to diffuse in a positive (constant) gradient for a time $2t$, the diffusion losses would be proportional to $\exp\left[-\frac{1}{3}\gamma^2 G^2 D(2t)^3\right]$. However, since the π pulse reverses the sign of the magnetic field gradients seen by the spins at time t, the echo magnitude at time $2t$ will be

$$\begin{aligned} M(2t) &= M(t)\exp\left(-\frac{1}{3}\gamma^2 G^2 D t^3\right) \\ M(2t) &= \left[M(0)\exp\left(-\frac{1}{3}\gamma^2 G^2 D t^3\right)\right]\exp\left(-\frac{1}{3}\gamma^2 G^2 D t^3\right) \\ M(2t) &= M(0)\exp\left(-\frac{1}{12}\gamma^2 G^2 D\,(2t)^3\right). \end{aligned} \tag{4.32}$$

The spin echo at time $T = 2t$ can then be expressed as

$$M(T) = M(0)\exp\left(-\frac{1}{12}\gamma^2 G^2 D\,(T)^3\right). \tag{4.33}$$

4.4.1.2 Signal Decay due to Diffusion in an Arbitrary Gradient Waveform Based on the Bloch Equation

The generalized Bloch equation for the M_x-coordinate is

$$\frac{dM_x}{dt} = \gamma M_y B_{eff} - \frac{M_x}{T_2} + \nabla \cdot \vec{D} \cdot \nabla M_x - \nabla \cdot \vec{v} M_x. \tag{4.34}$$

The first term on the right hand side is due to the rotation of the magnetization around the effective field $B_{eff} = \left(B_\circ - \frac{\omega}{\gamma}\right) + \mathbf{r}\cdot\mathbf{g}$, where $\mathbf{g} = \partial B_z/\partial x\,\hat{\mathbf{dx}} + \partial B_z/\partial y\,\hat{\mathbf{dy}} + \partial B_z/\partial z\,\hat{\mathbf{dz}}$ is the magnetic field gradient and $\mathbf{r} = \mathbf{x} + \mathbf{y} + \mathbf{z}$ is the position of the spin with respect to an arbitrary origin; the second term represents the inherent T_2 relaxation; the third term stands for relaxation due to diffusion of spins in the magnetic field gradients; the fourth and last term represents relaxation due to the directional transport (i.e., flow) of magnetization.[9] By exchanging the subscript x in Eq. 4.34 with y and vice versa, one can obtain a similar

---

[9] We choose to include the 'flow' term in the Bloch equation to illustrate the most general situation. Our *in vitro* experiments did not include flow; however, when modelling an *in vivo* situation, such as delivery of hyperpolarized gas to the lungs through inhalation, the relaxation due to the flow of magnetization should be taken into account.

equation for the M_y magnetization component:

$$\frac{dM_y}{dt} = -\gamma M_x B_{eff} - \frac{M_y}{T_2} + \nabla \cdot \vec{D} \cdot \nabla M_y - \nabla \cdot \vec{v} M_y. \tag{4.35}$$

We can combine Eqs. 4.34 and 4.35 by introducing a complex magnetization $M_+ = M_x + iM_y$. Furthermore, on resonance, $\omega = \gamma B_\circ$, and the effective field reduces to $B_{eff} = \mathbf{r} \cdot \mathbf{g}$. Thus,

$$\frac{\partial M_+}{\partial t} = -i\gamma \mathbf{r} \cdot \mathbf{g} M_+ - \frac{M_+}{T_2} + \nabla \cdot \vec{D} \cdot \nabla M_+ - \nabla \cdot \vec{v} M_+. \tag{4.36}$$

For isotropic diffusion, the diffusion term in the Bloch equation reduces to

$$\nabla \cdot \mathbf{D} \cdot \nabla M_+ = \nabla \cdot \begin{pmatrix} D & 0 & 0 \\ 0 & D & 0 \\ 0 & 0 & D \end{pmatrix} \cdot \nabla M_+ = D\nabla^2 M_+. \tag{4.37}$$

In addition, for spatially independent velocities, the flow term in the Bloch equation becomes

$$\nabla \cdot \vec{v} M_+ = (\nabla \cdot \vec{v}) M_+ + \vec{v} \cdot \nabla M_+ = \vec{v} \cdot \nabla M_+. \tag{4.38}$$

Assuming a solution of the form

$$M_+(\mathbf{r}, t) = A(t) \exp\left[-i\gamma \mathbf{r} \cdot \int_0^t \mathbf{g}(\tau) d\tau\right] \exp\left[-\frac{t}{T_2}\right], \tag{4.39}$$

and substituting it into Eq. 4.36, we get an expression for $A(t)$:

$$A(t) = \exp\left[-D\gamma^2 \int_0^t \left(\int_0^{t'} \mathbf{g}(\tau) d\tau\right)^2 dt'\right] \exp\left[i\gamma \mathbf{v} \cdot \int_0^t \left(\int_0^{t'} \mathbf{g}(\tau) d\tau\right) dt'\right]. \tag{4.40}$$

The first exponential on the right side of the above equation represents the signal decay due to diffusion, while the second exponential represents the signal decay due to flow. We will focus on the first term only. Since $k \equiv \frac{\gamma}{2\pi} \int_0^{t'} \mathbf{g}(\tau) d\tau$ [59], we can express the diffusion term as

$$\exp\left[-\frac{t}{T_D}\right] = \exp\left[-4\pi^2 D \int_0^t \mathbf{k}^2(t') dt'\right] = \exp\left[-Db\right], \tag{4.41}$$

where

$$b \equiv 4\pi^2 \int_0^t \mathbf{k}^2(\tau) d\tau. \tag{4.42}$$

Equation 4.41 tells us that by knowing the diffusion constant of the gas mixture and the integral of the gradient waveform over time, one can find T_D and as a result eliminate the signal decay due to diffusion from the total decay (see Eq. 4.2).

4.4.2 Spin-Spin Interaction

The theory of spin-spin interaction is very complex and can only be explained using the quantum mechanical description of nuclear interactions. We therefore limit this section to outlining the main steps in the derivation of T_2 as described in [59] .

There are several processes which contribute to dephasing of transverse magnetization [59]: the dipolar interaction between a pair of spins, chemical shift interaction, scalar coupling, and the quadrupole interaction (for $I > 1/2$). For spin-1/2 nuclei, the dominant interaction causing spin relaxation arises from the dipolar Hamiltonian [59], which is

$$H_D = \frac{\mu_\circ}{4\pi} \sum_{i<j} \frac{\gamma_i \gamma_j \hbar}{r_{ij}^3} \left[\mathbf{I}_i \cdot \mathbf{I}_j - \frac{3(\mathbf{I}_i \cdot \mathbf{r}_{ij})(\mathbf{I}_j \cdot \mathbf{r}_{ij})}{r_{ij}^2} \right], \tag{4.43}$$

where the sum refers to all the spin pairs (i,j), $\mathbf{I}$ is the vector operator given by $I_x\mathbf{x}+I_y\mathbf{y}+I_z\mathbf{z}$, and r_{ij} is the distance between two spins.

If we introduce a density matrix ρ, where for a spin-1/2 particle the density matrix is

$$\rho = \begin{bmatrix} \frac{1}{2} + \overline{\langle I_z \rangle} & \overline{\langle I_x - iI_y \rangle} \\ \overline{\langle I_x + iI_y \rangle} & \frac{1}{2} - \overline{\langle I_z \rangle} \end{bmatrix}, \tag{4.44}$$

then the evolution of the density matrix in the rotating frame of reference can be expressed as

$$i\frac{d\rho^*(t)}{dt} = \left[H_D^*(t),\, \rho^*(t) \right], \tag{4.45}$$

where H_D^* is the transformed dipolar Hamiltonian, $\exp\left[i\omega_\circ I_z t\right] H_D(t) \exp\left[-i\omega_\circ I_z t\right]$, $\rho^*(t)$ is transformed density matrix, $\exp\left[i\omega_\circ I_z t\right]\rho(0)\exp\left[-i\omega_\circ I_z t\right]$, and $\omega_\circ$ is the Larmor frequency.

Once the evolution of ρ^* in Eq. 4.45 is calculated, the decay of transverse relaxation can be determined. From [59], the transverse relaxation time in liquids T_2 is

$$\frac{1}{T_2} = \left(\frac{\mu_\circ}{4\pi}\right)^2 \gamma^4\,\hbar^2\,\frac{3}{2}\,I(I+1)\left[\frac{1}{4}J^{(0)}(0) + \frac{5}{2}J^{(1)}(\omega_\circ) + \frac{1}{4}J^{(2)}(2\omega_\circ)\right], \tag{4.46}$$

where $J^{(0)}(0)$, $J^{(1)}(\omega)$ and $J^{(2)}(\omega)$ are spectral density functions defined in terms of the rotational correlation time τ_c as

$$\begin{aligned} J^{(0)}(0) &= \frac{24}{15r_{ij}^6}\,\tau_c \\ J^{(1)}(\omega) &= \frac{4}{15r_{ij}^6}\,\frac{\tau_c}{1+\omega^2\tau_c^2} \\ J^{(2)}(\omega) &= \frac{16}{15r_{ij}^6}\,\frac{\tau_c}{1+\omega^2\tau_c^2}. \end{aligned} \tag{4.47}$$

4.5 Measurements of Reversible Transverse Relaxation with Free-Induction-Decay

The largest contribution to T_2^* relaxation is dephasing due to external field inhomogeneities (see Eq. 4.2), which can be removed using the technique of spin echoes. Consequently, T_2^* does not give any information about the system under study (hyperpolarized gas, for instance); it only describes how well one is able to *shim* the external magnet. To minimize the external field inhomogeneities, FID signals (which decay with time constant T_2^*, see Eq. 4.16) were collected prior to any other signal acquisition. Shimming currents were applied to the x, y, and z gradient coils in order to maximize T_2^* relaxation time. From the frequency domain perspective (see Appendix B), this translated into minimizing the linewidth of the frequency spectrum.

In addition to shimming, the FID signal was used to match the receiver frequency to the frequency of transmission (and therefore, precession). Special care was devoted to being within a few Hertz of the precession frequency to avoid off-resonance effects.

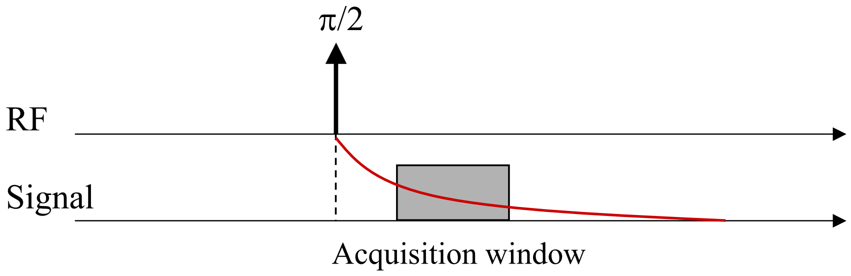

Figure 4.2: Pulse sequence used to generate free-induction-decay, or FID.

Figure 4.2 shows the basic structure of the pulse sequence used to generate free-induction-decay. The duration of the RF pulse determines the angle by which the magnetization has been tipped away from the static field (so-called “flip-angle”). If the amplitude of the RF field is B_1 and the frequency of precession around the B_1 field is $\omega_1 = d\theta/dt$, then the flip-angle $d\theta$ is

$$d\theta = \gamma B_1 dt. \tag{4.48}$$

Normally, the flip-angle is chosen to be 90° (i.e., $\pi/2$) to maximize the projection of magnetization onto the transverse plane and, therefore, the SNR.

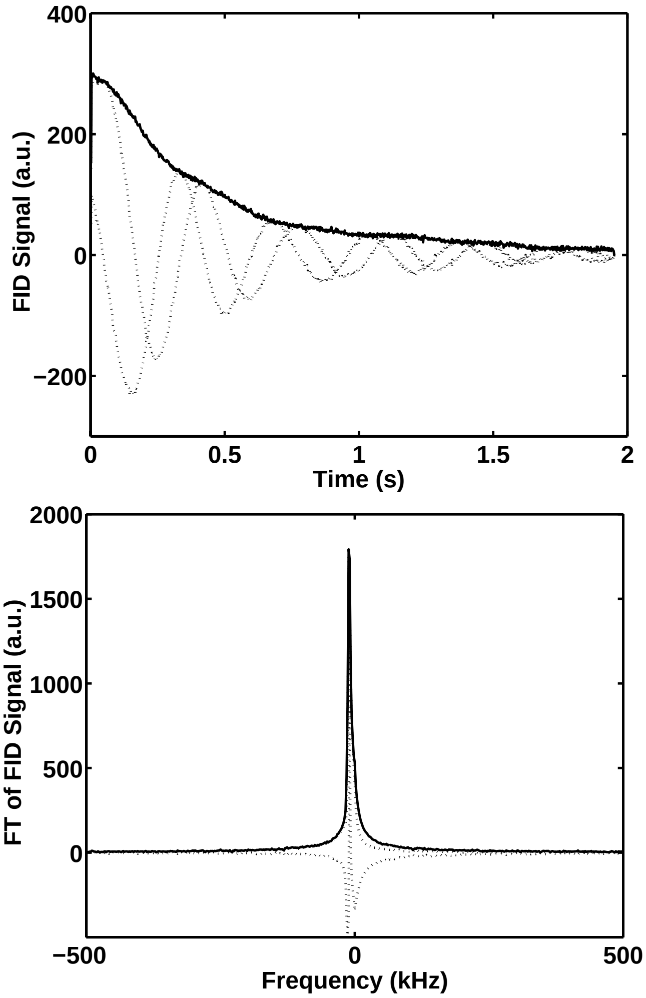

Figure 4.3: Free-induction-decay (FID) signal of water taken on the low-field pulsed resistive scanner (top) and its Fourier transform (bottom).

Figure 4.3 shows a typical FID signal of distilled water and its spectra, which is obtained by taking the Fourier transform (FT) of the time domain signal. Since the FT of an exponential decay is a Lorentzian (see Appendix B), we can fit the data to the function of the form

$$L(x) = \frac{1}{\pi} \frac{\frac{1}{2}\Gamma}{(\omega - \omega_\circ)^2 + \left(\frac{1}{2}\Gamma\right)^2} \,, \tag{4.49}$$

where Γ is the FWHM (Full-Width-Half-Maximum) value and $\omega_\circ$ is the central frequency of the fit. From Appendix B, the T_2^* relaxation time is

$$T_2^* = \frac{1}{\pi\Gamma}. \tag{4.50}$$

The typical linewidth (FWHM) of water, ^{129}Xe and ^{3}He frequency spectra at 397 kHz central frequency was between 5 and 15 Hz. The T_2^* relaxation rate for all samples was thus between 20 ms and 60 ms. Since the FID was collected from the entire sample (i.e., a sphere of diameter Δx, where $\Delta x = 2.5$ cm), the typical background gradients due to the field inhomogeneities were $G = \Delta f/(\gamma \Delta x) = 0.01 - 0.03$ mT/m.

4.5.1 Determination of Gas Polarization

Water and gas spectra were also used for calibrating the noble gas polarization. As demonstrated in Eq. 3.4, the NMR signal is proportional to the magnetization of the sample and the frequency ω at which the signal was acquired (i.e., readout frequency). The magnetization of the sample can be expressed in terms of the polarization as $M = Pn\mu$, where n is the number density of the sample and μ is its magnetic moment. Therefore,

$$\frac{S_{Hyp\,Gas}}{S_{H_2O}} = \frac{P_{Hyp\,Gas}}{P_{H_2O}} \; \frac{n_{Hyp\,Gas}}{n_p} \; \frac{\mu_{Hyp\,Gas}}{\mu_p} \; \frac{\omega_{Hyp\,Gas}}{\omega_{H_2O}}, \tag{4.51}$$

where the subscript *HypGas* refers to either ^{129}Xe or ^{3}He, n_p is the proton number density and μ_p is the proton magnetic moment. By measuring the ratio of the hyperpolarized gas and water signals which were acquired at the same readout frequency, the noble gas (hyper)polarization can be evaluated from

$$P_{Hyp\,Gas} = P_{H_2O} \; \frac{n_p}{n_{Hyp\,Gas}} \; \frac{\mu_p}{\mu_{Hyp\,Gas}} \; \frac{S_{Hyp\,Gas}}{S_{H_2O}}. \tag{4.52}$$

The ratio of magnetic moments can be determined immediately: $\mu_p = 2.793\mu_N$, $\mu_{Xe} = 0.780\mu_N$, and $\mu_{He} = 2.127\mu_N$, where μ_N is the nuclear magnetic moment. Therefore, $\mu_p/\mu_{Xe} = 3.58$ and $\mu_p/\mu_{He} = 1.31$.

The number density is commonly expressed in units of *amagat*, which is defined as the number density per standard atmosphere ($p = 1$ atm, $T = 273$ K). Thus, from the ideal gas law ($pV = nRT$, where R is the universal gas constant), 1 amagat = 44.50 mol/m^3. For water at $T = 25$°C,

$$n_{H_2O} = \frac{\rho_{H_2O}\left[\frac{\mathrm{g}}{\mathrm{m}^3}\right]}{\rho_{H_2O}^{molar}\left[\frac{\mathrm{g}}{\mathrm{mol}}\right]} \; \frac{[\mathrm{amagat}]}{44.50\left[\frac{\mathrm{mol}}{\mathrm{m}^3}\right]} \,. \tag{4.53}$$

Since at $T = 25$°C, $\rho_{H_2O} = 997 \times 10^3$ g/m^3, and $\rho_{H_2O}^{molar} = 18$ g/mol, it follows that

$n_{H_2O} = 1244.69$ amagats. Because there are two protons in each water molecule, the proton number density is $n_p = 2489.4$ amagats.

For hyperpolarized gas, the number density in *amagats* is a function of the gas pressure $p_{Hyp\,Gas}$ normalized to 1 atm; the temperature of the gas when the cells were filled, $T_{Hyp\,Gas}$, normalized to 273 K; and the abundance F of the spin-1/2 gas in the gas mixture:

$$n_{Hyp\,Gas} = \frac{p_{Hyp\,Gas}\,[\mathrm{atm}]}{1\,[\mathrm{atm}]}\,\frac{273\,[\mathrm{K}]}{T_{Hyp\,Gas}\,[\mathrm{K}]}\,F_{Hyp\,Gas}\,[\mathrm{amagat}]\,. \tag{4.54}$$

The xenon cell used for hyperpolarized ^{129}Xe experiments was filled with 0.48 atm of naturally abundant ^{129}Xe ($F_{Xe} = 26.44\% = 2.644 \times 10^{-3}$) at room temperature (300 K). The ^{129}Xe number density in the cell was thus $n_{Xe} = 0.115$ amagats. The helium cell used for all the hyperpolarized ^{3}He experiments was filled with 0.74 atm of pure ^{3}He ($F = 100\% = 1$) at room temperature. Therefore, the number density of ^{3}He in the cell was $n_{He} = 0.6825$ amagats. Table 4.1 summarizes the gas content of the cells.

	Hyp Gas Pressure (atm)	Nitrogen Pressure (atm)
^{129}Xe Cell	0.48	0.14
^{3}He Cell	0.75	0.10

Table 4.1: The gas content of ^{129}Xe and ^{3}He cells used at Stanford. All pressures measured at room temperature.

The thermal polarization of water protons is equal to the fraction of protons which are in the lower energy state , $N\uparrow/N_{total}$, minus the fraction of protons that are in the upper energy state, $N\downarrow/N_{total}$:

$$P^{thermal}_{H_2O} = \frac{N\uparrow - N\downarrow}{N\uparrow + N\downarrow}. \tag{4.55}$$

Using the Boltzmann distribution, we can express the number of protons in the lower energy state in terms of the number of protons in the higher energy state:

$$N\uparrow = N\downarrow \exp\left(\frac{\Delta E}{kT}\right) = N\downarrow \exp\left(\frac{\hbar\gamma B_\circ}{kT}\right). \tag{4.56}$$

Substituting this relation into Eq. 4.55 we get

$$P = \left[\frac{1 - \exp\left(-\hbar\gamma B_\circ/kT\right)}{1 + \exp\left(-\hbar\gamma B_\circ/kT\right)}\right] = \tanh\left(\frac{\hbar\gamma B_\circ}{2kT}\right). \tag{4.57}$$

At high temperatures T or small magnetic fields $B_\circ$ the hyperbolic tangent can be expanded in a power series. If only the first power term is kept, the thermal polarization becomes

$$P \sim \frac{\hbar\gamma B_\circ}{2kT} = \frac{\mu_p B_\circ}{kT}, \tag{4.58}$$

since $\Delta E = 2\mu_p B_\circ = \hbar\gamma B_\circ$ for a spin 1/2 particle. Notice that $\mu_p = 8.8 \times 10^{-11}$ eV/mT, $kT = 0.0258$ eV at room temperature, and $B_\circ = 397$ kHz/42.58 $\frac{\text{kHz}}{\text{mT}}$. The thermal polarization of water at room temperature and 397 kHz readout frequency is thus $P_{H_2O} = 3.18 \times 10^{-8}$.

It only remains to evaluate the ratio of hyperpolarized gas and water signals. We collected FID signals of distilled water using no polarizing waveform, so that the signal was entirely due to the thermal polarization at the readout frequency (397 kHz). Since the longitudinal relaxation time–which characterizes the rate of growth of thermal polarization in the applied magnetic field–was measured to be around 2.4 s for distilled water, we started signal acquisition approximately $3T_1$ or 7 s after the application of the readout pulse. This "waiting period" enabled the protons to reach thermal equilibrium levels before the collection of the FID signal. The hyperpolarized gas and water FID signals were collected using 90-degree flip-angles for maximum SNR.

Both water and hyperpolarized FID signals were Fourier transformed into the frequency domain and then analyzed using Matlab. First, the DC background level of both spectra was estimated using a linear fit through the noise tails (see Figure 4.4 and 4.5) and then subtracted from the main signal magnitude. This procedure removed any undesired impulse which could have appeared in the time domain signal at $t = 0$ as a result of electronic circuitry.[10] The areas under the gas and water spectral curves were then estimated by integrating the spectral function from one noise tail to the other. Finally, the gas polarization was estimated using Eq. 4.52.

We also compared the noise levels of water and hyperpolarized gas signals. In principle,

---

[10] One possible source of the impulse at $t = 0$ is the digital filter which could be coupling the switching noise into the AD converter.

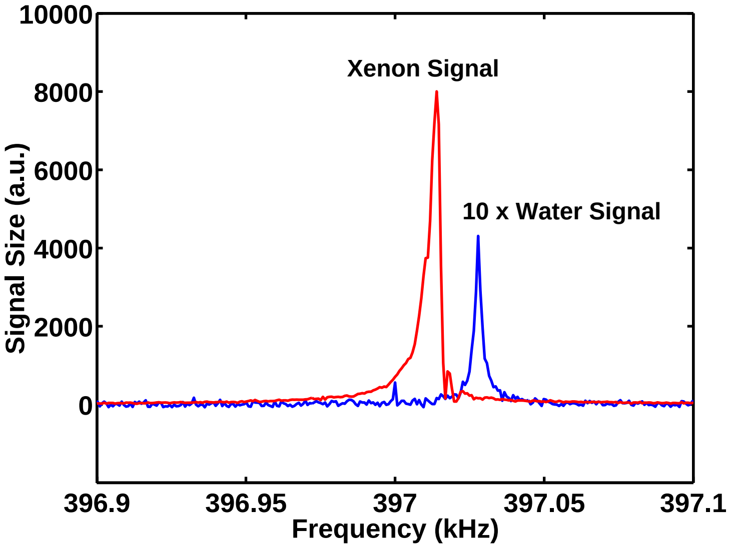

Figure 4.4: Xenon and water spectra used to calibrate xenon polarization levels.

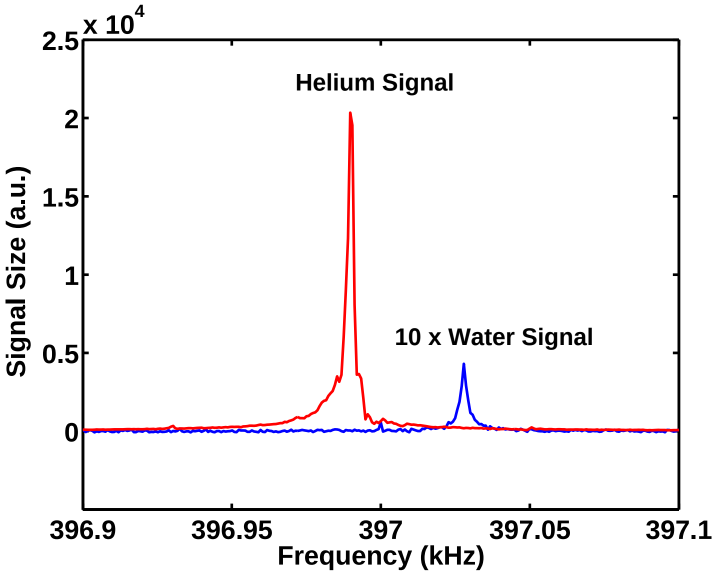

Figure 4.5: Helium and water spectra used to calibrate helium polarization levels.

if the water and gas signals were obtained on the same day, under the same conditions, the noise levels of both signals should have been comparable in size, because the dominant source of noise at the readout frequency of 397 kHz was the coil, which was the same for both samples. Therefore, a mismatch in the water and gas noise levels could indicate that the low-field pulsed resistive system response has changed after the collection of one spectra and before the collection of the other. One possibility is phase noise, which is a consequence of variations in the phase of the readout magnet that result when the magnet heats up. Unfortunately, phase noise is a function of signal size and thus can change the SNR response of the system. It is thus impossible to retroactively correct the signal size by scaling the signals with the ratio of noise levels. The noise levels of water and hyperpolarized gas in our measurements were within 70% of each other, which means that the ratio of hyperpolarized gas and water areas is at best 30% accurate. The errors in estimating other factors in Eq. 4.52 are negligible compared to the error in the estimation of the areas. The calibration of noble gas polarization is thus 30% accurate. This level of accuracy was satisfactory, since our goal at Stanford was not precise polarimetry, but to explore the versatile function of the low-field pulsed resistive system in imaging water and hyperpolarized gas.

Figure 4.4 shows ^{129}Xe and water spectra plotted on the same scale, while Figure 4.5 shows ^{3}He and water spectra. The typical ^{129}Xe polarization after 5 min of pumping with 7 W of circularly polarized laser power was between 2% and 7%, while after 30 min of pumping with 7 W of laser power we were able achieve polarizations of around 1% for ^{3}He.

4.5.2 Adiabatic Condition for Spin Transition in the Pulsed Scanner

Unlike water, which requires a polarizing field to increase its thermal polarization levels, the hyperpolarized gas polarization is created by the optical pumping process and thus does not require a polarizing waveform in the pulse sequence. Therefore, in the hyperpolarized gas experiments, only the readout field $B_\circ$ was used. However, due to its pulsed nature, the readout field is constantly turned *on* and *off* during imaging. While *off*, the noble gas magnetization is aligned with the Earth's field, which in the low-field pulsed resistive scanner is not parallel to the readout field. In contrast, during the *on* state, the magnetization aligns with the readout field which is two orders of magnitude bigger than the Earth's field. If this transition (see Figure 4.6) were nonadiabatic, significant polarization losses could occur.

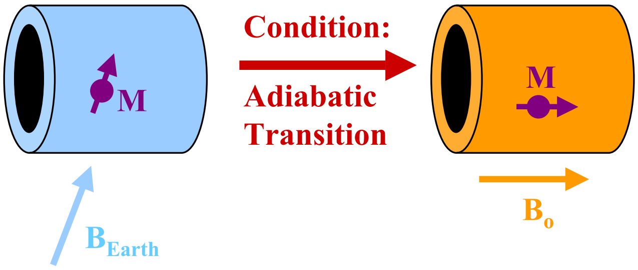

Figure 4.6: A schematic representation of the hyperpolarized gas magnetization alignment during imaging on the low-field pulsed resistive scanner. Left: magnetization alignment before the application of $B_\circ$ field. Right: magnetization alignment after the application of $B_\circ$ field. An adiabatic transition between the two states is required to prevent polarization loss.

We now compute the maximum ramping speed of the readout field allowed by the adiabatic condition. The adiabatic condition dictates the rate of change of the angle between the Earth's field B_E and the effective field $B_{eff}(t)$ (Figure 4.7). In the worst-case scenario, the Earth's field and the readout field are orthogonal.[11] The angle θ between B_{eff} and B_E can be expressed in terms of the time-varying readout field $B_\circ = tB_{max}/T_{ramp}$, where B_{max} is the saturation value of the readout field and T_{ramp} is the time it takes the readout field to reach its saturation value (see Figure 4.7),

$$\theta(t) = \arctan\left(\frac{tB_{max}}{T_{ramp}B_E}\right) \equiv \arctan\left(\frac{t}{\alpha}\right), \tag{4.59}$$

where $\alpha \equiv \frac{T_{ramp}B_E}{B_{max}}$. Thus,

$$\dot{\theta}(t) = \frac{\alpha}{(t^2+\alpha^2)}. \tag{4.60}$$

The transition will be adiabatic if the frequency of precession around the effective magnetic field is much bigger than the rate of change of θ. Therefore, $\dot{\theta}(t) \ll \gamma B_{eff}$, where

$$\gamma B_{eff} \quad = \quad \gamma\left[B_\circ^2(t)+B_E^2\right]^{1/2}$$

---

[11] Even though the Earth's field was not orthogonal to the readout field in the low-field pulsed resistive scanner, the worst-case scenario is a valid scenario at the beginning of the ramping period, when $B_\circ(t<0)=0$. The readout field ramping time which we derive in this section can be viewed as an upper limit on the ramping time that allows an adiabatic change of magnetization alinement. The ramping time could be shorter if we created a special readout-field pulse.

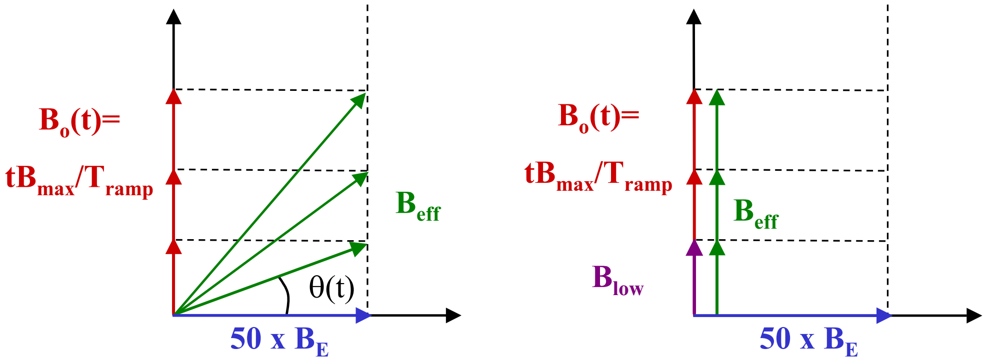

Figure 4.7: A vectorial representation of the hyperpolarized gas magnetization transition during the ramping of the readout field. Left: Without the background field. Right: With small background field, $\mathbf{B_{low}}$, along z-direction.

$$\begin{aligned} &= \gamma\left[\left(\frac{B_{max}t}{T_{ramp}}\right)^2 + B_E^2\right]^{1/2} \\ &= \gamma\frac{B_{max}}{T_{ramp}}\sqrt{t^2+\alpha^2}. \end{aligned} \tag{4.61}$$

The adiabatic condition can also be expressed as a ratio,

$$\frac{\dot{\theta}(t)}{\gamma B_{eff}(t)} = \frac{\alpha^2}{\gamma B_E\left[t^2+\alpha^2\right]^{3/2}} \ll 1. \tag{4.62}$$

Worst case occurs when $t = 0$. Thus,

$$\begin{aligned} \frac{\dot{\theta}(0)}{\gamma B_{eff}(0)} = \frac{1}{\gamma B_E \alpha} &\ll 1 \\ \Rightarrow T_{ramp}\left(\frac{B_E}{B_{max}}\right) &\gg \frac{1}{\gamma B_E}\,. \end{aligned} \tag{4.63}$$

In our case, $B_E \approx 50\ \mu$T and $B_{max} = 25$ mT. Hence,

$$\begin{aligned} T_{ramp} &\cong 200 \text{ ms for } {}^3\text{He} \\ &\cong 600 \text{ ms for } {}^{129}\text{Xe}. \end{aligned} \tag{4.64}$$

The results tell us that the magnetization will change adiabatically if the initial ramp-up time of the readout field is at least 200 ms long for ^{3}He and 600 ms long for ^{129}Xe. However, T_{ramp} is limited by the magnet rise-up time L/R, where L and R are the coil's inductance and resistance, respectively. For the readout magnet, the rise-up time is approximately 50 ms–a time too short for the adiabatic transition of hyperpolarized gas magnetization. A different method was thus needed to achieve an adiabatic sweep.

The problem was solved by applying a small offset current to the readout magnet in order to dominate the Earth's field and prevent the angle change during the *off* state of the readout field. The situation is illustrated on the right side of Figure 4.7. In this new operational mode, the readout magnet was never completely *off*–it was either on a high mode setting (which determines the readout frequency) or on a low mode setting (typically, 1 mT). A modified pulse sequence is shown in Figure 4.8.

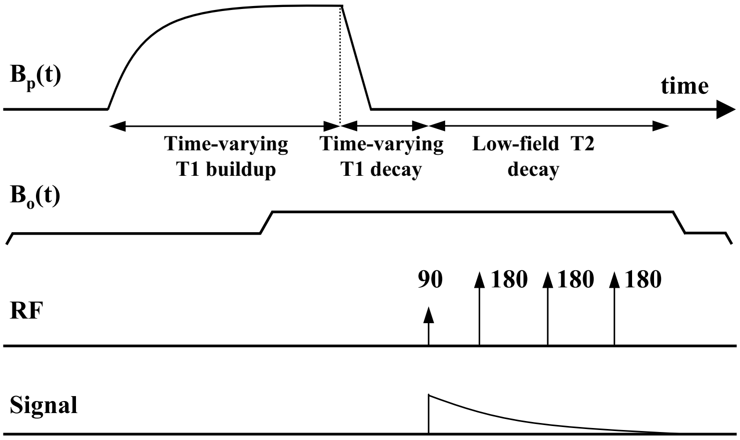

Figure 4.8: Timing diagram of a typical PMRI pulse sequence with a modified $B_\circ$ waveform. Unlike in the diagram of Figure 3.2, the $B_\circ$ is now on a low-field setting before the application of the B_p pulse.

To demonstrate experimentally that a fraction of polarization is lost without the low field enabled during the *off* mode of the readout magnet, we performed measurements of FID amplitude with and without the background (low) field present. We observed anywhere between 30% to 70% loss in hyperpolarized magnetization when the low-field setting was disabled. The wide spread in measurements was due to our inability to control precisely the parameters which affect the initial value of the gas magnetization, such as the time it takes to walk the cell from the pumping setup into the imaging scanner. Using this method we were also not able to determine accurately the minimal value of the low field required to prevent magnetization losses. Instead, we performed an experiment which gave a negative result (i.e., no signal) when the low field was *on*, and a positive result (i.e., signal) when the low field was *off*.

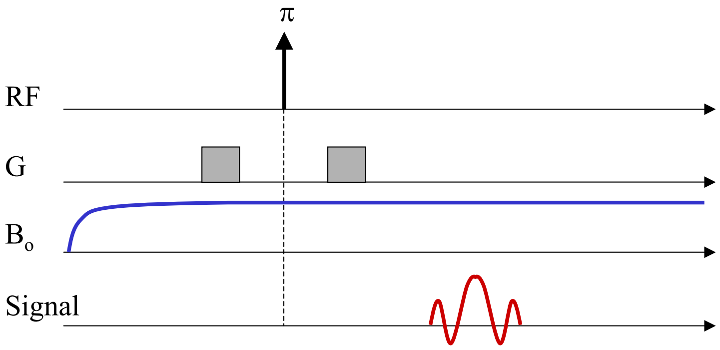

Figure 4.9: Pulse sequence used for demonstrating the non-adiabatic ramp-up of $B_{\circ}$ pulse in the absence of the low-field setting.

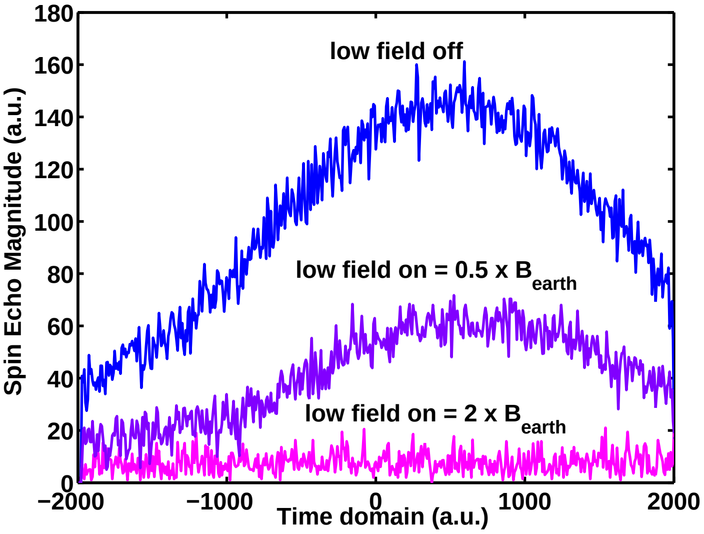

Figure 4.10: Creation of spin echoes demonstrating the existence of transverse magnetization before the ramp-up of the $B_{\circ}$ pulse: without the background field, with background field $= 25\ \mu$T and with background field $= 100\ \mu$T.

The experiment relied on the creation of a spin echo using a 180-degree pulse, a technique we described in Section 4.3.1. Figure 4.9 shows the sequence used in the experiment. Notice that there is no 90-degree pulse in this sequence, which would normally flip the magnetization from the z-axis on to the xy plane. Nevertheless, a spin echo was created after the 180-degree pulse. This indicated the presence of transverse magnetization before the (non-adiabatic) ramp-up of the $B_{\circ}$ field. On the other hand, if the low-field setting was enabled, the magnetization was aligned entirely along the z-direction before the ramp-up of the $B_\circ$ field, and consequently, no echo was formed. A small "crusher" (i.e., destructive) gradient was applied to destroy the FID signal which would result from an imperfect 180-degree pulse.

Figure 4.10 shows the results of spin echo experiments, confirming the need for the low-field setting during the *off* mode of the readout field cycle. When the low field was smaller than 0.1 mT (twice the Earth's field), an echo was created, which proves that transverse magnetization existed before the ramp-up of $B_\circ$ field. This transverse magnetization would have either been lost after the non-adiabatic ramp-up or, in the case of spin echo sequence, could contribute to the creation of stimulated echoes. From the results in Figure 4.10 we were able to conclude that the minimum (critical) field needed to prevent polarization loss was 0.1 mT. The low field used in our experiments was 1 mT, which is well above the critical value.

4.6 Measurements of Irreversible Transverse Relaxation Using CPMG Sequence

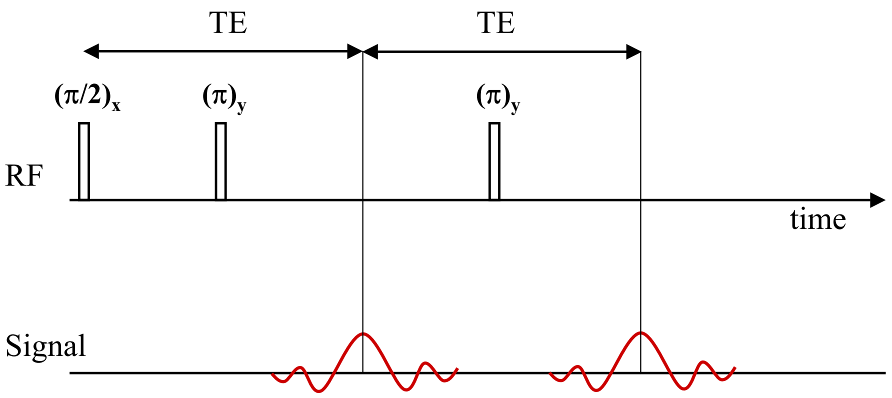

Figure 4.11: Pulse sequence used to generate a Carr-Purcell-Meiboom-Gill echo train.

The irreversible T_2 relaxation, given by the Eq. 4.23, describes the decay of a spin echo train in a Carr-Purcell-Meiboom-Gill sequence. The basic sequence used to create a spin echo train is illustrated in Figure 4.11. First, a 90-degree pulse was applied along one of the transverse axis (either x or y). A time $TE/2$ later, a 180-degree pulse was applied along the other transverse axis (either y or x). The 180-degree pulse flips the spins in the transverse plane (around either y or x axis) and causes a spin echo to appear at time TE after the application of the 90-degree pulse. By reapplying the 180-degree pulses in equally spaced intervals of length TE, an echo gets created each time at a half point ($TE/2$) between the 180-degree pulses. Since TE equals the length between two successive echoes, it is also called "interecho time". The axis of rotation of the 180-degree pulses (which is related to the phase of the RF pulses) has to be parallel to the orientation of magnetization [29]. For instance, after the application of a 90-degree pulse which rotates the spins around the x-axis, the spins are aligned along the y-axis; consequently, the 180-degree pulses have to be applied along the y-axis. This algorithm prevents the accumulation of errors from imperfect 180-degree pulses.

Figure 4.12 shows an example of ^{3}He and ^{129}Xe spin echo trains obtained on the low-field pulsed resistive scanner. Each plot contains 32 echoes. The interecho time for ^{3}He was 57.03 ms, while the TE for ^{129}Xe was 67.34 ms. There is nothing fundamental about the

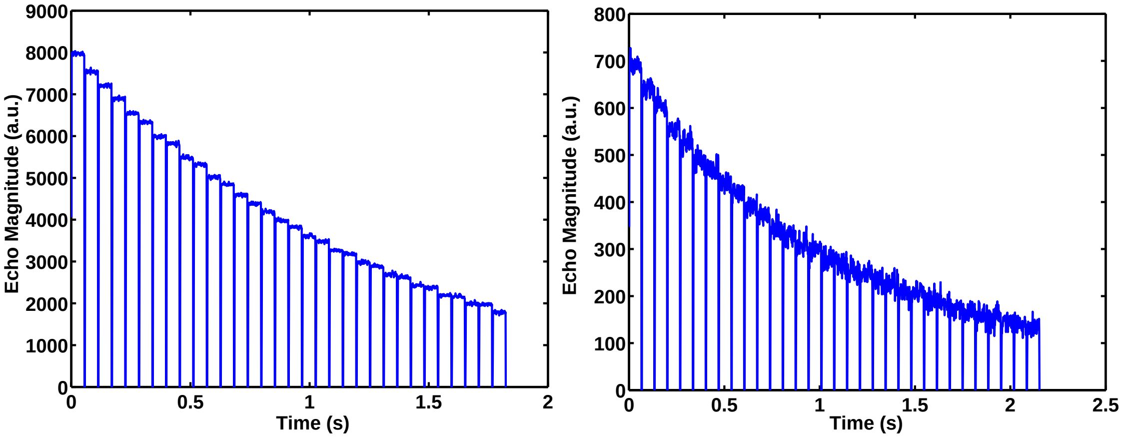

Figure 4.12: ^{3}He (left) and ^{129}Xe (right) spin echo trains obtained with the CPMG sequence.

TE times used in these experiments. The TE values were chosen so that we could display clearly the T_2^{CPMG} relaxation experienced by the gas during the acquisition window.

To extract the T_2^{CPMG} time constant from the echo trains such as the ones shown in Figure 4.12, we perform a least-square fit to the logarithm of the data.[12] The fit is a straight line of the form

$$\ln(S) = -\frac{t}{T_2^{CPMG}} + \ln S_\circ \rightarrow y = -tk + n, \tag{4.65}$$

where $y = \ln S$ is the natural log of the average (mean) echo magnitude, which was obtained by integrating the area under each echo; $n = \ln S_\circ$ is the natural log of the initial echo magnitude; and $k = 1/T_2^{CPMG}$ is the relaxation rate of the spin echo train in the CPMG sequence. Figure 4.13 shows experimental data as well as the fit to the data (using Eq. 4.65) of average echo magnitude as a function of time during a CPMG sequence. The T_2^{CPMG} relaxation time obtained from the fit was 49.5 s.

Measurements of T_2^{CPMG} showed a strong dependence of T_2^{CPMG} relaxation time on the interecho time TE. Consequently, unique ^{3}He and ^{129}Xe T_2^{CPMG} relaxation times do not exist. However, the dependence of T_2^{CPMG} on the interecho time is important for determining the inherent T_2 relaxation rate of gases, which is the subject of Section 4.8. In that section we study the functional dependence of T_2^{CPMG} on TE and develop a method for extracting the inherent T_2 relaxation time from the T_2^{CPMG} data.

In the following two subsections we examine in more detail two common problems en-

---

[12] In Matlab, the least-square algorithm is implemented into the function *polyfit* which we used for fitting the data.

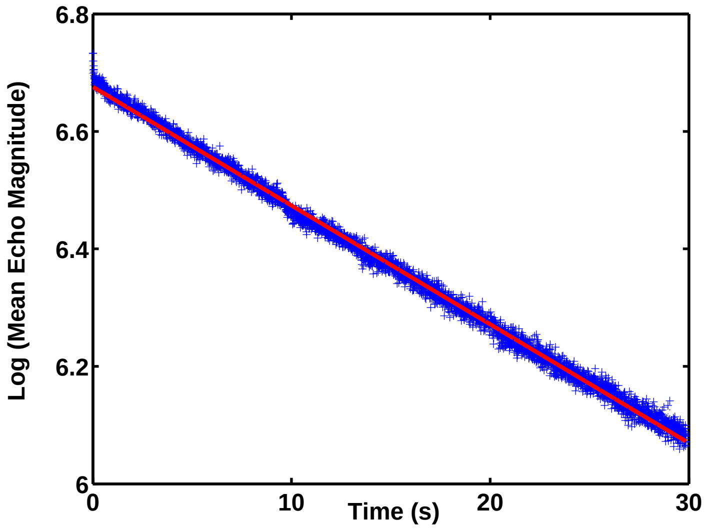

Figure 4.13: A logarithmic plot of the average measured ^{129}Xe spin echo magnitude as a function of time and best fit to the data. Number of echoes=4096, TE=7.29 ms, T2 extracted from the plot=49.5 s.

countered when using the CPMG spin echo sequence on the low-field pulsed resistive scanner: the generation of stimulated echoes and the off-resonance effects resulting from the resistive heating of the magnet.

4.6.1 Errors in RF Pulse Calibration and Stimulated Echoes

The duration of the RF pulses determines the magnetization flip-angle according to the Eq. 4.48. The magnitude of B_1 field in Eq. 4.48 is a function of the shape and size of the RF coil, the strength of the current in the coil, and the position of the sample within the coil. If the sample *fills* the coil (i.e., the coil fits tightly around the sample), the magnitude of B_1 can vary significantly across the sample. For all these reasons, the magnitude of B_1 is not known *a priori* and the flip-angle calibration has to be determined experimentally. The common procedure is to look for a null in the FID signal–a result of a 180-degree flip–while systematically increasing the duration of the B_1 pulse. However, this method is not practical for hyperpolarized gases since ($M_\circ \sin\alpha$) of noble gas magnetization is destroyed after each α-degree pulse. We therefore always calibrate the RF pulses on a water phantom and then scale the duration of the B_1 pulse by the ratio of gas and water gyromagnetic moments. For a flip-angle α, the duration of the B_1 field in the case of hyperpolarized gas,

$T_\alpha^{Hyp\,Gas}$, and in the case of water, $T_\alpha^{H_2O}$, are related by

$$\begin{aligned} \alpha &= \gamma_p\, B_1\, T_\alpha^{H_2O} = \gamma_{Hyp\,Gas}\, B_1\, T_\alpha^{Hyp\,Gas} \\ &\rightarrow\ T_\alpha^{Hyp\,Gas} = \frac{\gamma_p}{\gamma_{Hyp\,Gas}}\, T_\alpha^{H_2O}. \end{aligned} \tag{4.66}$$

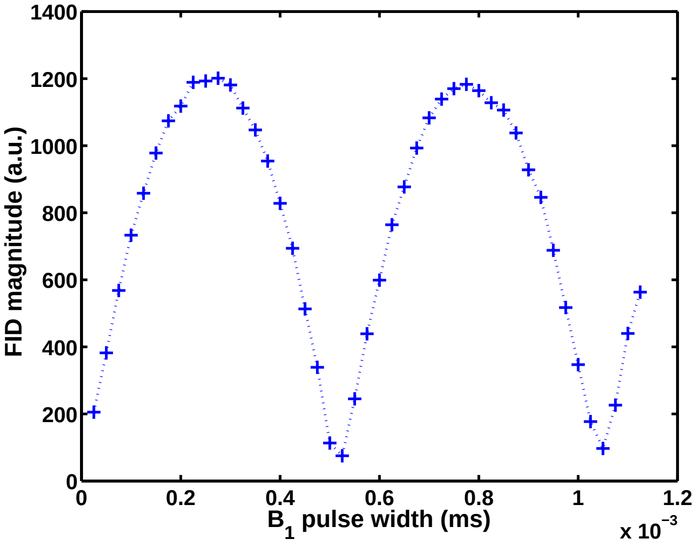

Figure 4.14: Measurement of FID magnitude as a function of B_1 pulse duration.

Figure 4.14 is an example of RF pulse calibration. It displays the magnitude of the FID signal at time $t = 0$ as a function of B_1 pulse width. As predicted from

$$M_{xy} = M_\circ \left|\sin\left(\gamma B_1 T_\alpha\right)\right|, \tag{4.67}$$

the dependence of the FID magnitude on the B_1 pulse width is sinusoidal. The maximum FID values correspond to odd multiples of $\pi/2$ (90° and 270°), while the nulls correspond to even multiples of $\pi/2$ (180° and 360°). Measurements such as this one enabled us to determine the width of B_1 for any flip-angle.

One of the implication in using the above-described calibration procedure is that any error in measuring the width of the 180-degree pulses translated into an error in the RF flip-angle. The accuracy in determining the width of a 180-degree pulse when looking for a null in the FID signal was ± 1 μs. The width of the 180-degree pulse depended on the signal attenuation used in producing the magnitude of B_1 pulse. With the attenuation most commonly used, the length of 180-degree pulse for water was around 120 μs. Thus, the error in the RF flip-angle could be as high as 0.8%-1%. This means that in the CPMG sequence, around $\sin(180 - 0.01 \times 180) = 3\%$ of the initial magnetization might end up along the longitudinal axis after each 180-degree pulse. This would cause an accelerated decay of the transverse component M_{xy}. In addition, the magnetization stored along the longitudinal axis would eventually be knocked back into the transverse plane by an imperfect 180-degree pulse and contribute to the creation of stimulated echoes. Such echoes were observed occasionally during our measurements. Figure 4.15 shows an example of an echo train that produced stimulated echoes in the second half of the train. We attribute this effect to miscalibrated 180-degree pulses.

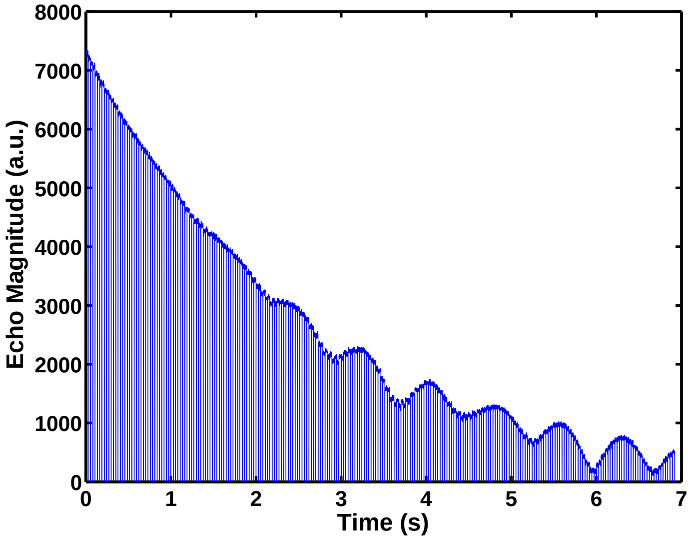

Figure 4.15: An example of the occurrence of stimulated echoes during a CPMG spin echo train. Number of echoes=256, TE=27.03 ms.

4.6.2 Heating of the Magnet and Off-Resonance Effects

One of the challenges in using resistive magnets for MR imaging is temporal instability of the magnetic field due to the resistive heating of the copper wires. The heat causes the copper wires to expand outward from the center of the magnet bore–a process, which changes the strength of the magnetic field at the position of the sample. In addition, the increase in the temperature of the wires increases their resistance and, as a result, the power of the magnetic field changes. The temporal instability of the $B_\circ$ field causes drifts in the readout frequency and therefore, phase errors. In Section 3.4.1 we showed that for a field-of-view of 10 cm and a resolution of 1 mm, the temporal stability of the magnet should be better than 100 ppm.

The temporal drifts in the readout field are particularly damaging in the case of CPMG sequence, which has stringent phase stability requirements. In Section 4.3.1 we derived an expression (Eq. 4.20) for the complex transverse magnetization in the rotating frame after the application of a 180-degree pulse, for the case of time-dependent local fields b_j. In that derivation we made an assumption that stationary spins (unlike freely diffusing spins) see a constant, time-independent field, which enabled us to solve the integral in Eq. 4.20. That assumption no longer holds when the local fields change due to temporal instabilities arising from resistive heating of the magnet. In such a case, the two exponential terms in Eq. 4.20 no longer cancel out. The situation is conceptually similar to the case of diffusing spins; the only difference is in the source of the temporal field variation.

To solve the time integrals in Eq. 4.20, we need to make an assumption about the form of the $b_j(\tau)$ field. To first order, the field drifts linearly with time, so that $b_j(\tau) = b_\circ + \alpha t$, where $b_\circ$ is the Larmor frequency of the individual spin, and $\alpha = \partial b/\partial t$. Equation 4.20 then reduces to

$$\begin{aligned} M(2t_1) &= \frac{1}{N}\sum_{j=1}^{N} \exp\left[-i\gamma\alpha_j t_1^2\right] M^*(0) \\ M(t) &= \frac{1}{N}\sum_{j=1}^{N} \exp\left[-\frac{i}{4}\gamma\alpha_j t^2\right] M^*(0). \end{aligned} \tag{4.68}$$

Assuming all spins see the same field variation $\partial b_j/\partial t \equiv \partial B/\partial t$, the sum over all spins reduces to

$$M(t) = \exp\left[-\frac{i}{4}\frac{\partial(\gamma B)}{\partial t}t^2\right] M^*(0). \tag{4.69}$$

The above equation represents the complex magnetization at time t in terms of the initial magnetization (at $t = 0$). We see that unlike in the case of time-independent field, the echo for a linearly drifting field is phase shifted with respect to the original signal. As a result, the axis of rotation is no longer parallel to the magnetization–a situation which violates the CPMG condition (see beginning of Section 4.6). As the echo train progresses, transverse phase errors diverge. This leads to the growth of the longitudinal magnetization, a faster decay of transverse magnetization and, potentially, to stimulated echoes, as discussed in Section 4.6.1.

Measurements of T_2^{CPMG} presented in Section 4.6 (see Figure 4.13) demonstrate that our resistive system can maintain sufficient temporal stability to acquire as many as 4096 echoes in the time period of 30 s. This was an important milestone in investigating the use of resistive pulsed low-field magnets for hyperpolarized gas imaging.

4.7 Measurements of Diffusion Using PGSE Sequence

To determine the relaxation rate arising from the diffusion of spins through magnetic field gradients ($1/T_D$ in Eq. 4.23), we need to know the value of diffusion coefficients for the gas mixture used in our experiments. Appendix A gives a theoretical estimation of the observable diffusion coefficients of ^{129}Xe and ^{3}He in the binary gas mixture with nitrogen gas, based upon Lennard-Jones potentials. For measurements of ^{129}Xe diffusion, a cell containing 0.48 atm of naturally abundant ^{129}Xe and 0.14 atm of nitrogen was used. The theoretical calculation gave an observable diffusion coefficient for ^{129}Xe of $(1.08 \pm 0.08) \times 10^{-5}$ m^2/s. For measurements of ^{3}He diffusion, we used a cell that contained 0.75 atm of pure ^{3}He gas and 0.1 atm of nitrogen. The calculations yielded an observable diffusion coefficient for ^{3}He of $(1.77 \pm 0.12) \times 10^{-4}$ m^2/s. The diffusion coefficient of water is 2.26×10^{-9} m^2/s [84].

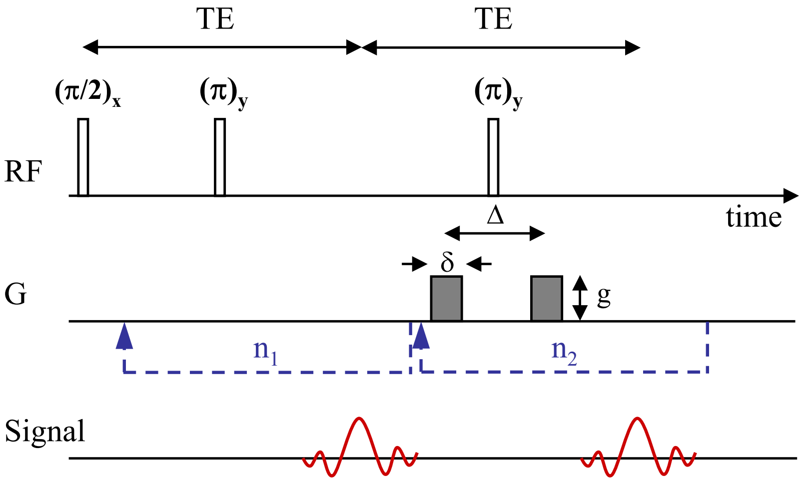

Figure 4.16: Pulse sequence used for measuring diffusion coefficients of hyperpolarized gases and water. First n_1 loops: no gradients used; last n_2 loops: bipolar gradients with amplitude = g, width = δ, separation = Δ.

The pulse sequence used for measurements of the diffusion coefficients is shown in Figure 4.16. A pair of bipolar pulsed gradients of size g, width δ, and separation Δ, was added between each acquisition to the standard CPMG sequence (Figure 4.11). Since each 180-degree pulse inverts the sign of the preceding gradients, the area under the gradient waveform is zero at the time of each acquisition. The first n_1 echoes were acquired with the gradient amplitude set to zero, while the last n_2 echoes were acquired at a fixed value of g.

As a result, there was an extra decay due to diffusion in the bipolar gradients during the last n_2 echoes only.

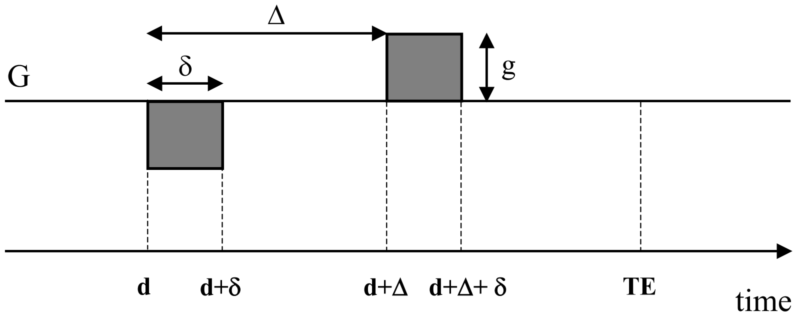

Figure 4.17: Bipolar gradient waveform used in the diffusion sequence as a function of time.

To find this decay, we refer back to the Eq. 4.41 [59],

$$A(t) = A_\circ \exp\left[-D\gamma^2 \int_0^t \left(\int_0^{t'} \mathbf{g}(t'')dt''\right)^2\right]. \tag{4.70}$$

The signal decay due to diffusion is obtained by integrating the gradient waveform over time. The bipolar gradients used in our diffusion experiments (Figure 4.16) are displayed again in Figure 4.17, this time explicitly showing the sign inversion of the first gradient lobe due to the 180-degree pulse. The time integral of $\mathbf{g}$ from the beginning of the waveform to the occurrence of the spin echo at time $t = TE$ is

$$\int_0^{t'} \mathbf{g}(t')dt'' = \begin{cases} 0 & 0 < t < d \\ -g(t' - d) & d < t < d + \delta \\ -g\delta & d + \delta < t < d + \Delta \\ -g\delta + g(t' - d - \Delta) & d + \Delta < t < d + \Delta + \delta \\ -g\delta + g\delta & d + \Delta + \delta < t < TE \end{cases} \tag{4.71}$$

and the time integral of $\mathbf{k}^2$ is

$$\begin{aligned} \int_0^t \left(\int_0^{t'} \mathbf{g}(t'')dt''\right)^2 &= -\int_d^{d+\delta} g^2(t' - d)^2 dt' - \int_{d+\delta}^{d+\Delta} g^2\delta^2 dt' \\ &\quad + \int_{d+\Delta}^{d+\Delta+\delta} \left[g^2\delta^2 - 2g^2\delta(t' - d - \Delta) + g^2(t' - d - \Delta)^2\right] dt' \end{aligned}$$

$$= \quad g^2\delta^2\left(\Delta-\frac{\delta}{3}\right). \tag{4.72}$$

To obtain the amplitude of the nth echo we need to sum n such integrals. Thus,

$$A(nTE) = A_\circ \exp\left[-D\, n\gamma^2 g^2\delta^2\left(\Delta-\frac{\delta}{3}\right)\right], \tag{4.73}$$

where D is the diffusion coefficient of the sample, $A_\circ$ is the initial signal amplitude, and γ is the gyromagnetic ratio in radial units (i.e., rad/s/T).

We are now able to express the echo amplitude as a function of the interecho time TE during the diffusion sequence from Figure 4.16,

$$A(n_1TE) \quad = \quad A_\circ \exp\left(-\frac{n_1TE}{T_2^{CPMG}}\right) \tag{4.74}$$

$$A\left((n_1+n_2)TE\right) \quad = \quad A_\circ \exp\left(-\frac{(n_1+n_2)TE}{T_2^{CPMG}} - D\, n_2\gamma^2 g^2\delta^2\left(\Delta-\frac{\delta}{3}\right)\right). \tag{4.75}$$

Equation 4.74 refers to the echo amplitude of the first n_1 echoes (at times n_1TE), while Eq. 4.75 refers to the echo amplitude of the last n_2 echoes (at times $(n_1+n_2)TE$). By taking the logarithm of each equation above, we obtain two straight lines. A least-square-fit to the two lines produces four parameters–slope and intersect of the first line, P_1 and P_2, and slope and intersect of the second line, R_1 and R_2, where

$$\begin{aligned}
P_1 &= -\frac{1}{T_2^{CPMG}} \\
P_2 &= \ln A_\circ \\
R_1 &= -\frac{1}{T_2^{CPMG}} - D\frac{b}{TE} \\
R_2 &= Dn_1b + \ln A_\circ
\end{aligned}$$

and $b \equiv \gamma^2 g^2\delta^2(\Delta-\delta/3)$. The above equation can be rewritten in matrix form as $A\cdot x = B$, where

$$A = \begin{bmatrix} 0 & -1 & 0 \\ 1 & 0 & 0 \\ 0 & -1 & -\frac{b}{TE} \\ 1 & 0 & n_1b \end{bmatrix} \; B = \begin{bmatrix} P_1 \\ P_2 \\ R_1 \\ R_2 \end{bmatrix} \; x = \begin{bmatrix} \ln A_\circ \\ 1/T_2^{CPMG} \\ D \end{bmatrix}. \tag{4.76}$$

Since there are four parameters (vector B), but only three unknowns (vector x), the system is over-constrained [85].[13] The problem is then to search for the least-square solution $\bar{x}$ that minimizes the error $E = (B - A\bar{x})$. Geometrically, this translates to searching for a solution $\bar{x}$ such that the error vector E will be perpendicular to every column of A (or every row of A^T). Therefore,

$$\begin{aligned} A^T(B - A\bar{x}) &= 0 \\ \bar{x} &= \left(A^T A\right)^{-1} A^T b \qquad (4.77) \\ D &= \bar{x}(3). \qquad (4.78) \end{aligned}$$

We have demonstrated that by fitting the echo amplitudes obtained with the diffusion sequence to two straight lines, we can obtain an estimation of the diffusion constant using Eqs. 4.77 and 4.78.

Figures 4.18, 4.19 and 4.20 show an example of diffusion measurements for ^{3}He, ^{129}Xe and water, respectively. Figures on the left display the echo magnitude as a function of acquisition time, while figures on the right show the average echo magnitude plotted on a logarithmic scale as a function of real time and best linear fit to the data. From the log plots one can see a clear change in the slope of the two linear fits, which can be attributed to diffusion losses in bipolar gradients during the last n_2 echoes.

The difference in the slopes of the two straight fits depends on the parameter b (see Eq. 4.42). In the case of bipolar gradients of amplitude g, width δ, and separation Δ, the value of b for the n_2th echo is

$$b \equiv 4\pi^2 \int_0^t k^2(\tau)d\tau = n_2\gamma^2 g^2 \delta^2 \left(\Delta - \frac{\delta}{3}\right). \qquad (4.79)$$

In our experiments, we chose values of b that produced a visible change in the slope of the two linear fits. For ^{3}He, $b(n_2 = 1)$ ranged from 0.5×10^3 s/m^2 to 2×10^3 s/m^2, for ^{129}Xe from 4×10^3 s/m^2 to 2.5×10^4 s/m^2, and for water from 3.5×10^7 s/m^2 to 1.5×10^8 s/m^2. We observed that a value of b which was smaller than the lower limit of the intervals given above produced large uncertainties in the measurements of diffusion coefficients for xenon and helium, and gave unreasonable results (i.e., negative D values) for the diffusion

---

[13] There will not exist a choice of x that perfectly fits the parameters of B.

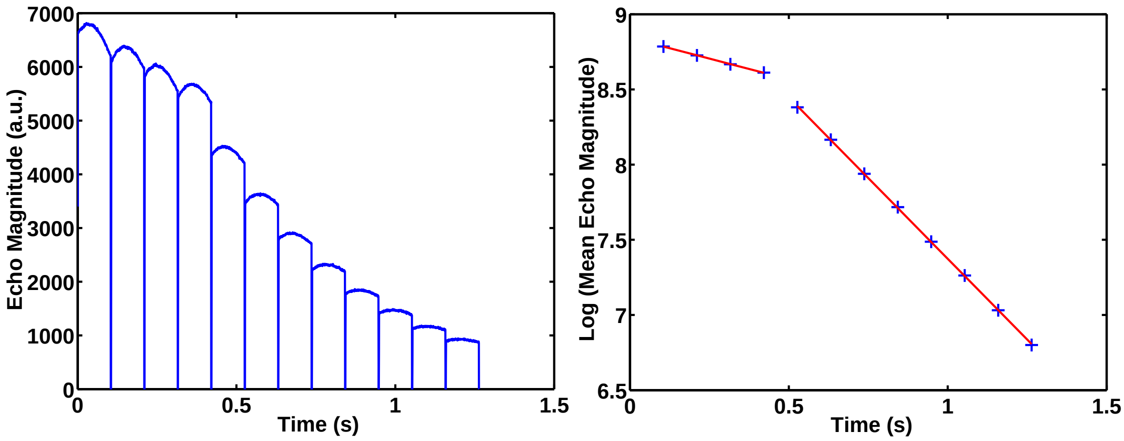

Figure 4.18: Left: ^{3}He spin echo train obtained with diffusion sequence from Figure 4.16. Right: Average echo amplitude from (right) plotted on a log scale as a function of time and best fit to data. n_1=4: g=0; n_2=8: g=0.368 mT/m; TE=105.35 ms, Δ=10.09 ms, δ=5 ms.

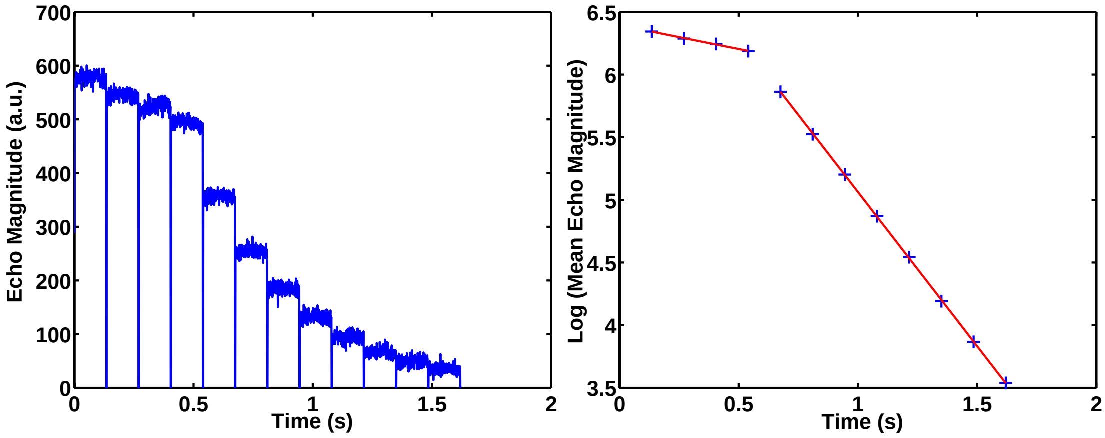

Figure 4.19: Left: ^{129}Xe spin echo train obtained with diffusion sequence from Figure 4.16. Right: Average echo amplitude from (right) plotted on a log scale as a function of time and best fit to data. n_1=4: g=0; n_2=8: g=2.76 mT/m; TE=135 ms, Δ=25.22 ms, δ=5 ms.

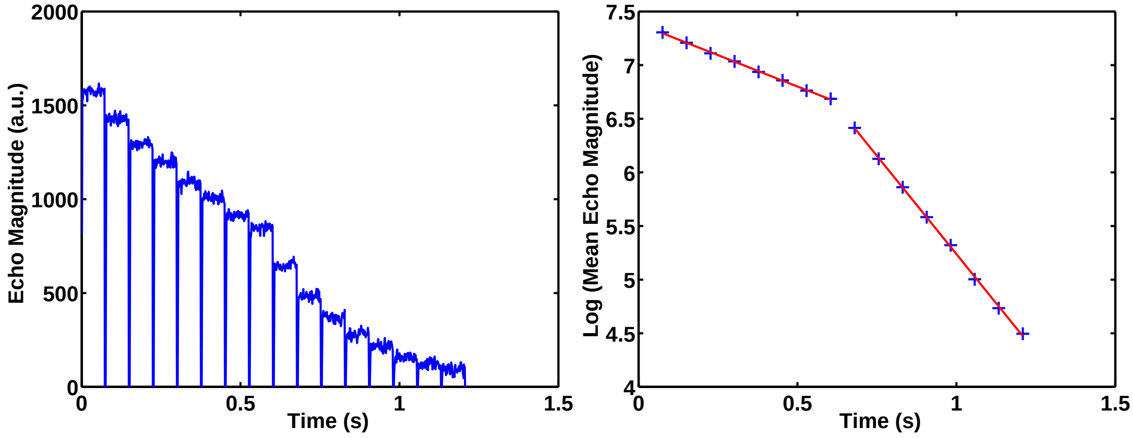

Figure 4.20: Left: Water spin echo train obtained with diffusion sequence from Figure 4.16. Right: Average echo amplitude from (right) plotted on a log scale as a function of time and best fit to data. n_1=8: g=0; n_2=8: g=13.8 mT/m; TE=75.55 ms, Δ=35.13 ms, δ=15 ms.

coefficient of water. The problem lies in the fact that a small value of b, combined with a small diffusion coefficient of water D_{H_2O}, produces a signal decay e^{-Db} which is smaller than the statistical variation of our measurements. Dividing the data into two parts and then fitting each part to a straight line can result in a negative slope difference and thus a negative diffusion coefficient.

4.7.1 Uncertainties in Determining Diffusion Coefficients of Hyperpolarized ^{129}Xe and ^{3}He

Let us first estimate the uncertainty in the theoretical estimation of diffusion coefficients for bipolar gas mixtures. Since the calculations involve many tabulated parameters, they are presented in Appendix A. From Eqs. A.2, A.4, and A.5 we see that the largest uncertainty in the estimation of observable diffusion coefficient of ^{129}Xe and ^{3}He comes from the uncertainty in the temperature of the gas inside the cell and, to a lesser extent, from the uncertainty in the pressures of the gases in the binary gas mixture. By performing simple experiments in which we measured the temperature of ^{129}Xe and ^{3}He cells during optical pumping and then again 2-5 min after cooling them in cold water, we were able to determine that the temperature of the ^{129}Xe cell was $30 \pm 10°$C, while the temperature of the ^{3}He cell (which was pumped at a higher temperature than ^{129}Xe) was $35 \pm 10°$C. The uncertainty in the pressure of gases inside the cell is directly related to the accuracy of the cell-filling process which we estimated to be ±0.01 atm.

To estimate the uncertainty in the measurement of diffusion coefficient we return to Eqs. 4.76, 4.77, and 4.78. The diffusion coefficient D is a function of the elements of matrices A and B:

$$D = \frac{TE}{b\,(1 + n_1^2\,TE^2)}\,\{P(1) - n_1\,TE\,P(2) - R(1) + n_1\,TE\,R(2)\}\,. \tag{4.80}$$

Therefore, the uncertainty in D will mainly be a function of the uncertainties in b, TE, and uncertainties in the fit parameters $P(1)$, $P(2)$, $R(1)$, $R(2)$. From Figures 4.18, 4.20 and 4.19 we can see that the fits match the data almost perfectly, so the uncertainties in the fit parameters can be ignored. The uncertainty in the interecho time should also be negligible, because the console system can generates time intervals with 10 μs accuracy, while the smallest interecho times were 5 ms. The uncertainty from the TE times would thus be less than 0.5%.

Finally, it is important to evaluate the uncertainty in the parameter $b \equiv \gamma^2 \delta^2 (\Delta - \delta/3)$. The dominant error in b comes from the gradient strength $g = \eta\, I$, where η is the gradient efficiency coefficient in units of mT/m/A, and I is the current through the gradient coils in units of Amperes. The gradient efficiencies were calibrated for each gradient coil with 5% accuracy. Since the gradient efficiency is the dominant source of uncertainty, we conclude that the measurements of ^{129}Xe, ^{3}He and water diffusion coefficients are $\Delta D/D = 2\Delta g/g =$ 10% accurate. This estimation is also consistent with the spread of D values obtained from repeated measurements.

	D (m^2/s) Experimental	D (m^2/s) Theory
^{129}Xe	(1.28 $^+$/- 0.13) x 10^{-5}	(1.08$^+$/-0.08) x 10^{-5}
^{3}He	(1.69 $^+$/- 0.17) x 10^{-4}	(1.77 $^+$/-0.12) x 10^{-4}
H_2O	(2.10 $^+$/- 0.21) x 10^{-9}	(2.0 $^+$/- 0.3) x 10^{-9}

Table 4.2: Table of experimental and theoretical values of diffusion coefficients for ^{129}Xe, ^{3}He and distilled water.

Table 4.2 summarizes the experimental values of ^{129}Xe, ^{3}He and water diffusion coefficients obtained on the pulsed low-field resistive scanner using the pulse sequence from Figure 4.16, and compares them to the theoretical values which are calculated in Appendix A. The theoretical value for the water diffusion coefficient was obtained from Piton *et.al.* [84].

4.8 Measurement of Intrinsic (Spin-Spin) T2 Relaxation Using CPMG Sequence with Variable Interecho Times

At the end of Section 4.6 we indicated that the measured T_2^{CPMG} of hyperpolarized gases depends strongly on the interecho time TE used in the CPMG sequence. We are now going to investigate this dependence in more detail.

The T_2^{CPMG} measurements showed that using longer interecho times in the CPMG sequence resulted in shorter measured T_2^{CPMG} relaxation times. This dependence is indicative of diffusion-induced losses (see Section 4.4.1) which occur when spins diffuse out of the voxel that is being inverted and refocused by the 180-degree pulse of the CPMG sequence. The longer the time between two successive 180-degree pulses (which equals the interecho time TE in Figure 4.11), the bigger the average distance travelled by the spins during that time and the bigger the loss of signal coherence. However, diffusion loss is the result of random phase accretion when spins diffuse through magnetic field gradients, and there were no external gradients used in the CPMG pulse sequence of Figure 4.11. Does this mean the reasoning just presented is flawed? Not really. Even though there were no external gradients applied during the CPMG sequence of Figure 4.11, there were gradients present due to magnetic field inhomogeneity as well as gradients due to the magnetic field susceptibility differences between air and the sample.[14] These gradients, which are constant throughout the CPMG sequence, are estimated to be small (on the order of 0.1 mT/m), yet can cause a detectable signal loss because of the large diffusion constant of gases.

To compute signal decay due to constant gradients we refer back to Figure 4.17 and Eq. 4.73. The amplitude of the nth echo in the case of constant gradients is the limiting case of Eq. 4.73, with $\delta \to TE/2$ and $\Delta \to \delta$. At time $t = nTE$,

$$\begin{aligned} A(nTE) &= \lim_{\delta=\Delta\to TE/2} \left\{ A_\circ \exp\left[-D\, n\gamma^2 g^2 \delta^2 \left(\Delta - \frac{\delta}{3} \right) \right] \right\} \\ &= A_\circ \exp\left[-\frac{1}{12}\, Dn\gamma^2 g^2 TE^3 \right]. \end{aligned} \tag{4.81}$$

---

[14] In the case of spherical glass cells, the susceptibility effects are negligible.

By adding the decay due to the inherent $T2$ relaxation, we get

$$A(nTE) = A_\circ \exp\left(-\frac{nTE}{T_2}\right) \exp\left(-\frac{1}{12}\, Dn\gamma^2 g^2 TE^3\right). \tag{4.82}$$

Since the detected relaxation rate is $1/T_2^{CPMG}$, the two exponentials can be combined into a single decay term,

$$\begin{aligned} A(nTE) &= A_\circ \exp\left(-\frac{nTE}{T_2^{CPMG}}\right), \text{ where} \\ \frac{1}{T_2^{CPMG}} &\equiv \frac{1}{T_2} + \frac{1}{12} D\gamma^2 g^2 TE^2. \end{aligned} \tag{4.83}$$

The above equation expresses the relationship between the T_2^{CPMG} relaxation time and the interecho time TE. We see that the inherent T_2 relaxation is equal to T_2^{CPMG} relaxation at $TE = 0$.

We performed T_2^{CPMG} measurements using the pulse sequence shown in Figure 4.11 and with TE times ranging from 5 ms to above 100 ms for ^{129}Xe, ^{3}He and water. We then plotted T_2^{CPMG} versus TE and fitted the data using least-square method to a two-parameter function of the form

$$F(TE) = \frac{1}{1/a + bTE^2}. \tag{4.84}$$

Using Eq. 4.83, the values of a and b give the inherent T_2 relaxation and the gradient amplitude due to the magnetic field inhomogeneities, respectively:

$$T_2 = a \tag{4.85}$$

$$g = \sqrt{\frac{12b}{D\gamma^2}}\,. \tag{4.86}$$

Since the inherent T_2 relaxation and the gradient amplitude g are independent of each other, we should obtain, within the experimental error, same T_2 relaxation times regardless of the size of the background gradients. We therefore repeated the $T_2^{CPMG}(TE)$ measurements for a range of g values (0.01 mT/m-0.4 mT/m) which were controlled with the size of the shimming currents applied to the magnetic field gradients (see beginning of Section 4.5). The measurements of T_2^{CPMG} for different g values should, in theory, converge to a single point at $TE = 0$.

Figures 4.21, 4.22, and 4.23 show the results of our $T_2^{CPMG}(TE)$ measurements for ^{3}He, ^{129}Xe, and water, respectively. Water measurements were done on distilled water as well as water doped with 0.012 molar $CuSO_4 \cdot 5H_2O$–a substance which decreases the T_2 relaxation time of water. Only the results for the distilled water are shown. The water measurements should show no variation in the measured T_2^{CPMG} beyond the statistical error because of the small diffusion constant of water (see Section 4.7). This is confirmed in Figure 4.23. The average T_2 relaxation time of distilled water was 1 s, while T_2 of doped water was around 42 ms. Both results are in agreement with expectations.

Analysis of the three sets of ^{129}Xe T_2^{CPMG} data in Figure 4.22 results in an inherent T_2 relaxation of ^{129}Xe equal to 46.7 ± 0.5 s. On the other hand, the inherent T_2 relaxation time of ^{3}He for the two sets of data in Figure 4.21 is equal to 19.2 ± 4.5 s. In the next section we examine the sources of errors involved in obtaining this data.

4.8.1 Uncertainties in Determining Inherent T2 Relaxation of Hyperpolarized ^{129}Xe and ^{3}He

Equation 4.84 tells us that the inherent T_2 relaxation of ^{129}Xe and ^{3}He is obtained from one of the parameters of a two-parameter fit. The quality of the fit will thus determine the uncertainty in the inherent T_2 time. In addition, we need to examine the uncertainty associated with the data of Figures 4.21 and 4.22. Each data point in these plots was obtained from the least-square fit of the CPMG echo train (see Figure 4.13). Consequently, the uncertainty in the extracted T_2^{CMPG} time constant will contribute to the uncertainty in the data points of Figures 4.21 and 4.22. By shifting the data in the vicinity of $TE = 0$ for the amount of T_2^{CPMG} uncertainty we concluded that the uncertainty in the estimation of the inherent T_2 is between 3% and 6%.

The uncertainty of 6% is sufficient to explain the variation in the extrapolated T_2 times for the three sets of ^{129}Xe data, but it does not suffice to explain the 20% error in the ^{3}He data. We thus have to look at possible systematic errors.

There are many effects which can shorten the measured T_2^{CPMG} times. We mentioned some of them, such as the uncertainties in the calibration of the 180-degree pulses and the off-resonance effect due to the resistive heating of the magnet, in Sections 4.6.1 and 4.6.2. However, none of these possible sources of error should affect ^{3}He data more than ^{129}Xe. One major difference between ^{3}He and ^{129}Xe experiments was the temperature of the cell

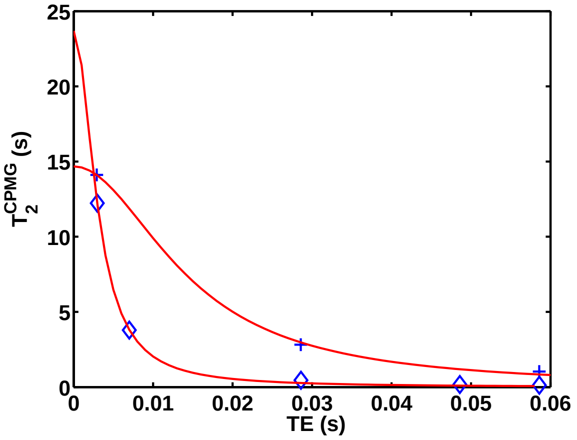

Figure 4.21: ^{3}He T_2^{CPMG} data as a function of interecho time, TE, for two shimming values, and a fit to the data according to Eq 4.84. $g \approx 0.06$ mT/m, $T_2 = 23.7$ s; $g \approx 0.01$ mT/m, $T_2 = 14.7$ s.

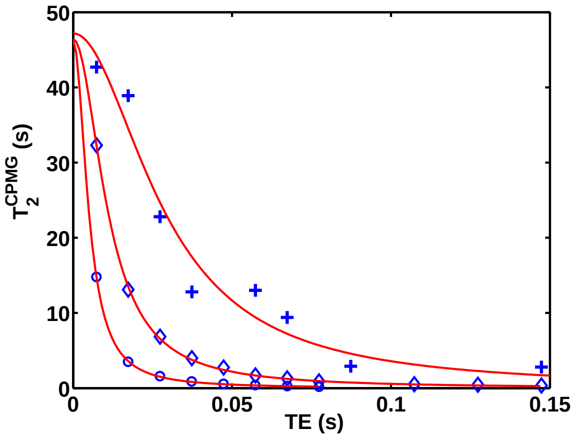

Figure 4.22: ^{129}Xe T_2^{CPMG} data as a function of interecho time, TE, for three shimming values, and a fit to the data according to Eq 4.84. $g \approx 0.02$ mT/m, $T_2 = 47.2$ s; $g \approx 0.13$ mT/m, $T_2 = 46.5$ s; $g \approx 0.38$ mT/m, $T_2 = 46.3$ s.

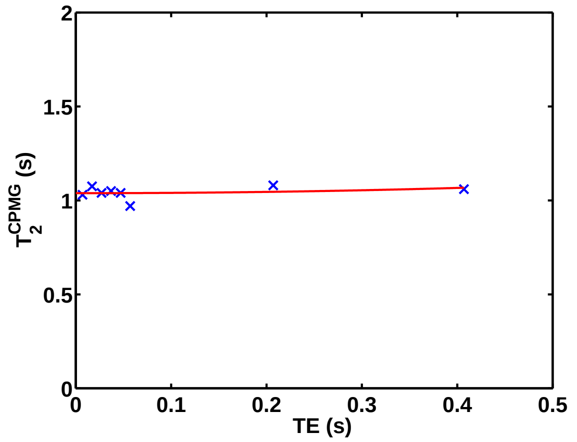

Figure 4.23: Distilled water T_2^{CPMG} data as a function of interecho time, TE, and a fit to the data according to Eq 4.84. $g = 0.005$ mT/m, $T_2 = 1.04$ s.

during optical pumping (120°C for ^{3}He vs. 80°C for ^{129}Xe). Since the signals were collected immediately after placing the cell into the low-field scanner for best SNR values, the ^{3}He cell might not have been in thermal equilibrium during data acquisition and the gas inside the cell might have been undergoing convective flow.

To understand how flow of gas inside the cell would decrease the echo magnitude and contribute to T_2^{CPMG} decay, we return to Eq. 4.40. The second term on the right hand side represents the phase shift of the echo in the presence of flow with velocity $\mathbf{v}$. Since no external gradients were applied during the CPMG sequence, the gradient $\mathbf{g}(t)$ in Eq. 4.40 will be due to the magnetic field inhomogeneities. For a constant background inhomogeneity of magnitude g, the time integral reduces to

$$\int_0^t \left(\int_0^{t'} g(t'')dt'' \right) dt' = -\frac{1}{4}\, g\, TE^2. \tag{4.87}$$

The second term in Eq. 4.40 thus becomes

$$\exp\left[i\gamma \mathbf{v} \cdot \int_0^t \left(\int_0^{t'} \mathbf{g}(\tau) d\tau \right) dt' \right] = \exp\left[-\frac{i}{4}\, \gamma\, \mathbf{v} \cdot \mathbf{g}\, TE^2 \right] \tag{4.88}$$

For ^{3}He, $\gamma = 32.43$ kHz/mT, g was on the order of 0.1 mT/m, and the shortest TE time was 7 ms.[15] In the worst-case scenario, $\mathbf{v} \cdot \mathbf{g} = v\, g$. For a 1-degree phase shift we have

$$\begin{aligned} \exp\left[-\frac{1}{4}\, \gamma\, v\, g\, TE^2 \right] &= \exp\left[-i \frac{\pi}{180} \right] \\ v &= 1 \text{ cm/s.} \end{aligned} \tag{4.89}$$

The result tells us that if the convective flow moves with velocity of 1 cm/s (a plausible assumption), each spin echo would be phase-shifted 1-degree from the previous one. This would violate the CPMG condition which requires that the axis of rotation remains parallel to the gas magnetization (see also Section 4.6.2) and result in an accelerated decay of spin echoes and a shorter T_2^{CPMG} time.

We tested our "flow" hypothesis by performing some simple tests. Table 4.3 gives an overview of these tests and the corresponding qualitative results. On the basis of the test results we were able to form the following conclusions: 1. Shaking the cell and so disturbing

---

[15] The error in T_2^{CPMG} of the echo train with the shortest TE time will weight the most in the evaluation of the error in T_2.

the gas inside the cell does indeed affect the quality of spin echoes and the rate of decay of the spin echo train; 2. In our *in vitro* experiments the effect of gas movement (due to shaking or high temperatures) subsides after 10-20 s, hence data acquisition should not begin before the gas had the time to reach thermal equilibrium; 3. Spin echoes decay faster if the cell is not at room temperature during data acquisition, although more studies (possibly with ^{3}He gas rather than ^{129}Xe) would have to be done to understand whether this effect is due to hyperpolarized gas relaxation resulting from collisions with unpolarized Rb vapor or due to the effects of gas flow.

In summary, we think that either shaking of the cell and/or not cooling the gas inside the cell to room temperature affected our T_2^{CPMG} data and thus contributed to the error in the inherent ^{3}He T_2 relaxation times. Evaluating the size of this systematic error would require a more detailed study. Alternatively, we could increase the statistics of ^{3}He data.

Finally, understanding the effects of flow on a CPMG spin echo train and the measured T_2^{CPMG} relaxation time would be essential in *in vivo* experiments, due to the motion (flow) of gas through the bronchi and lungs.

Flow Tests using Xe cell	Qualitative Results	
	Quality of Spin-Echo Train	Rate of Spin-Echo Decay
Shaking the cell vigorously before data acquisition	Poor	Fast
No shaking before data acquisition	Good	Slow
Shaking + waiting 10 sec before data acquisition	Good	Slow
No cooling of the cell before data acquisition	Bad	Fast
Cooling for 10 sec before data acquisition	Good	Fast
Cooling for 20 sec before data acquisition	Good	Slow

Table 4.3: Results of simple qualitative experiments testing the hypothesis of gas flow.

4.9 Conclusions

We have investigated the possibility of using a pulsed (or variable) rather than a static resistive system for low-field hyperpolarized gas imaging. In particular, the field instability at 397 kHz (i.e., 33 mT for ^{129}Xe) is small enough to allow the implementation of the CPMG spin echo sequence. We were able to collect ^{129}Xe CPMG spin echo trains lasting over 30 s and following a well behaved exponential decay. In addition, by adding a small offset field to the readout magnet, we guaranteed an adiabatic transition in magnetization alignment during the pulsing of the readout magnet and hence prevented loss of gas polarization.

We have developed a single-shot sequence for measuring diffusion coefficients of gases which separates diffusion losses from T_2^{CPMG} relaxation losses. Our diffusion sequence was a variation of the pulsed gradient spin echo sequence, with external gradients applied in the second half of the sequence only. For the binary mixture of hyperpolarized gas and nitrogen, the experimental values of ^{3}He, ^{129}Xe and water diffusion coefficients were: $D_{He3} = (1.69 \pm 0.17) \times 10^{-4}$ m^2/s, $D_{Xe129} = (1.28 \pm 0.13) \times 10^{-5}$ m^2/s, and $D_{H_2O} = (2.10 \pm 0.21) \times 10^{-9}$ m^2/s. The dominant experimental error was due to the uncertainty in the gradient strengths. This error could easily be reduced in the future by calibrating the gradient strengths more accurately. Finally, the experimental measurements agree well with the theoretical calculations of diffusion coefficients using Lennard-Jones [30] potentials.

Because diffusion coefficient is dependent on the cell pressure and gas composition, it is difficult to compare our data with the existing experimental data on diffusion coefficients. Schmidth *et al.* [80] measured a ^{3}He diffusion coefficient of 21.3 ± 0.4 mm^2/s at 7 atm of gas, which translates to $(1.491 \pm 0.028) \times 10^{-4}$ m^2/s at 1 atm of gas and agrees well with our measurement to within the uncertainty in the nitrogen pressure used in their experiment. Peled *et al.* [82] measured a ^{129}Xe diffusion coefficient of 0.0579×10^{-4} m^2/s, which is very close to our calculated ^{129}Xe self-diffusion coefficient (see Appendix A), so we conclude that their gas mixture had negligible amounts of nitrogen gas.

Finally, by varying the interecho time in the CPMG sequence we were able to determine the T_2 relaxation time at zero interecho spacing, which represents the inherent T_2 decay of hyperpolarized gas and is the upper limit on the time available for spin echo imaging. We measured an inherent ^{129}Xe T_2 relaxation of 46.7 ± 0.5 s, and an inherent ^{3}He T_2 relaxation of 19.2 ± 4.5 s. We hypothesize that the large error in the ^{3}He data might be due to the flow (motion) of gas inside the cell, which would result if the cell is not in thermal equilibrium during data acquisition or is shaken before being placed in the scanner.

Most of the T_2 values quoted in literature are the T_2^{CPMG} times which include diffusion losses in the background gradients. For instance, Pfeffer *et al.* [86] point out that their T_2 measurement was influenced by the field inhomogeneities so that the ^{129}Xe relaxation time of 12.9 ± 1.9 s was the lower limit on ^{129}Xe T_2 relaxation. Darrasse *et al.* [47] measured T_2^{CPMG} for ^{3}He in lungs at two different interecho times (10 ms, 30 ms) but did not use their measurements to find the inherent T_2 in lungs.

For future work, it would be interesting to see whether our method for determining the inherent T_2 times would be applicable to *in vivo* experiments. When imaging lungs, the effect of gas flow on the T_2 measurements would need to be studied in detail. However, such a study requires a full body scanner.

Chapter 5

Hyperpolarized Gas Imaging on a Low-Field Pulsed Resistive System

5.1 Background

MR imaging with hyperpolarized helium and xenon is an alternative to conventional proton MR imaging, especially for imaging void spaces, such as lungs [16, 39, 9] and colon [87], which contain no water. Initially, most of the hyperpolarized gas imaging was done on commercially available middle and high field scanners [16, 40, 43, 11, 88], mainly because of the availability to the MRI community. However, in Chapter 3.2.3 we show that the SNR of hyperpolarized gas is independent of the imaging field strength once the body becomes the dominant source of noise (so-called “body-noise dominance”) [22, 23, 21, 20]. Since the transition from coil-noise to body-noise dominance occurs at about 1 MHz (23.5 mT) for human torsos and 4 MHz (94 mT) for heads [20], hyperpolarized gas MR can be performed at low-field with no loss in the SNR of the image.

Low-field imaging offers important advantages over the high-field imaging. The low-field MR system is straightforward and inexpensive to build, since a homogeneous magnetic field can be produced with a homogeneous wire-wound electromagnets and the low Larmor frequencies reduce RF power requirements and allow the use of commonly available electronic components. The low-field systems are easy to site as they do not require specialized accommodations, such as a shielded room or cryogenic cooling of the magnet [21]. One of the biggest advantages of low-field MRI is the reduced susceptibility differences in heterogeneous samples and reduced static field inhomogeneities at low-field, which can cause significant distortions and signal loss at high-field strengths.

Low-field imaging of hyperpolarized gas has been performed mainly with static electromagnets [21, 47, 71, 72, 89, 26, 90]. Some attempts have also been made to image hyperpolarized gases with SQUIDS [91]. However, there are several advantages in using a pulsed, rather than a static resistive system. A pulsed magnet is lighter than the permanent magnet and it can be designed to produce practically no eddy currents which can distort the image. Another important advantage is that the pulsed electromagnet allows for the adjustment of the current strength and so eliminates the need to retune the RF coils for imaging different species (^{129}Xe, ^{3}He, water, fluoride). Because of the low duty-cycle, pulse mode power supplies are ideally suited to the brief imaging window of hyperpolarized gas MRI, especially when used in conjunction with single-shot techniques, such as RARE and trueFISP. Finally, a pulsed MR scanner is compatible with prepolarized proton MRI [25, 24] (see Chapter 3), and would therefore enable hyperpolarized gas as well as proton MRI on a single low-field scanner [92].

In addition to the many advantages offered by the pulsed resistive low-field MRI scanner, the system also presents several challenges. As discussed in Chapter 3, the readout field must be temporally and spatially stable to better than 100 ppm. There are several possible sources of field instability. First, the magnetic field could vary as a result of power supply instability. This problem was solved by using high-precision electronic components. Second, the strength of the magnetic field at the position of the sample changes due to the resistive heating of the copper wires which expand slightly outward from the center of the magnet bore. ^{129}Xe and ^{3}He T_2^{CPMG} measurements described in Section 4.6 produced spin echo trains containing 4096 echoes and lasting tens of seconds which demonstrated that the resistive heating of the magnet coils had negligible effect on the temporal stability of the magnetic field at low magnetic field strengths (frequency of 397 kHz). Another challenge was to investigate the effect of field-switching on the hyperpolarization of the noble gas, especially since there has been minimal research done in this area. We anticipated that the field-switching might destroy some or all of the gas hyperpolarization due to nonadiabatic changes in the alignment of the gas magnetization, between the direction parallel to the readout field and the direction parallel to the Earth's field. The experiments described in Chapter 4.5.2 confirmed the need for hardware and software adjustments to the pulsed resistive MRI scanner.

The experiments presented in the previous chapter established the possibility of using a pulsed low-field resistive system for hyperpolarized gas imaging. They also helped us to determine two important parameters–the diffusion coefficient and the T_2 relaxation time of hyperpolarized ^{129}Xe and ^{3}He–both of which make hyperpolarized gas imaging very different from proton imaging. In this chapter we will examine how these parameters affect the design of pulse-sequences used in imaging hyperpolarized gases. In particular, we will try to focus on two issues: 1. How to make best use of the nonrenewable hyperpolarization of the noble gas; 2. How to minimize the large diffusion of hyperpolarized gases. To answer these questions we will develop a model of signal decay during gradient echo and spin echo imaging. We will show that the hyperpolarized gas signal is best utilized using a CPMG spin echo sequence (also called RARE) while diffusion is minimized by first collecting the low k-values using centrally ordered phase-encode gradients. Consequently, the sequence that satisfies both requirements is a RARE sequence with centrally ordered phase-encode gradients.

5.2 Basic Principles of MR Imaging

In Section 3.2.1 we derived the MR signal equation (see Eqs. 3.1 and 3.5). We would now like to build upon this equation to show how imaging of the nuclear spin density can be performed using imaging gradients.

Ignoring the strength of the field generated by the transmit coil (B_1) and the flux though the receiver coil ($\propto i\omega_\circ$), the MR signal is the sum of magnetic moments throughout the imaging volume,

$$s(t) = \int_V M(x, y, z)\, dV. \tag{5.1}$$

The magnetic moments have magnitude, $M_\circ$, and phase, ϕ, so that

$$s(t) = \int_x \int_y \int_z M_\circ(x, y, z) e^{-i\phi(x,y,z,t)}\, dx\, dy\, dz. \tag{5.2}$$

If imaging is slice-selective, we can immediately integrate over the z-coordinate and define the magnetization in a slice of thickness Δz, centered around $z_\circ$, as

$$m(x, y) \equiv \int_{z_\circ-\delta z/2}^{z_\circ+\delta z/2} M_\circ(x, y, z) e^{-i\phi(x,y,z,t)}\, dz. \tag{5.3}$$

The phase of the magnetic moment can be expressed from the Larmor relationship as

$$\phi(t) = \gamma \int_0^t B(x, y, \tau)\, d\tau, \tag{5.4}$$

where the magnetic field is a sum of the static magnetic field and the imaging gradients, $B(x, y, \tau) = B_\circ + \mathbf{G} \cdot \mathbf{r}$; while the magnetization magnitude decays due to T_2 relaxation, $m(x, y) = m_\circ(x, y) \exp(-t/T_2)$. Therefore,

$$s(t) = \int_x \int_y m_\circ(x, y) e^{(-t/T_2)} e^{-i\omega_\circ t} e^{-i\gamma \int_0^t (\mathbf{G}(\tau)\cdot\mathbf{r}) d\tau}\, dx\, dy. \tag{5.5}$$

To simplify the present analysis, we will ignore the T_2 relaxation for the moment. Furthermore, the $\exp(-i\omega_\circ t)$ term can be dropped since the detection apparatus demodulates the carrier frequency by multiplying the received signal by $\exp(+i\omega_\circ t)$. The remaining term contains the imaging gradients which are central to our discussion:

$$s(t) = \int_x \int_y m_\circ(x,y) exp\Big\{ -i\gamma \int_0^t [G_x(\tau)x + G_y(\tau)y]\ d\tau \Big\}\ dx\ dy. \tag{5.6}$$

Equation 5.6 tells us that the imaging gradients control the phase of the precessing magnetization. We can express the gradients in terms of the spatial frequency vector, **k**:

$$\begin{aligned} k_x &\equiv \frac{\gamma}{2\pi} \int_0^t G_x(\tau)\ d\tau \\ k_y &\equiv \frac{\gamma}{2\pi} \int_0^t G_y(\tau)\ d\tau. \end{aligned} \tag{5.7}$$

The MR signal is thus

$$s(t) = \int_x \int_y m_\circ(x,y) e^{-i2\pi[k_x(t)x + k_y(t)y]}\ dx\ dy, \tag{5.8}$$

where $s(t)$ can be viewed as the sampling of trajectories of $k_x(t)$ and $k_y(t)$. From this last representation of the MR signal equation, we can clearly see that the detected MR signal is the two dimensional Fourier transform (2DFT) of the spin density distribution:

$$s(t) = F_{2D}\{m(x,y)\}. \tag{5.9}$$

This is an important result of MRI physics. It means that the imaging problem is reduced to acquiring the signal $s(t)$ at a range of values (k_x, k_y) and then inverting Eq. 5.8 using the inverse Fourier transform function (2DFT^{-1}).

There are many possible ways of sampling the k-space, each with its own advantages and uses, but the one that is most readily applicable to 2DFT is the Cartesian sampling of k-space, shown in Figure 5.1. Equation 5.7 tells us that the different k-values can be accessed by either changing the size of the imaging gradient or by changing the upper limit of the time integral. The former method is used for phase-encoding along the y-direction (also called the phase-encode direction), while the later method is used for encoding along the x-direction (also called the readout direction). Consequently,

$$\Delta k_x = \frac{\gamma}{2\pi} G_x\ \Delta t \tag{5.10}$$

$$\Delta k_y = \frac{\gamma}{2\pi} \Delta G_y\ t_{Gy}. \tag{5.11}$$

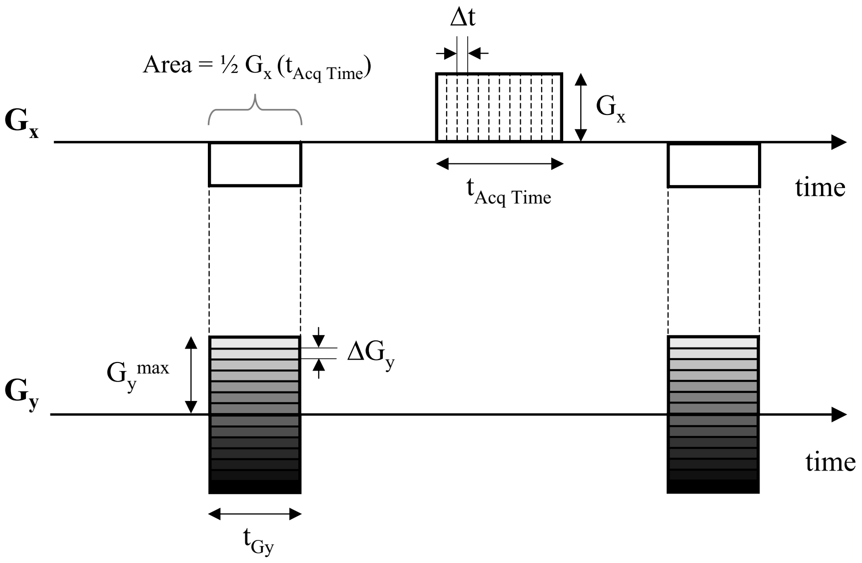

Figure 5.1: A typical gradient waveform used for collecting k-space data. Data acquisition occurs during the application of the positive G_x lobe. The magnitude of G_y is decremented with each excitation, while the magnitude of G_x is kept constant.

The k-space trajectory is described in Figure 5.2. The x and y-gradients turn on simultaneously for a time Δt_{Gy}, and the k-space trajectory moves to the point

$$k_{x,1} = -\frac{\gamma}{2\pi}\,\frac{1}{2} G_x\, t_{Acq.\,Time},\;\; k_{y,1} = \frac{\gamma}{2\pi}\, G_y^{max}\, t_{Gy}.$$

Once the y-gradient is turned off, the signal is read out in the presence of a constant x-gradient of amplitude G_x and duration $t_{Acq\,Time}$. The k-space trajectory moves along a constant k_y axis to the point

$$k_{x,2} = -k_{x,1},\;\; k_{y,2} = k_{y,1}.$$

On subsequent excitations, the amplitude of the y-gradient lobe is decremented (or incremented) while the x-gradient remains the same. This way, a new line of k-space is sampled after each excitation. Eventually, a sufficient amount of 2-D transform space is sampled to perform an inverse 2-D Fourier transform in order to reconstruct the object space, $m(x, y)$.

The study of pulse-sequence design examines ways in which k-space could be traversed

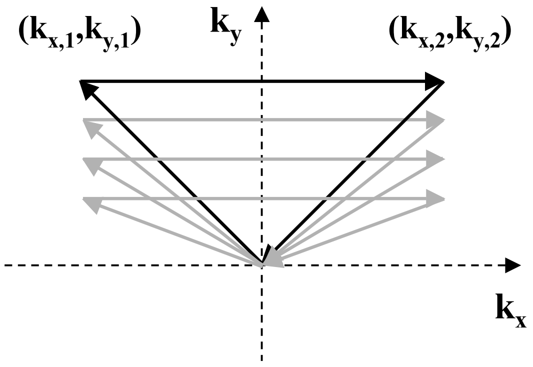

Figure 5.2: A schematic representation of k-space data collection. A line of k-space is acquired during each data acquisition; multiple acquisitions with varying k_y values are required to scan the entire plane.

so as to minimize imaging artifacts while maximizing the SNR and resolution of the image. In this work we will focus on two standard imaging sequences–the gradient echo and spin echo sequence.

5.3 Theoretical Model of Signal Decay during Hyperpolarized Gas Imaging

The estimation of T_2 relaxation and diffusion coefficients of hyperpolarized gases presented in Chapter 4 enables us to model the amount of signal decay during an imaging sequence. We can divide the effects which decrease the size of hyperpolarized gas signal into three groups: the effect of the excitation flip-angle; T_1 and T_2 relaxation losses; and diffusion-induced losses. We now examine each one of these effects in more detail.

5.3.1 Flip-Angle Effect

Since the signal detected in the receiver coil is due to the precession of the *transverse* magnetization, we need to estimate the projection of the longitudinal magnetization vector onto the transverse axis after each excitation. If a flip-angle α is used for each excitation, then the longitudinal components before and the transverse components after the first, second, and the nth excitations (where $n = 1, 2, ..., N$) are, respectively (see Figure 5.3),

$$\begin{aligned} m_{z,0} &= m_\circ, & m_{xy,1} &= m_\circ(\sin\alpha), \\ m_{z,1} &= m_\circ(\cos\alpha), & m_{xy,2} &= m_\circ(\cos\alpha)(\sin\alpha), \\ m_{z,n-1} &= m_\circ(\cos^{n-1}\alpha), & m_{xy,n} &= m_\circ(\cos^{n-1}\alpha)(\sin\alpha). \end{aligned} \tag{5.12}$$

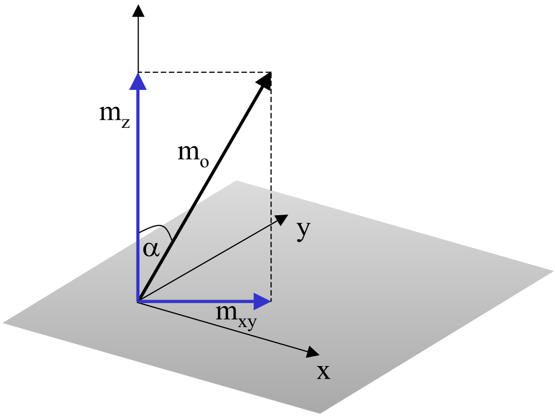

Figure 5.3: Projection of magnetization onto the longitudinal and transverse axis.

If a 90-degree flip-angle is used, then $m_{xy,1} = m_\circ$ and $m_{xy,2} = m_{xy,n} = 0$. In other words, because of the nonrenewable nature of the gas polarization, there can be no further excitations after the entire gas magnetization has been tipped into the transverse plane. In contrast, proton imaging allows the use of multiple 90-degree excitations, provided the time between the excitations is sufficiently long for the build-up of the longitudinal thermal proton magnetization.

The transverse magnetization after the nth excitation replaces the $m_\circ(x, y)$ term in Eq. 5.8, so that the NMR signal is

$$\begin{aligned} s(t) &= \int_x \int_y m_\circ \cos^{n-1}\alpha \, \sin\alpha \; e^{-i2\pi[k_x(t)x + k_y(t)y]} \, dx \, dy \\ &= \cos^{n-1}\alpha \, \sin\alpha \int_x \int_y m_\circ \, e^{-i2\pi[k_x(t)x + k_y(t)y]} \, dx \, dy \\ &= s_\circ(t) \left\{ \cos^{n-1}\alpha \, \sin\alpha \right\}, \end{aligned} \tag{5.13}$$

where $s_\circ(t)$ is

$$s_\circ(t) = \int_x \int_y m_\circ \, e^{-i2\pi[k_x(t)x + k_y(t)y]} \, dx \, dy, \tag{5.14}$$

while the term in the brackets is the weighting (scaling) function representing the effect of the RF flip-angle. The expression above assumes that the flip-angle α is homogeneous across the sample (i.e., is independent of x and y-coordinates) so that the cosine and sine terms can be pulled out of the integral. This assumption is correct only if the sample is smaller than the region of homogeneity of the RF coils. If this is not the case, the above expression is at best an approximation. The weighting function can be manipulated by variable flip-angles to achieve equal weighting of k-space lines [93].

5.3.2 Signal Decay due to T_1 and T_2 Relaxation

Signal loss is also caused by the relaxation mechanisms. According to Bloch equations [59], the transverse signal decays with a time constant T_2, while the longitudinal signal of the hyperpolarized gas decays with the time constant T_1 towards its thermal equilibrium.[1] Equation 5.12 tells us that in the absence of any relaxation, the transverse magnetization

---

[1] The T_1 relaxation represents the relaxation of the longitudinal magnetization component towards the thermal polarization levels along the z-axis. Therefore, in the case of *hyperpolarized* gases with polarization levels well above the thermal equilibrium, the T_1 relaxation represents the *decay* of hyperpolarization, while for *water*, T_1 relaxation represents the *growth* of magnetization along the longitudinal axis.

after the nth excitation, $m_{xy,n}$, can be expressed in terms of the longitudinal component before the nth excitation, $m_{z,n-1}$, as $m_{xy,n} = m_{z,n-1} \sin\alpha$. Scaling the transverse magnetization by the transverse relaxation, $\exp(-t/T_2)$, and the longitudinal magnetization by the longitudinal relaxation, $\exp(-t/T_1)$, we get

$$\begin{aligned} m_{xy,n} \exp(-\frac{t_2}{T_2}) &= m_{z,n-1}\ \sin\alpha\ \exp(-\frac{t_1}{T_1}) \exp(-\frac{t_2}{T_2}) \\ &= m_\circ\ \cos^{n-1}\alpha\ \sin\alpha\ \exp(-\frac{t_1}{T_1}) \exp(-\frac{t_2}{T_2}), \end{aligned} \tag{5.15}$$

where t_1 is the time elapsed from the first to the nth RF excitation and could be on the order of seconds, while t_2 is the time since the nth RF excitation and is usually on the order of milliseconds.

The NMR signal can again be obtained from Eq. 5.8, by replacing the $m_\circ$ term with the final expression in Eq. 5.15, so that

$$\begin{aligned} s(t) &= \int_x \int_y m_\circ\ \cos^{n-1}\alpha\ \sin\alpha\ e^{-t_1/T_1}\ e^{-t_2/T_2}\ e^{-i2\pi[k_x(t)x+k_y(t)y]}\ dx\ dy \\ &= s_\circ(t) \left\{\cos^{n-1}\alpha\ \sin\alpha\right\} \left\{e^{-t_1/T_1}\ e^{-t_2/T_2}\right\}, \end{aligned} \tag{5.16}$$

where we again assumed that the flip-angle and the relaxation rates do not change across the sample. Comparing Eq. 5.16 with Eq. 5.13 we can conclude that the exponential term in Eq. 5.16 is the contribution of T_1 and T_2 relaxation to signal loss.

When using the CPMG spin echo imaging sequence, we will only be concerned with the transverse relaxation time constant since the magnetization is constantly in the transverse axis during imaging. In particular, the T_2 relaxation should be replaced with the T_2^{CPMG} relaxation time, because the imaging sequences were acquired in the presence of background gradients (see Section 4.3 for more details). On the other hand, when using the gradient echo imaging sequence, T_2 relaxation time should be replaced with T_2^* time constant to include signal decay due to gradient inhomogeneities. In addition, when imaging ^{3}He, T_1 decay can be ignored, since the T_1 relaxation times of ^{3}He are on the order of hours, while the imaging time is on the order of seconds.

5.3.3 Signal Decay due to Diffusion

In Section 4.4.1 (Eqs. 4.41 and 4.42) we derived an expression for signal decay due to diffusion in an arbitrary gradient form $\mathbf{g}(\tau)$,

$$\exp\left[-D\gamma^2 \int_0^t \left(\int_0^{t'} \mathbf{g}(\tau)d\tau\right)^2 dt'\right] = \exp\left[-4\pi^2 D \int_0^t \left(k_x^2(t') + k_y^2(t')\right) dt'\right], \tag{5.17}$$

where D is the diffusion coefficient. Since the gradient waveform is known from the pulse sequence used in the imaging experiments and the diffusion coefficients of hyperpolarized ^{129}Xe and ^{3}He have been estimated in Section 4.7, we can use Eq. 5.17 to model diffusion losses as a function of imaging time.

The NMR signal in the presence of diffusion losses is

$$\begin{aligned} s(t) &= \int_x \int_y m_\circ \, e^{-4\pi^2 D \int_0^t [k_x^2(t')+k_y^2(t')]dt'} \, e^{-i2\pi[k_x(t)x+k_y(t)y]} \, dx \, dy \\ &= s_\circ(t) \left\{ e^{-4\pi^2 D \int_0^t [k_x^2(t')+k_y^2(t')]dt'} \right\}, \end{aligned} \tag{5.18}$$

where again we were able to pull the diffusion term out of the integral because the gradient waveform is assumed to be uniform across the sample (i.e., G_x and G_y have no spatial dependence).

5.3.4 K-Space Weighting

Knowing the various processes that contribute to MR signal decay we are now able to construct so-called *"k-space weighting"* which modulates (weights or scales) the MR time-domain data.

In all the imaging experiments, the object imaged was a sphere, 2.5 cm in diameter, filled with either hyperpolarized ^{129}Xe, ^{3}He or water. Since no gradients were applied along the z-axis, the imaging was slice non-selective. This meant that we were imaging the projection of a sphere onto a plane orthogonal to the z-axis, which was a circle of varying signal intensity. The intensity is greatest at the center of the circle, since it corresponds to the projection through the center of the sphere, and falls off to zero at the sphere's borders.

Because data acquisition happens in time (or k-space) domain, we have to consider the Fourier transform of a circle–which is a jinc function (see Figure 5.5). However, since k-

space signal is subjected to the decay processes described in the previous section, the jinc function has to be scaled by a function describing the amount of signal decay along the readout (x) and phase-encode (y) directions. We call such a scaling function the "k-space weighting". The k-space weighting can easily be constructed once we are able to evaluate all the scaling terms from Eqs. 5.13, 5.16, and 5.18 pertaining to a particular pulse sequence. For a general case, the k-space weighting w is

$$w(t) = \left\{\cos^{n-1}\alpha\sin\alpha\right\} \left\{e^{-t_1/T_1} e^{-t_2/T_2}\right\} \left\{e^{-4\pi^2 D \int_0^t \left[k_x^2(t')+k_y^2(t')\right]dt'}\right\}. \tag{5.19}$$

The product of the jinc and w functions is then transformed into the image domain using 2-D inverse Fourier transform. The result, when displayed in the image mode as in Figure 5.5, is a circle that has been convolved with the inverse Fourier transform of the k-space weighting function.[2] The entire procedure is schematically illustrated in Figures 5.5 and 5.4.

The procedure described above served as a the basis for a Matlab simulation which modelled signal decay given specific pulse-sequence parameters (see Appendix C) and resulted in a weighted (scaled) projection of a sphere in both, k-space and object-space domains.

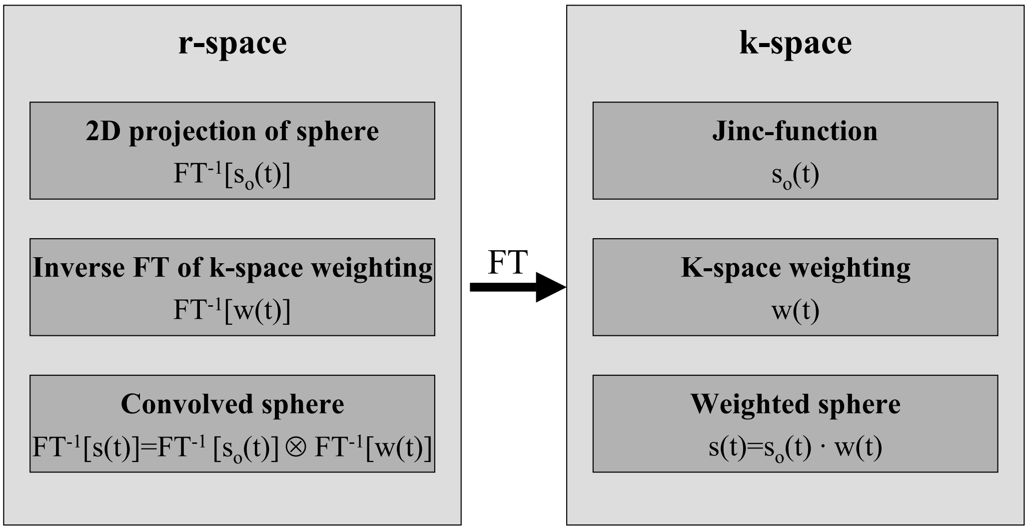

Figure 5.4: Overview of r-space and k-space functions used in modelling the effects of signal decay on the image of a 2-D sphere.

---

[2] According to the theorem of Fourier transforms [94], multiplication of two functions in the k-space domain is equivalent to the convolution of the inverse Fourier transforms of the functions in the image domain.

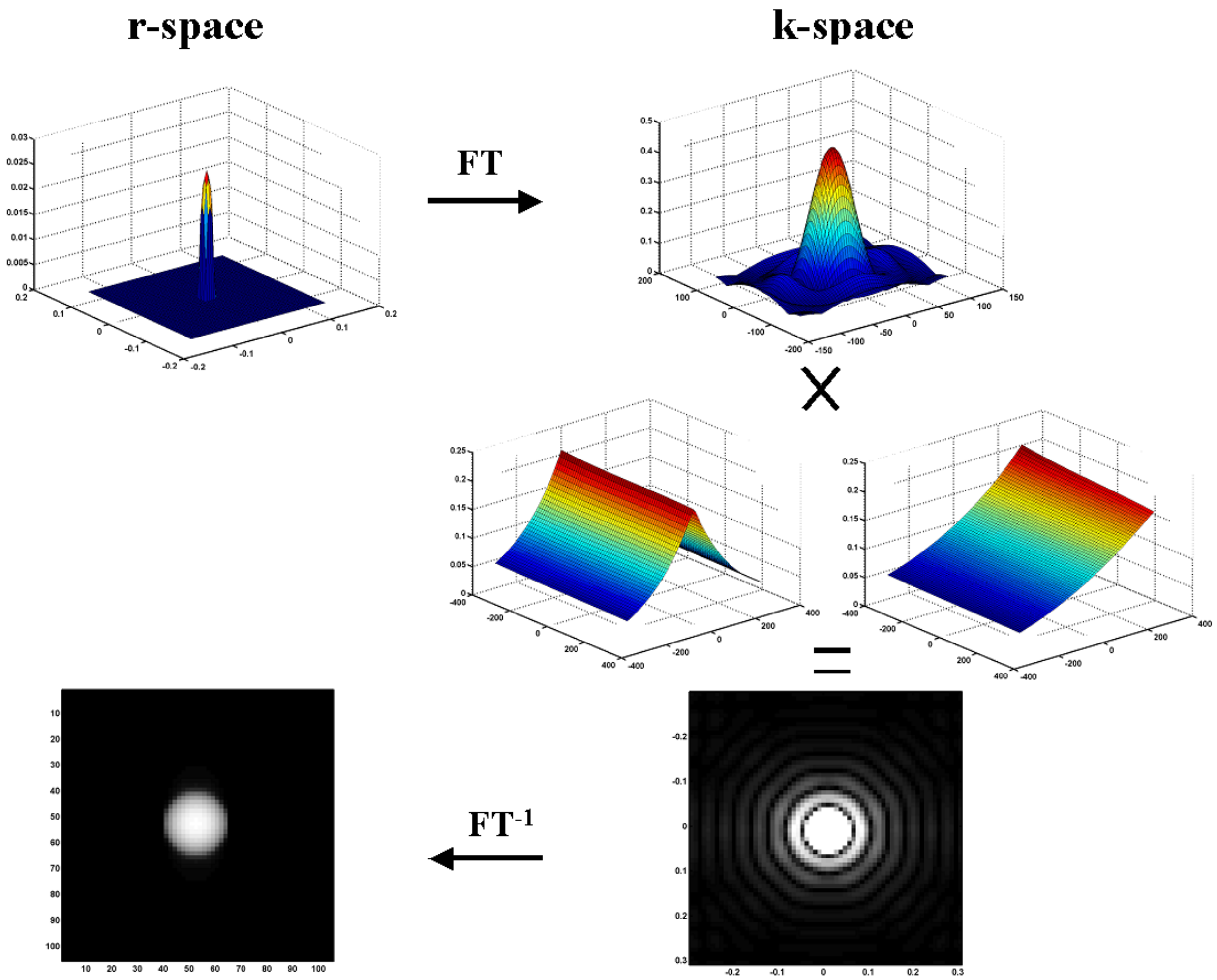

Figure 5.5: Schematic representation of the model used to obtain the effect of diffusion, relaxation and finite flip-angle on the image. Top left: projection of a sphere onto the z-axis. Top right: Fourier transform of the sphere's projection–the jinc-function. Middle right: k-space weighting for centric (l) and sequential (r) encoding schemes. Bottom right: weighted projection of a sphere in k-space displayed in image mode. Bottom left: weighted projection of a sphere in r-space displayed in image mode.

5.4 Gradient Echo Imaging

5.4.1 Gradient Echo Pulse Sequence

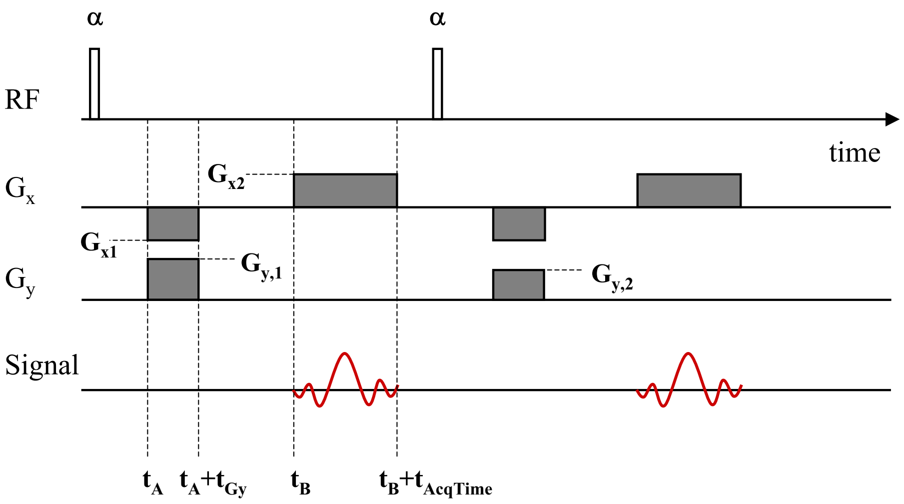

Figure 5.6: Pulse sequence used in gradient echo imaging. RF = excitation pulse, α = flip-angle, G_x = gradient waveform along x-direction, G_y = gradient waveform along y-direction, Signal = gradient echo.

Figure 5.6 shows a typical gradient echo pulse sequence. First, an RF pulse tips (or flips) the magnetization an angle α away from the z-axis. Then, imaging gradients G_x and G_y are applied. In general, when a gradient $\mathbf{G}$ is applied, spins at position $\mathbf{x}$ acquire a phase ϕ equal to

$$\begin{aligned}\phi(t) &= \gamma \int_0^t [\mathbf{G}(\tau) \cdot \mathbf{x}]\, d\tau = \gamma x \int_0^t G_x(\tau)\, d\tau + \gamma y \int_0^t G_y(\tau)\, d\tau \\ &= 2\pi k_x(t) x + 2\pi k_y(t) y, \end{aligned} \tag{5.20}$$

where in the last step we used Eq. 5.7. The above equation also tells us that the phase of the spins is proportional to the cumulative area $\int_0^t G(\tau) d\tau$ under a gradient waveform. Hence,

$$\phi(t) = \gamma x A(t)_{G_x} + \gamma y A(t)_{G_y}. \tag{5.21}$$

When the cumulative area under the gradient waveform–$A(t)_{G_x}$ or $A(t)_{G_y}$–is non-zero, the spins at different (x,y) locations accumulate a different amount of phase. The result is spin de-phasing. However, by detecting the amount of spin-incoherence at different spatial locations, the spatial distribution (i.e, density) of spins can be mapped out. This is the image-domain perspective to position-encoding.[3] As the cumulative area under the gradient waveform reaches zero, the spins at different locations re-phase (i.e., $\phi(t)$ in Eq. 5.21 is zero for all values of x and/or y). The re-phasing of spins results in an echo. In other words, the coherence of spins, which has been lost during the application of position-encoding gradients, has been restored. Therefore, a gradient echo is produced whenever the cumulative area under the readout gradient G_x reaches zero. It is instructive to compare the occurrence of a gradient echo with the occurrence of a spin echo. In the spin echo case, the 180-degree pulses reverse the polarity of the gradients due to the static field inhomogeneities (i.e., *internal* gradients) halfway between the excitation and the middle of acquisition (time TE in Figure 4.11). The spin echo occurs when the cumulative area under these internal gradients reaches zero–exactly in the middle of the acquisition.

The basic principle behind the gradient and spin echoes is thus the same: gradient echoes as well as spin echoes occur when the cumulative area under a gradient waveform is zero (and therefore, $k = 0$). The difference is that in the case of spin echoes, it is the area under the *internal* gradient waveform, while in the case of gradient echoes, it is the area under the *external* gradient waveform that counts.

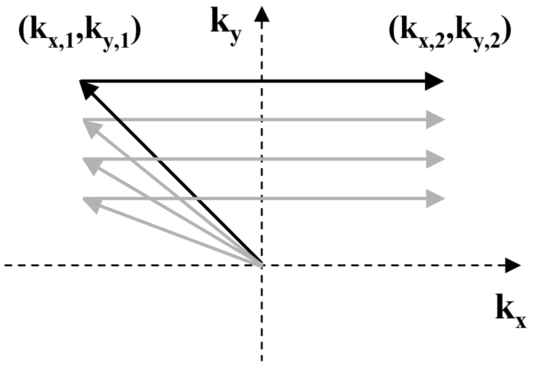

Figure 5.7: A schematic representation of k-space data collection in gradient echo sequence.

Figure 5.7 shows the k-space trajectory for the gradient echo sequence. Since each line of k-space is obtained with a “fresh” magnetization that has just been tipped away from the z-axis, we do not need to bring the k-vector back to zero (i.e., refocus the magnetization) after reading out a line of k-space.

---

[3] For the k-space perspective of position-encoding see Section 5.2.

5.4.2 *K*-Space Weighting for Gradient Echo Imaging

To construct k-space weighting for the gradient echo imaging sequence, we have to examine which processes contribute to signal decay along the readout and phase-encode directions, respectively. To study signal decay along the readout direction, we examine the k-space weighting in Eq. 5.19 (see also the pulse-sequence in Figure 5.6) at a fixed value of the phase-encode gradient (i.e., fixed y), or alternatively, after the nth excitation (at fixed n).

The nth excitation tips the magnetization an angle α away from the longitudinal axis. The projection of magnetization onto the transverse plane decays with with T_2^* relaxation constant. If the time between each excitation is TR, then the time up to the nth excitation is $t_1 = (n-1)TR$. Therefore, the k-space weighting after the nth excitation is

$$w(t) = \cos^{n-1}\alpha\ \sin\alpha\ \exp\left(-\frac{(n-1)TR}{T_1}\right)\ \exp\left(-\frac{t}{T_2^*}\right)\ \exp\left(-4\pi^2 D\int_0^t \left\{k_x^2(t') + k_y^2(t')\right\} dt\right). \tag{5.22}$$

Since we are concerned with signal decay during the acquisition period, the upper limit of the integration time t is $t_B < t < t_B + t_{AcqTime}$, where t_B is the time when the positive lobe of the readout gradient is turned on, while $t_B + t_{AcqTime}$ is the time when the positive lobe of the readout gradient is turned off (see Figure 5.6). If, in addition, we define the time when the phase-encode gradient lobe is turned on as t_A, and the time when it turned off as $t_A + t_{Gy}$, then we can solve the integrals in Eq. 5.22. For $t > t_B$,

$$\begin{aligned} w(t) \quad = \quad & \cos^{n-1}\alpha\ \sin\alpha\ \exp\left(-\frac{(n-1)TR}{T_1}\right)\ \exp\left(-\frac{t}{T_2^*}\right) \times \\ & \exp\left(-D\gamma^2\left\{-\frac{2}{3}\,t_{Gy}^3 G_{x1}^2 + t_{Gy}^2 G_{x1}^2(t-t_A) - t_{Gy}G_{x1}G_{x2}(t-t_B)^2 + \frac{1}{3}\,G_{x2}^2(t-t_B)^3\right\}\right) \times \\ & \exp\left(-D\gamma^2\left\{-\frac{2}{3}\,t_{Gy}^3 G_{y,n}^2 + t_{Gy}^2 G_{y,n}^2(t-t_A)\right\}\right), \end{aligned} \tag{5.23}$$

where G_{x1} is the amplitude of the negative lobe of the x-gradient, G_{x2} is the amplitude of the positive lobe of the readout gradient and $G_{y,n}$ is the amplitude of the phase-encode gradient after the nth excitation. For a constant n, both, the diffusion term in Eq. 5.23 and the T_2^* relaxation depend on the time of the acquisition, t.[4] Signal decay along the readout direction will thus be caused by diffusion in the x and y-gradients and by the T_2^* relaxation.

To study signal decay along the phase-encode direction, we need to consider Eq. 5.22 for

---

[4] The cosine term and the T_1 relaxation term are constant for a given n value.

two consecutive excitations, for instance, the nth and *(n+1)*th. Doing so, we can see that the signal along k_y changes as a result of the additional projection onto the transverse axis ($\cos^{n-1}\alpha$ vs. $\cos^{n}\alpha$); as a result of additional T_1 decay ($e^{-(n-1)TR/T_1}$ vs. e^{-nTR/T_1}); and as a result of a different G_y amplitude ($G_{y,n}$ vs. $G_{y,n+1}$). As already mentioned before, the T_1 decay can be neglected for ^{3}He since the T_1 relaxation time for ^{3}He is on the order of hours, while the total imaging time is on the order of a minute. Therefore, it is a combination of the flip-angle effect and diffusion losses in the y-gradients that contribute to the changes along the phase-encode direction.

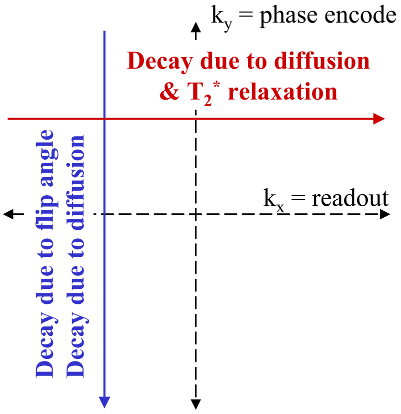

Figure 5.8: Schematic representation of signal decay during gradient echo sequence. Diffusion and T_2^* relaxation cause signal loss along the readout direction, while flip-angle and diffusion cause signal loss along the phase-encode direction.

Figure 5.8 summarizes, schematically, the processes which contribute to signal decay along the readout and phase-encode directions during gradient echo imaging of ^{3}He. As discussed above, diffusion and T_2^* relaxation affect the loss of signal along the readout direction (at constant n value), while diffusion and the size of the flip-angle affect the signal loss along the phase-encode direction.

5.4.3 2-D Gradient Echo Imaging Experiments and Simulations

Figures 5.9 and 5.10 demonstrate experimentally and theoretically the effect of diffusion, T_2^* relaxation and flip-angle on signal loss along the k_x and k_y directions, respectively. The magnitude of the raw k-space data is displayed on top of the page, followed by the simulation of the two-dimensional k-space and the k-space weighting which were obtained using the imaging parameters from the experiments.

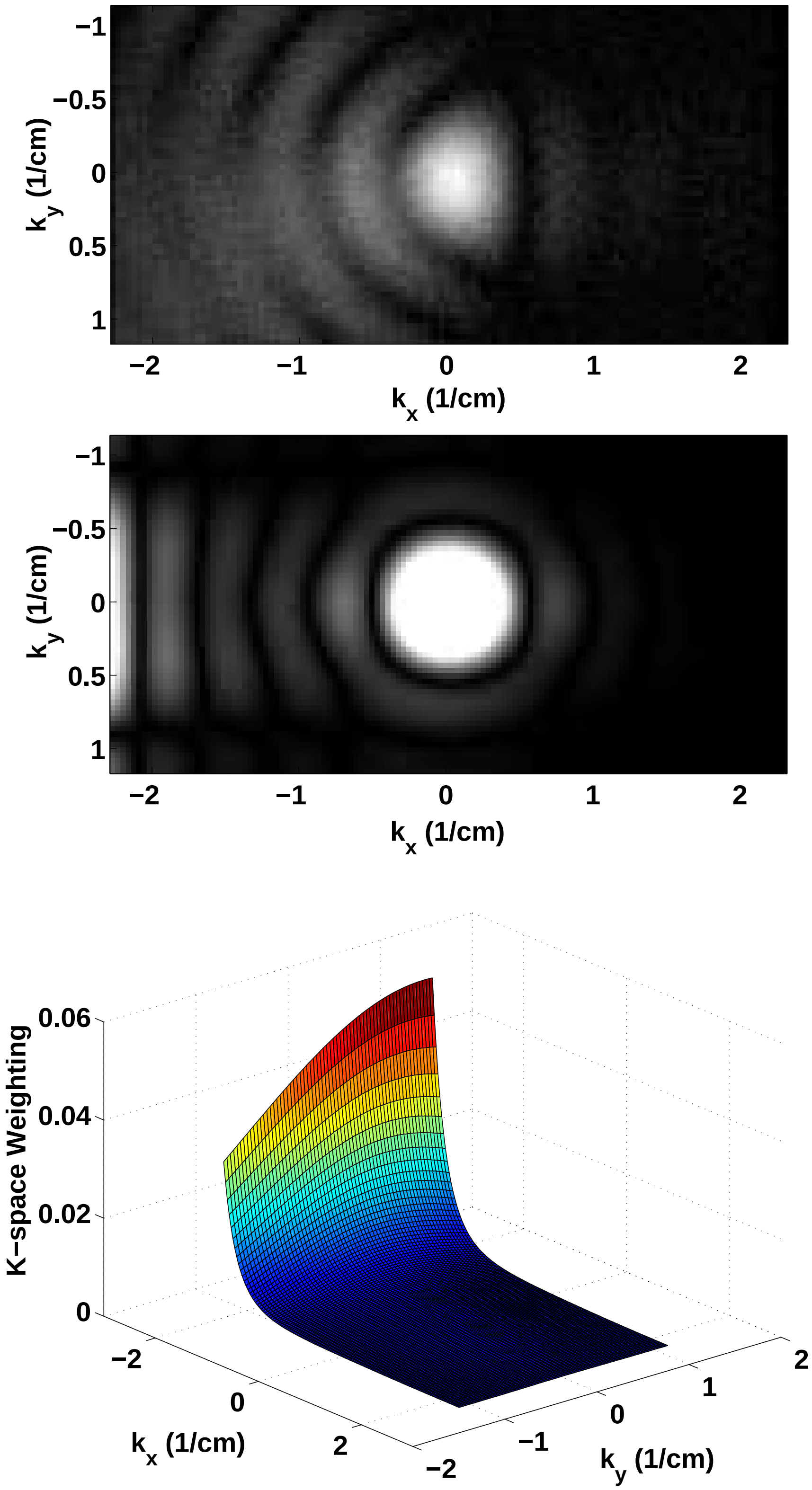

Figure 5.9: Diffusion and T_2^* losses along the readout direction. Top: Experimental raw k-space data. Middle: Simulation of k-space data. Bottom: K-space weighting used in the simulation. Acq.time=42.6 ms, BW=1502 Hz, $\alpha = 8°$, $FOV_x = FOV_y = 27.8$ cm, $\Delta x = 2.17$ mm, $\Delta y = 4.34$ mm, $T_2^* = 40$ ms, sequentially ordered phase-encode gradients.

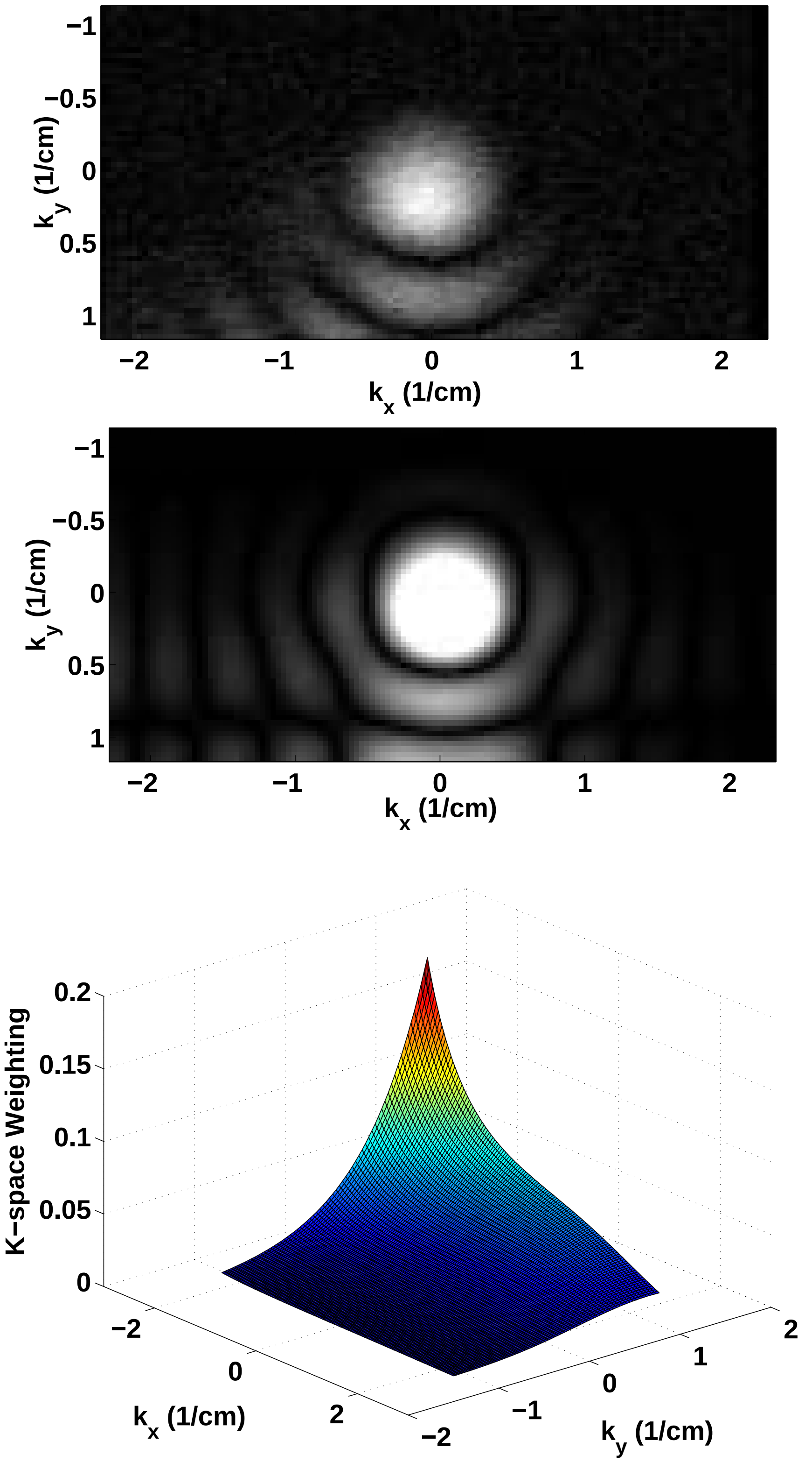

Figure 5.10: Flip-angle effects along the phase-encode direction. Top: Experimental raw k-space data. Middle: Simulation of k-space data. Bottom: K-space weighting used in the simulation. Acq.time=10.8 ms, BW=5952 Hz, $\alpha = 19.6°$, $FOV_x = FOV_y = 27.8$ cm, $\Delta x = 2.17$ mm, $\Delta y = 4.34$ mm, $T_2^* = 40$ ms, sequentially ordered phase-encode gradients.

To understand the appearance of partial concentric circles in the k-space data of Figures 5.9 and 5.10, we recall that the Fourier transform of a circle is a *jinc* function (see Figure 5.5) which is characterized by concentric circles spreading from the center ($k_x = 0,\ k_y = 0$) of k-space. In Figure 5.9, the intensity of concentric circles decreases from negative to positive k_x, which corresponds to the forward passage of time (see Eq. 5.10 as well as Figure 5.6). Such decay in signal intensity is indicative of excessive T_2^* relaxation and diffusion losses in the G_x gradient during the acquisition period. This can also be observed from the k-space weighting, which shows a large drop of relative NMR signal along the k_x direction. Ideally, we would like to minimize such asymmetric signal loss.

Similarly, the intensity of concentric circles in Figure 5.10 decreases from positive to negative k_y values (i.e., from the first to the last line of k-space scanned). However, in this case the loss of signal intensity must be attributed to flip-angle effects. In particular, if the flip-angle is too large, the magnetization could decay completely before the entire k-space plane is scanned. The flip-angle used to obtain the k-space data in Figure 5.10 was 19°, which turns out to be too large to utilize all the available magnetization in our gradient echo sequence the best way possible.[5] To see this, consider Eq. 5.13 for 64 phase-encoding steps ($n = 64$). To best utilize the available magnetization, we must *maximize* the SNR at the center of k-space while at the same time making sure not to run out of the magnetization before the end of the scan. The first condition is satisfied by looking for a maximum of the normalized signal $s(t, n, \alpha)/s_\circ(t)$ in Eq. 5.13 at $y = 0$, which corresponds to $n = 32$:

$$\begin{aligned}
\frac{d\left[s(t, n=32, \alpha)/s_\circ(t)\right]}{d\alpha} &= 0 = -31\cos^{30}\alpha\ \sin^2\alpha + \cos^{32}\alpha \\
\tan\alpha &= \sqrt{\frac{1}{31}} \\
\alpha &= 10.2^\circ. \qquad (5.24)
\end{aligned}$$

To satisfy the second condition we demand that we use 99% of gas polarization during the scan. Thus,

$$\begin{aligned}
\frac{s(t, n=64, \alpha)}{s_\circ(t)} &= \frac{s_\circ(t)\ \cos^{63}\alpha\ \sin\alpha}{s_\circ(t)} \approx 0.01 \\
\cos^{63}\alpha\ \sin\alpha &\approx 0.01 \\
\alpha &\approx 18.9^\circ. \qquad (5.25)
\end{aligned}$$

---

[5] Flip-angle calibration was done prior to imaging experiments by collecting FID data on a water sample (see also Section 4.6.1).

Therefore, for 64 phase-encoding steps, flip-angles around 15° offer a compromise between the need for maximum SNR in the middle of k-space and the need for optimal usage of the available magnetization. The calculations would need to be adjusted when using a different number of phase-encoding steps or a different encoding scheme.[6]

5.4.3.1 Centrally and Sequentially Ordered Phase-Encode Gradients during Gradient Echo Imaging

While the flip-angle can be optimized to provide uniform magnetization levels throughout the gradient echo imaging sequence [93], the diffusion losses (such as those in Figure 5.9) are, in principle, unavoidable. However, they can be minimized significantly by collecting low k-values prior to high k-values. Recall, that the diffusion loss is proportional to the cumulative path integral in k-space (see Eq. 5.17):

$$\ln \frac{s(t)}{s_\circ} = -4\pi^2 D \int_0^t \mathbf{k}^2(t')dt'. \tag{5.26}$$

Consequently, to reduce diffusion losses as much as possible, we would ultimately have to design a pulse sequence with a trajectory that starts at the origin of k-space and then spirals (or progresses) to the outer edges of k-space, such as the trajectories shown in Figure 5.11. However, we start by simply reorienting the phase-encode gradients in our gradient echo sequence. Instead of starting the scan of k-space at high k_y values where diffusion losses are large (Figure 5.12, right), we can start with the $k_y = 0$ line and then proceed with alternate scans on either side of the k-plane (Figure 5.12, left). This adjustment in the ordering of the phase-encode gradients is easy to implement into the pulse-sequence and does not require an elaborate algorithm during the image processing stage.

Figures 5.13 and 5.14 show, respectively, an image and a simulation of ^{3}He obtained using the gradient echo sequence with sequentially ordered phase-encode gradients (as displayed on the right side of the Figure 5.12). The x and y axes are the imaging axes in units of cm. The 2-D image of the sphere occupies a circular area with a diameter of about 2 cm, which is consistent with the size of the cell imaged ($r = 1.25$ cm). The vertical axis in both plots represents the intensity of the MR signal in arbitrary units.[7] The spike at the origin of

---

[6] For 128 phase-encoding steps, the ideal angle would be between 7.2° and 12.6°.

[7] The vertical scales of the image and simulation were not scaled against each other because the units used in the simulation represent the fraction of signal decay from the onset of imaging (i.e., when the

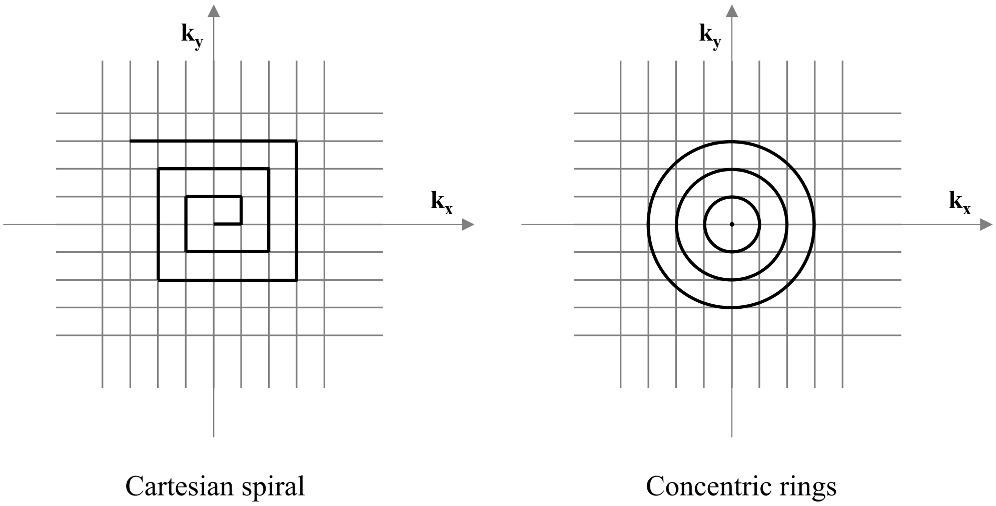

Figure 5.11: A schematic representation of k-space trajectories using a Cartesian spiral (left) and concentric circles (right) encoding scheme that can significantly reduce diffusion losses during imaging.

k-space is a DC signal, which results from a DC offset in any of the electronics components. It can be removed during signal processing.

Similarly, Figures 5.15 and 5.16 show, respectively, an image and a simulation of ^{3}He obtained using the gradient echo sequence with centrally ordered phase-encode gradients (as displayed on the left side of Figure 5.12). Both (central and sequential) gradient echo images were collected after 2 hours of optical pumping and using the same imaging parameters: the transmit-receive frequency of 397 kHz, a flip-angle of 15.5 degrees, resolution of 1.64 mm in x and y dimensions, field-of-view of 10.5 cm, acquisition time of 4 ms, receiver bandwidth of 8 kHz, G_x gradient equal to 4.7 mT/m and maximum G_y gradient value equal to 9.41 mT/m.

By comparing Figures 5.13 and 5.14 with Figures 5.15 and 5.16, we can determine the SNR gain in using centrally as opposed to sequentially ordered phase-encode gradients. To compare the SNR's in the actual data, we first notice that the noise levels in Figures 5.13 and 5.15 are approximately the same, with the average noise around 0.5 units. This is consistent with the fact that the same receiver bandwidth was used for both experiments.[8]

---

magnetization of the hyperpolarized gas was equal to 1), while the vertical scale in the experimental plots reflects the amount of voltage induced in the receiver coil during the scan. It would not be straightforward to normalize the detected voltage against the maximum voltage, in part due to the DC signal at the origin of k-space.

[8] As discussed in Section 3.2.2 on MRI noise properties, the amount of noise is proportional to the receiver bandwidth.

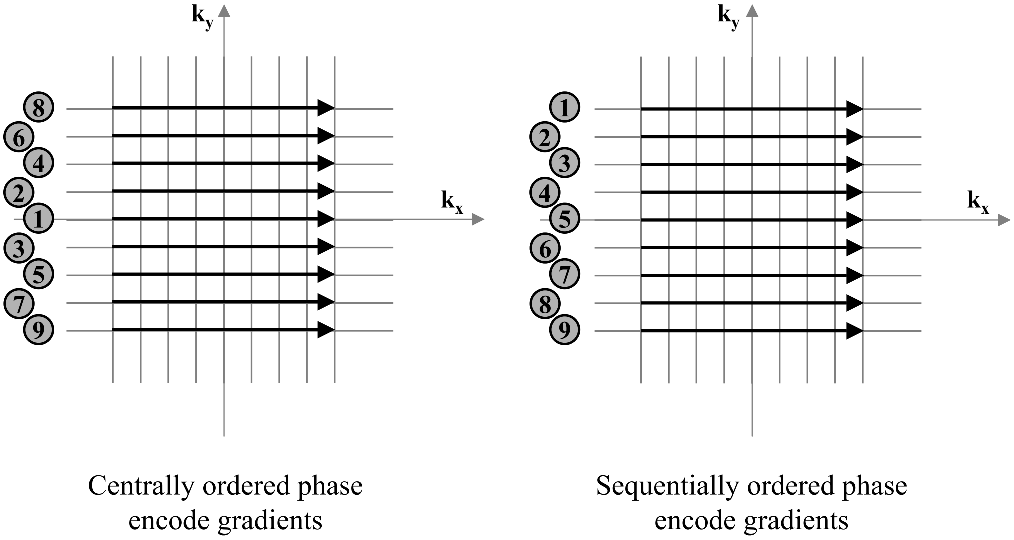

Figure 5.12: A schematic representation of centrally (left) and sequentially (right) ordered phase-encoding scheme using 2DFT sampling of k-space. By acquiring central phase-encodes first, diffusion losses are reduced.

To compare the signal levels, we would need to take the ratios of the volumes under the signal intensity function. However, to first order, we can approximate the ratio of the volumes with the ratios of the maximum signal intensity (ignoring the DC peak) because the projections onto the xy-plane are approximately the same for the two plots. Therefore, we have

$$\begin{aligned} SNR\ for\ sequentially\ ordered\ phase-encode\ gradients &\approx 17.4:1; \\ SNR\ for\ centrally\ ordered\ phase-encode\ gradients &\approx 4.4:1, \end{aligned}$$

and the SNR gain for gradient echo images obtained with centrally ordered phase-encode gradient is thus around 4.

Since the simulations do not model noise during the acquisition, we cannot estimate the SNR of the simulations. However, as demonstrated by the experimental data, the ordering of phase-encode gradients does not effect the noise level, which only depends on the receiver bandwidth. It thus suffices to compare the signal levels of the two simulations (Figure 5.13 and 5.16). The gain when using centrally ordered phase-encode gradient is approximately 3.

We can conclude that the actual data and simulation do agree to first order. The slight difference between experiment and simulation in the amount of signal gained using centrally ordered phase-encode gradient could be attributed to various factors. First, the simulation assumes that the levels of magnetization at the onset of imaging are the same for the two experiments (centric and sequential encoding schemes). However, even though we attempted to pump the ^{3}He cell the same amount of time in both experiments, and in addition, to take the same amount of time from the end of the pumping process to the start of imaging, the levels of polarization might have been slightly different in the two experiments (due, for instance, to differences in pumping temperature, the cell-cooling process, changes in the gradient shim values). One way to avoid this uncertainty in the future would be to collect an FID signal before imaging, using a small flip-angle to minimize magnetization loss. This FID signal would serve as a marker (or detector) of the polarization levels at the onset of imaging.

Another possible cause of the SNR gain difference could be the uncertainty in the flip-angle used in the experiment. Since uncertainty in the flip-angle is cumulative with the number of excitations (due to the factor $\cos^{n-1}\alpha$ in Eq. 5.12), it will have a disproportionably larger effect on the experiment with sequentially rather than centrally ordered phase-encode gradients since the center of k-space occurs at $n = 33$. For instance, a 16% error in the flip-angle ($15.5^\circ \pm 2.5^\circ$) would produce a 22% error in the maximum signal intensity at $k = 0$ for sequentially ordered phase-encode gradients, and consequently, the signal gain in the simulation would become 3.11 ± 0.9, which would account for the entire difference between simulation and experiment.

Finally, in future experiments, a crusher gradient could be added into the pulse sequence after the acquisition period to destroy the remaining transverse magnetization before "fresh" magnetization is tipped from the longitudinal axis [68]. This is necessary whenever $TR < T_2^*$–a condition that indicates that T_2^* relaxation processes have not destroyed the transverse magnetization by the end of the TR period. In the experiments of Figure 5.17, $TR \approx 110$ ms, while $T_2^* = 30 - 60$ ms, so the gas magnetization should have decayed significantly by the end of the TR period.

Figure 5.17 shows our best gradient echo image (left) and projection onto y-axis (right) of hyperpolarized ^{3}He taken with centrally ordered phase-encode gradients after 10 hours of optical pumping. It is instructive to compare the SNR of the gradient echo image of a cell filled with hyperpolarized ^{3}He with the SNR of the gradient echo image of the same-sized cell filled with water. Figure 5.18 shows a water gradient echo image (left) and projection (right) obtained with sequentially ordered phase-encode gradients.[9] Both hyperpolarized ^{3}He and water gradient images were collected at 398 kHz.

From the projections onto the y-axis, displayed on the right of Figures 5.17 and 5.18, we can see that the SNR of hyperpolarized ^{3}He is approximately 13, while the SNR for prepolarized water is 4. Hyperpolarized ^{3}He has thus a factor of approximately 3 higher SNR than prepolarized water when using a gradient echo sequence, 10 hours of optical pumping, and $B_p \approx 0.3$ T.

In conclusion, the gradient echo imaging of hyperpolarized gases is very straightforward to implement on the low-field pulsed resistive scanner once the flip-angle and the gradient waveform are chosen to provide a symmetric signal decay around the center of k-space. However, gradient echo imaging is an inefficient way of using the gas hyperpolarization due to the small flip-angles used for each excitation. We will examine spin echo imaging in the next chapter.

---

[9] Since water was pre-polarized before each 90-degree excitation, there was no detectable difference in the SNRs of the gradient echo image using centrally versus sequentially ordered phase-encode gradients.

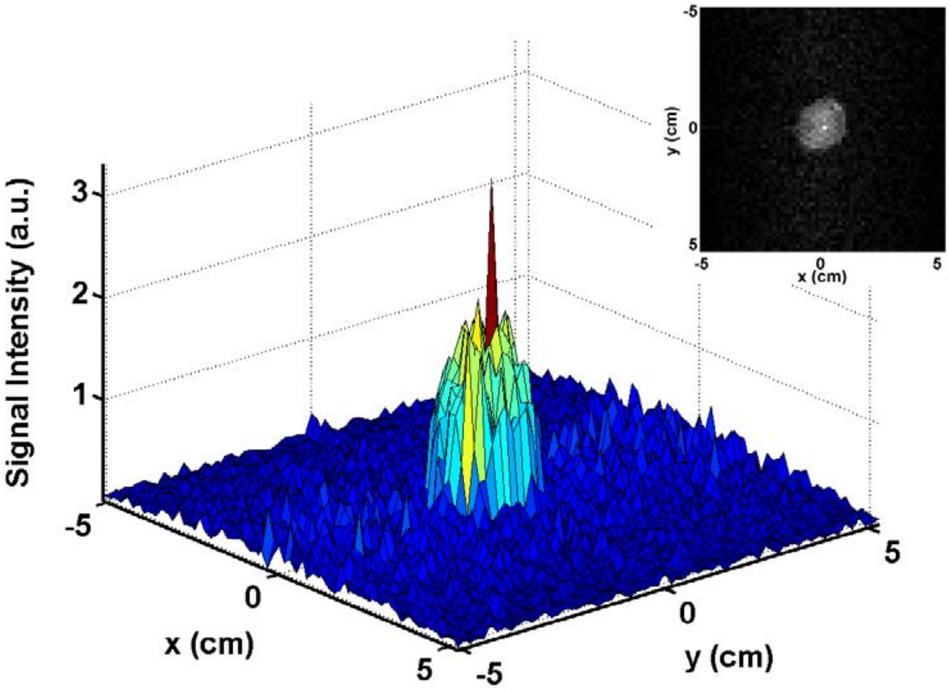

Figure 5.13: Gradient echo image of a 2.5 cm sphere filed with hyperpolarized ^{3}He obtained with **sequentially ordered** phase-encode gradients. Acq.time=4 ms, BW=8 kHz, $\alpha = 12.7°$, $FOV_x = FOV_y = 10.5$ cm, $\Delta x = \Delta y = 1.64$ mm, $t_{pump} = 2$ h, T_2^* relaxation negligible.

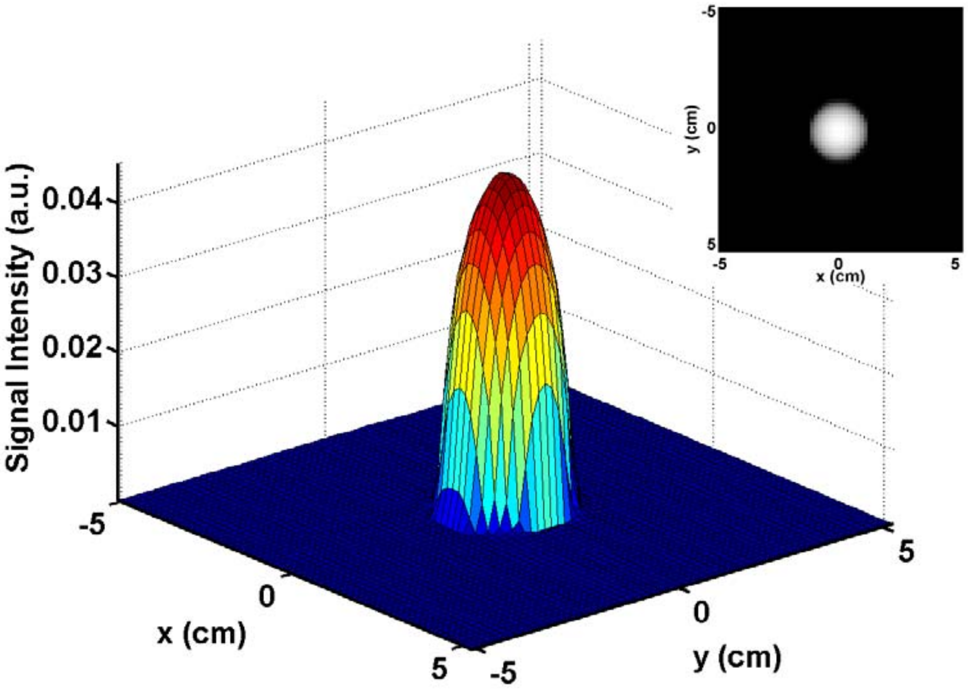

Figure 5.14: Simulation of the experiment displayed in the Figure 5.13.

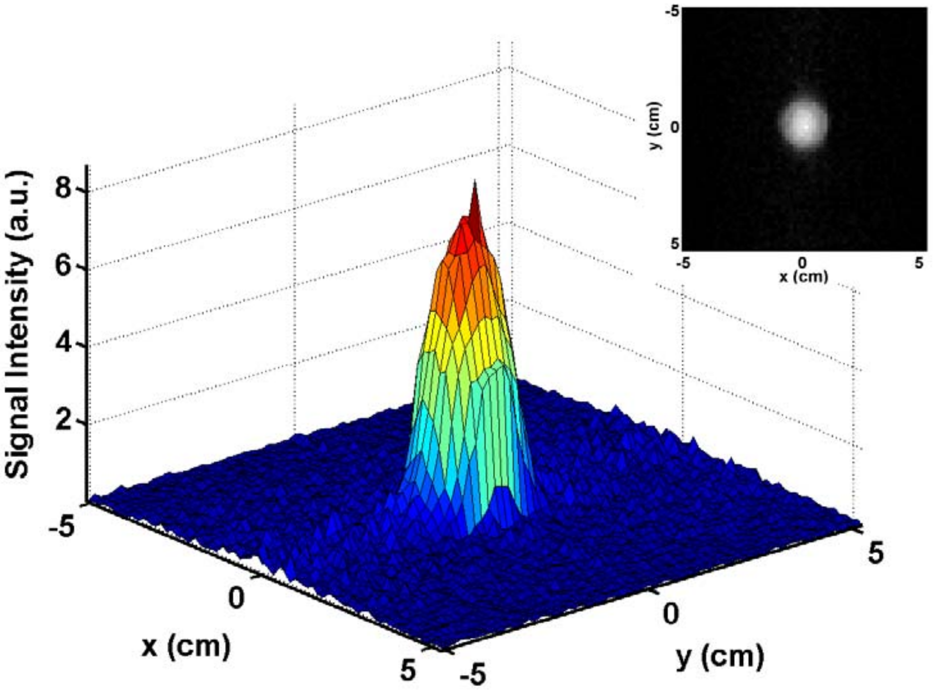

Figure 5.15: Gradient echo image of a 2.5 cm sphere filed with hyperpolarized ^{3}He obtained with **centrally ordered** phase-encode gradients. Acq.time=4 ms, BW=8 kHz, $\alpha = 12.7°$, $FOV_x = FOV_y = 10.5$ cm, $\Delta x = \Delta y = 1.64$ mm, $t_{pump} = 2$ h, T_2^* relaxation negligible.

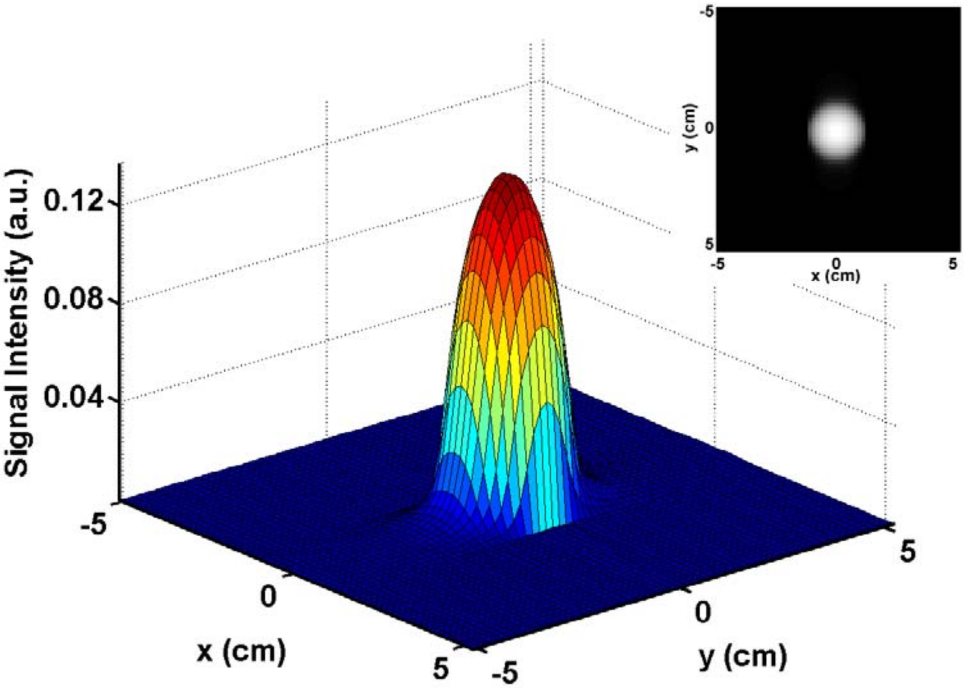

Figure 5.16: Simulation of the experiment displayed in the Figure 5.15.

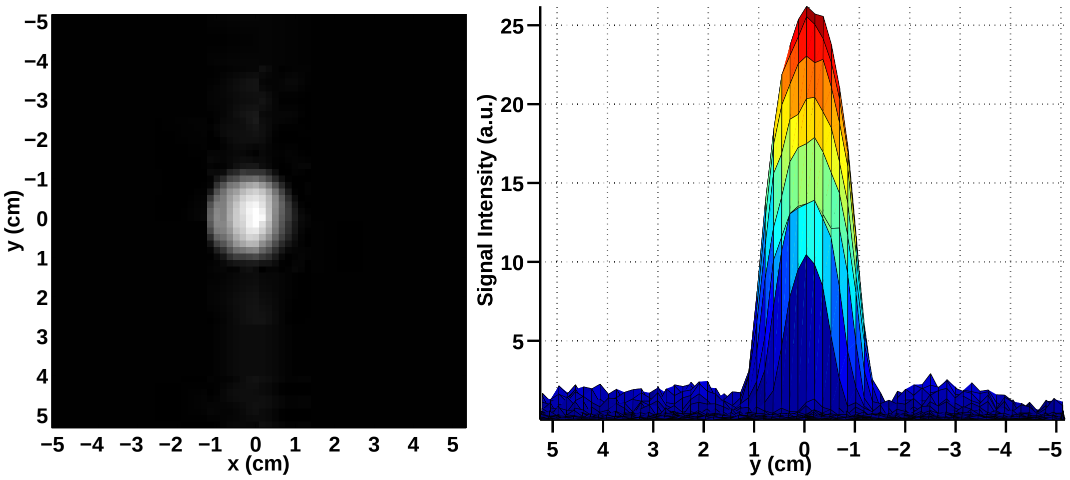

Figure 5.17: Gradient echo image (left) and projection (right) onto the y-axis of a 2.5 cm sphere filed with **hyperpolarized ^{3}He** using centrally ordered phase-encode gradients. $t_{OP} = 10$ h; $f_{RF} = 398$ kHz; $\alpha = 13°$; $\Delta x = \Delta y = 1.64$ mm; $FOV_x = FOV_y = 10.5$ cm; $T_{AcqTime} = 4$ ms; $BW = 8$ kHz; $G_x = 4.7$ mT/m; $G_y^{max} = 9.41$ mT/m.

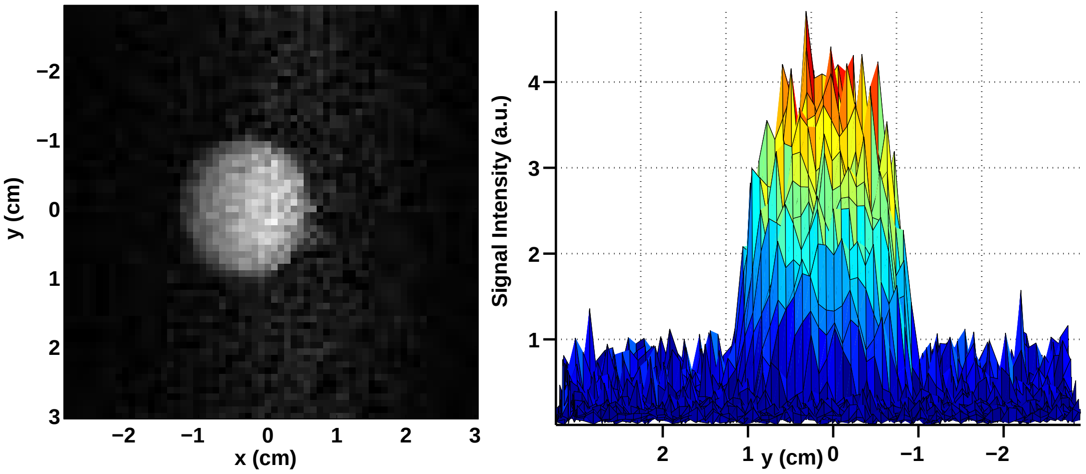

Figure 5.18: Gradient echo image (left) and projection (right) onto the y-axis of a 2.5 cm sphere filed with **doped water**. $B_p \approx 0.3$ T; $f_{RF} = 398$ kHz; $\alpha = 90°$; $\Delta x = \Delta y = 0.94$ mm; $FOV_x = FOV_y = 6$ cm; $T_{AcqTime} = 4$ ms; $BW = 8$ kHz; $G_x = 6.26$ mT/m; $G_y^{max} = 12.5$ mT/m.

5.5 Spin Echo Imaging

5.5.1 Spin Echo Pulse Sequence

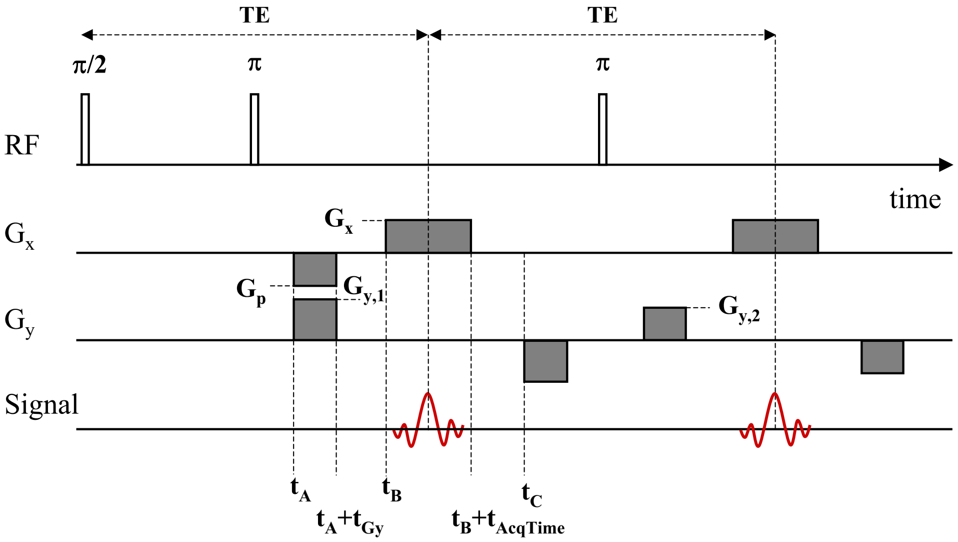

Figure 5.19: Pulse sequence used in spin echo imaging.

The spin echo imaging sequence is shown in Figure 5.19, while the k-space trajectory corresponding to this sequence in shown in Figure 5.20. The sequence is an extension of the CPMG sequence (see Figure 4.11 in Chapter 4.6) with the imaging gradients applied along the x and y direction. The spin echo occurs in the middle of the acquisition time, $t_{Acq\ Time}$, provided that the area under the negative x-gradient lobe is half the area under the positive x-gradient lobe. Unlike in the case of the gradient echo sequence, the phase-encode gradients are refocused after each acquisition to avoid error accumulation due to imperfect 180-degree pulses. An imperfect 180-degree pulse would flip only a fraction of the area under the y-gradient pulse, and consequently, the point $(k_{x,2}, k_{y,2})$ in Figure 5.20 would not map into its mirror image across the y-axis as it should. As a result, the k-space would be encoded improperly. The problem of imperfect 180-degree pulses could be avoided entirely if the k-space vector was at the origin of k-space before applying each 180-degree pulse. However, if the readout gradient was refocused in addition to the phase-encode gradients, diffusion losses might be too large. In this work, we focus exclusively on 1-D projection experiments using phase-encode gradients. The issues related to 2-D spin echo acquisition are briefly outlined in the conclusion of this chapter.

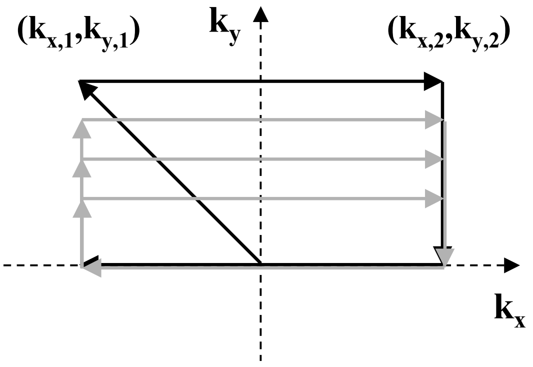

Figure 5.20: A schematic representation of k-space data collection in spin echo sequence.

5.5.2 $\boldsymbol{K}$-Space Weighting for Spin Echo Imaging

The k-space weighting for spin echo imaging can be constructed following arguments similar to the ones used when designing the k-space weighting for gradient echo imaging. Unlike in the case of gradient echo imaging, however, the initial flip-angle in the spin echo imaging is 90°, which brings all the magnetization into the transverse plane. The 180-degree pulses are then used to refocus the magnetization every TE time period. Furthermore, since the magnetization is in the transverse plane during imaging, it decays exclusively due to the transverse T_2^{CPMG} relaxation. Finally, we also need to consider diffusion losses in the imaging gradients. The k-space weighting for spin echo imaging will thus be equal to

$$\begin{aligned} w(t) &= \left(\cos^{n-1} 90\right)(\sin 90) \exp\left(-\frac{t}{T_2^{CPMG}}\right) \exp\left(-4\pi^2 D \int_0^t \{k_x^2(t') + k_y^2(t')\} dt\right) \\ &= \exp\left(-\frac{t}{T_2^{CPMG}}\right) \exp\left(-4\pi^2 D \int_0^t \{k_x^2(t') + k_y^2(t')\} dt\right). \end{aligned} \tag{5.27}$$

In the above equation, the time integral must span the entire history of the magnetization vector which is being imaged. Since spin echo imaging is performed by continuously refocusing the same magnetization vector, t should be the time from the 90-degree excitation–when the magnetization was tipped into the transverse plane. Contrast this with gradient echo imaging, where t was the time elapsed from the last RF excitation.

We can divide the decay expressed in Eq. 5.27 into the decay along the readout (i.e., x) axis and the decay along the phase-encode (i.e., y) axis. If we ignore the T_2^{CPMG} relaxation for a moment, then the decay along the readout and the phase-encode directions is entirely due to diffusion in the imaging gradients, as depicted in Figure 5.21. To find the diffusion term in Eq. 5.27 we need to express the x and y-gradients as a function of time and then integrate the gradients from the beginning of the imaging sequence to the time of interest. This procedure was performed numerically, using Matlab, as it has no simple close-form solution. Once the diffusion losses were modelled, the T_2^{CPMG} relaxation was added into the model in the form of a simple exponential decay whose time constant T_2^{CPMG} was based on the results obtained in Section 4.6. Figure 5.21 shows schematically, that the main process contributing to signal loss along the readout and phase-encode axis is diffusion.

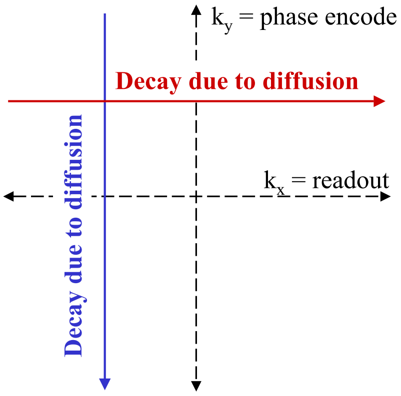

Figure 5.21: Schematic representation of signal decay during spin echo sequence. The main mechanism of signal loss in both readout and phase-encode directions is diffusion.

5.5.3 1-D Spin Echo Imaging Experiments and Simulations

Since spin echo sequences are limited by large diffusion losses in the case of hyperpolarized gases, we examine a 1-D spin echo pulse sequence, with imaging gradients applied along the y-axis only (Figure 5.19 without the G_x gradient).

5.5.3.1 Centrally and Sequentially Ordered Phase-Encode Gradients

Gradient echo imaging of ^{3}He showed that using centrally rather than sequentially ordered phase-encode gradients improved the SNR of the image by a factor of 4. It is thus reasonable to investigate the SNR gain when using centrally ordered phase-encode gradients in the spin echo imaging sequence. To study this SNR improvement, we used the Pulsed Gradient Spin

Echo sequence (PGSE) introduced in Chapter 4.7 (see Figure 4.16). If the diffusion inducing gradients are advanced according to the centric/sequential ordering schemes (Figure 5.12), they mimic the centric/sequential ordering of phase-encode gradients in the 1-D spin echo sequence. However, since the echo was acquired at $k = 0$, the frequency distribution of the object had no bearing on the size of the spin echo which was thus purely a consequence of diffusion losses accrued during $t = \Delta$. In other words, by using the PGSE sequence rather than the 1-D spin echo sequence, we were able to assess directly the k-space weighting function for pulsed bipolar gradients (Chapter 5.3.4). Figure 5.22 shows the PGSE sequence with pulsed gradients advancing in either centric or sequential order.

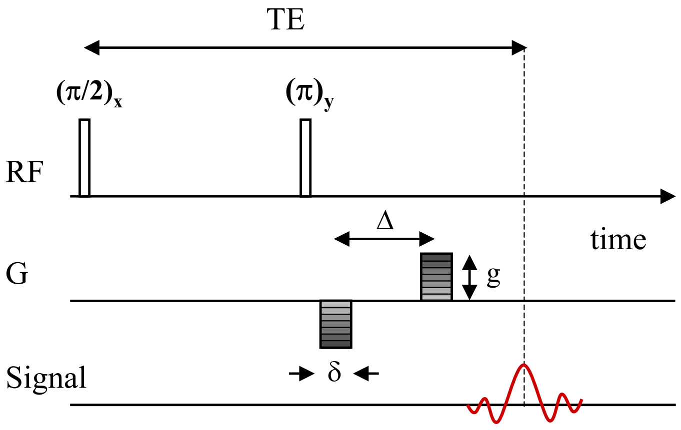

Figure 5.22: Pulsed gradient spin echo sequence.

Diffusion losses due to pulsed bipolar gradients were expressed in Chapter 4.7, Eq. 4.73. After accounting for T_2^{CPMG} relaxation losses, the k-space weighting for the nth echo is

$$w(nTE) = \exp\left[-D\, n\gamma^2 g^2 \delta^2 \left(\Delta - \frac{\delta}{3}\right) - \frac{nTE}{T_2^{CPMG}}\right]. \tag{5.28}$$

Since the gradient size g, duration δ, and separation Δ are known, while the T_2^{CPMG} relaxation time constant can be predicted from the measurements described in Section 4.8, we can directly calculate the relative magnitude of the nth echo and compare it to the experimental results.

Figure 5.23 shows experimental data and simulations of k-space weighting for ^{129}Xe as a function of k for both centrally and sequentially ordered bipolar gradients. The corre-

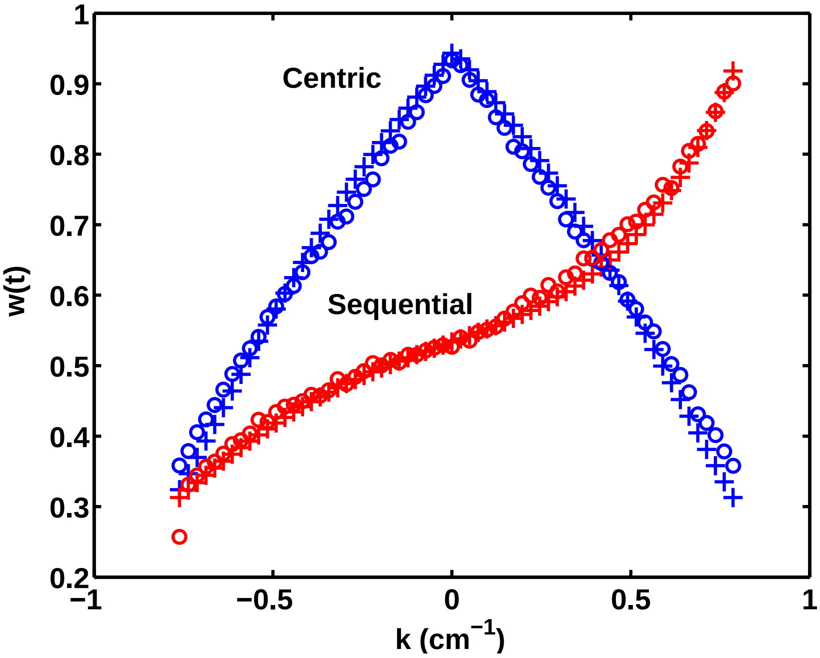

Figure 5.23: K-space weighting for ^{129}Xe using PGSE sequence with centric and sequential ordering - experimental data (circles), simulation (crosses). Predicts a ×2 SNR gain using centric ordering. T_2 used in simulation $= 6.5$ s, $g_{max} = 1.32$ mT/m, $\Delta g = 0.04$ mT/m, $\delta = 5$ ms, $\Delta = 10.36$ ms, $TE = 54.2$ ms, $\Delta y = 0.58$ cm, $FOV_y = 40.7$ cm.

spondence between the simulation and the experimental data was best when ^{129}Xe T_2^{CPMG} relaxation time constant was chosen to be 6.5 s, which is reasonable in light of data displayed in Figure 4.22. The data obtained with the centric ordering scheme (Figure 5.12, left) peaks at $k = 0$, while the sequential ordering scheme (Figure 5.12, right) peaks at the positive edge of k-space, reflecting the fact that the first line of k-space is acquired with maximum available magnetization. Furthermore, since diffusion losses are proportional to the square of k, the k-space weighting function decays slower for centric than sequential ordering scheme. For an imaging resolution of 5.6 mm, there is a factor of two improvement in the intensity of the signal at the center of k-space when using centric ordering scheme. For a higher resolution, we expect an even faster decay of magnetization because stronger gradients have to be used to reach larger k-space values.

Figure 5.24 shows a simulation of the diffusion k-space weighting for ^{129}Xe at a higher imaging resolution (2 mm). As predicted, the difference in signal intensity in the center of k-space when using centrally versus sequentially ordered bipolar pulsed gradients is very pronounced. This effect is even bigger for ^{3}He, because it has a larger diffusion constant than ^{129}Xe. Figure 5.25 shows diffusion k-space weighting for ^{3}He, for a resolution of 5 mm.

When k-space data is transformed into the image domain, the signal intensity at $k = 0$ determines the image SNR. Our experiments and simulations using PGSE pulse sequence have thus demonstrated that the SNR of the hyperpolarized gas images should improve significantly when using centrally ordered phase-encode gradients. We tested this assumption by performing 1-D imaging experiments with centric and sequential ordering schemes.

The 1-D imaging experiments were performed using only the G_y gradient in the spin echo imaging sequence, shown in Figure 5.19. Figure 5.26 shows a projection image of a sphere filled with hyperpolarized ^{3}He. Note that the image obtained with sequentially ordered phase-encode gradients has been multiplied by a factor of 50. The SNR gain in using centric ordering scheme is on the order of 100.

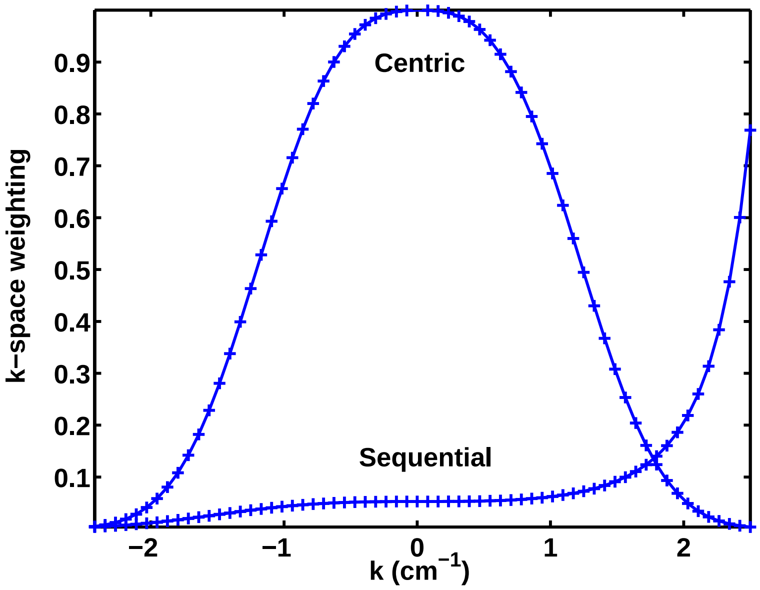

Figure 5.24: Diffusion k-space weighting–simulation for ^{129}Xe. Predicts a ×20 SNR increase for a 2 mm target resolution using centric encoding. No T_2^{CPMG} relaxation. $\Delta y = 2$ mm, $FOV_y = 12.8$ cm, $G_{max} = 4.2$ mT/m, $\Delta G = 0.13$ mT/m, $\delta = 5$ ms, $\Delta = 10$ ms, $TE = 20$ ms.

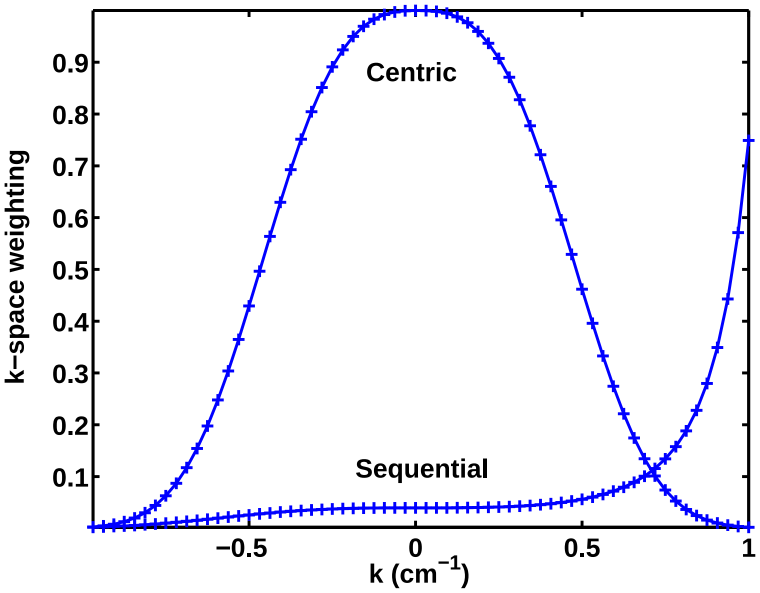

Figure 5.25: Diffusion k-space weighting–simulation for ^{3}He. Predicts a ×20 SNR increase for a 5 mm target resolution using centric encoding. No T_2^{CPMG} relaxation. $\Delta y = 5$ mm, $FOV_y = 32$ cm, $G_{max} = 1.54$ mT/m, $\Delta G = 0.05$ mT/m, $\delta = 2$ ms, $\Delta = 5$ ms, $TE = 10$ ms.

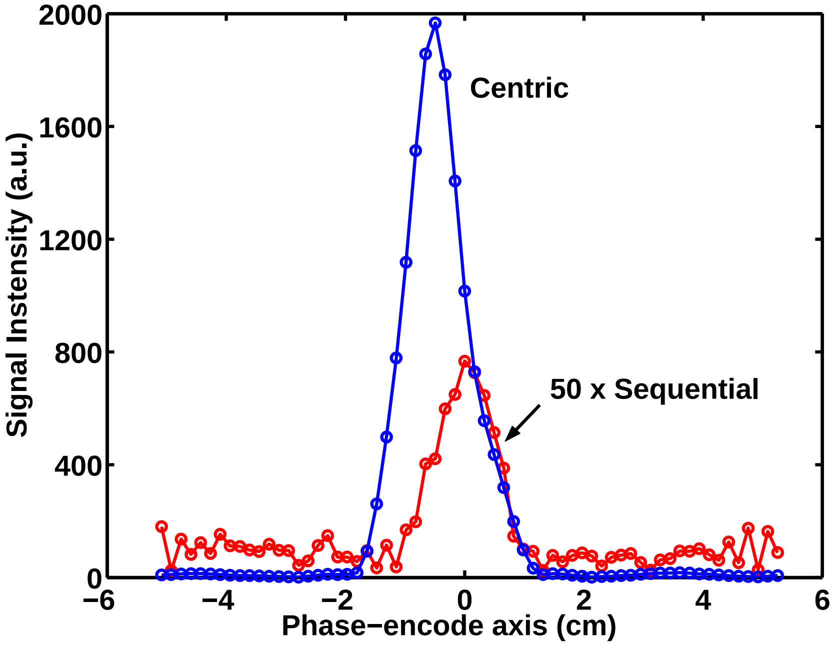

Figure 5.26: A 1-D spin echo image of a 2.5 cm sphere filled with hyperpolarized ^{3}He taken with centrally and sequentially ordered phase-encode gradients. Acquisition time = 4 ms, $FOV_y = 10.5$ cm, $\Delta y = 1.64$ mm, $G_{y,max} = 9.4$ mT/m, $\Delta G_y = 0.29$ mT/m.

5.6 Conclusions

The most commonly used sequences for imaging hyperpolarized gases are small flip-angle sequences, such as FLASH, which use a fraction of gas hyperpolarization to encode each line of k-space. These sequences are straightforward and easy to implement as they have very liberal phase requirements; however, they do not utilize all the available hyperpolarized gas magnetization.

In this work we modelled signal decay during gradient echo imaging which resulted from the flip-angle, relaxation and diffusion of the gas. We were able to determine the optimal flip-angle to avoid a non-uniform sampling of the phase-encode axis of k-space and show a factor of three improvement in the image SNR when using centrally ordered phase-encode gradients. Our gradient echo images using centric and sequential ordering scheme agreed with simulations to first order. Finally, comparing ^{3}He and water gradient echo images we find a factor of three improvement in the image SNR when using hyperpolarized ^{3}He.

Other researchers have studied in detail gradient echo imaging and the issues related to the flip-angle used. Zhao *et al.* [68] compared the quality of hyperpolarized ^{129}Xe images when using constant flip-angle (CFA) with sequential phase-encode gradients, CFA with centric phase-encode gradients, and a sequence with a variable flip-angle (VFA) which maintains a constant transverse magnetization throughout the duration of imaging. The researchers concluded that the VFA approach significantly improves the SNR of ^{129}Xe images and eliminates image artifacts which are unavoidable when using CFA with centric encoding scheme. Our images which were collected with centric ordering of phase-encode gradients and with constant flip-angle show no artifacts because of the nature of the object being imaged. A spherical object, such as our cell, contains almost no high frequency components in k-space domain.[10] Consequently, we were not affected by having a greatly depleted magnetization when collecting high frequency components in the case of centrally ordered phase-encode gradients. In the future, we would need to apply our model to a more realistic object–one that contains high frequency components. Since past research [68, 78, 95] shows an improved SNR when using variable flip-angles, it would be useful to implement the variable flip-angle algorithm on the pulsed resistive low-field scanner.

While the gradient echo sequences enabled us to obtain hyperpolarized gas images,

---

[10] This is because a sphere has no sharp edges, which would contribute high frequency components to the Fourier transform of a sphere.

the focus of our work was spin echo imaging. Single-shot CPMG spin echo sequences use all the available gas magnetization and thus offer greater SNR efficiency than small flip-angle sequences. At low magnetic field strengths at which we are operating, the gradient inhomogeneities and susceptibility effects are reduced, so the T_2 relaxation times of gases are long enough to allow for the collection of the entire k-space in a single-shot. The disadvantage is that spin echo sequences are limited by large diffusion losses in the case of hyperpolarized gases.

In this work we studied ways of minimizing diffusion losses. Since signal decay depends on the path integral over k-space, diffusion can be minimized by collecting low k-space values first. Our experimental spin echo data using a pulsed gradient spin echo sequence (PGSE) with centric and sequential ordering of phase-encode gradients agrees well with simulations and shows an improvement in the SNR when using centric ordering scheme. Finally, we collected 1-D projection spin echo images of ^{3}He. There was a factor of 100 improvement in the image SNR when using centric as opposed to sequential ordering of phase-encode gradients. However, large diffusion losses prevented us from obtaining 2DFT spin echo images.

Durand *et al.* [26, 89] used a RARE sequence for *in vivo* imaging of human lungs at low field (0.1 T). The diffusion coefficient of hyperpolarized gases in lungs is greatly reduced, because the alveolar structure of the lungs restricts gas diffusion. The apparent diffusion of ^{3}He, for instance, is around 2×10^{-5}, which is 10 times less than the unrestricted diffusion coefficient [26]. The smaller diffusion coefficient enabled the authors to obtain 2-D RARE images of human lungs. However, the authors were not able to obtain good quality cell images with the 2-D RARE sequence [26]. This fact indicates that spin echo imaging holds more promise for *in vivo* than *in vitro* imaging. The authors also concluded that the maximum resolution achievable with RARE (in the *in vivo* case) was 6 mm. However, this resolution might be surpassed, if a different phase-encoding scheme were used.

The ideal 2-D RARE sequence for low-field hyperpolarized gas imaging would be an outward sequence of rings, as described in [96] for other applications. The diffusion losses of this 2-D sequence would likely be dominated by crusher pulses, so RF-insensitive spin echo pulses [97] will be important to obviate crushers, and the increased SAR (specific absorption rate) would be well below safety limits for low-field MRI.

Chapter 6

Future Work

6.1 Hyperpolarized Gas Polarimetry

Although ^{129}Xe EPR polarimetry produced detectable EPR frequency shifts, the uncertainty associated with the shift was at least 50%. To develop ^{129}Xe EPR into a reliable polarimetry method, the following improvements have to be done:

1. The background field variation has to be reduced. To achieve an accuracy of 2%, the maximum allowable variation in the background EPR frequency–assuming a net ^{129}Xe EPR frequency shift of around 1 kHz–would be 20 Hz. Since $\gamma_{Rb} = 466.7$ kHz/G, the 20 Hz variation in ^{129}Xe EPR frequency would be produced by a variation in the background magnetic field on the order of 4×10^{-5} G. Consequently, for a holding field of 20 G, the field would have to be stable to ppm levels.

2. The intensity of Rb D2 resonance has to be increased. This could be achieved by increasing the cell's temperature during the EPR polarimetry measurement. If a temperature of 150°C instead of 80°C is used, the intensity of Rb D2 resonance may increase by a factor of around 100. However, if the higher pumping temperature significantly reduces the lifetime of hyperpolarized ^{129}Xe in the cell, then the detected Rb D2 resonance signal will have to be increased electronically (using RF amplifiers and filters).

3. The lifetime of the ^{129}Xe cell has to be improved. We speculated that the decay of the ^{129}Xe EPR signal–while the magnetization was anti-aligned with the magnetic field–was due to the poor lifetime of the cell, which caused the magnetization to decay towards its thermal equilibrium along the magnetic field axis. If the lifetime

of the cell is improved to 10 min, then the magnetization may take around 7 min ($\ln 2/0.1$ s) before decaying to zero. An EPR frequency shift measurement could easily be performed in that time frame.

A side note: The fact that the laser is pumping in the opposite direction while the gas is anti-aligned with the field becomes important only when $\gamma_{SE} \approx \Gamma$. For ^{129}Xe, $\gamma_{SE} \approx 10^{-4}$ s^{-1} at 90°C, so the lifetime of the cell would have to be around 2.8 h before the polarization of laser light during the AFP flip starts to matter.

6.2 Hyperpolarized Gas Imaging

While the uncertainty in the extrapolated ^{129}Xe T_2 relaxation times was only a few percent, the uncertainty in ^{3}He T_2 relaxation times was around 20%. To reduce the uncertainty in ^{3}He T_2 relaxation times, more measurements of ^{3}He T_2^{CPMG} relaxation should be performed, especially for the interecho times up to 30 ms. During these measurements, special care will have to be taken to eliminate the possibility of gas flow inside the cell (e.g., wait until cell cools to room temperature before collecting the data).

While our theoretical as well as experimental results show a significant improvement in the SNR of the image when using central ordering of phase-encode gradients, this might no longer be the case when imaging an object containing high-frequency components. Our model of diffusion-induced losses should thus be applied to, and tested on, an object with sharp edges (such as a cylindrically-shaped cell).

To obtain a 2-D spin echo image of hyperpolarized gas, diffusion-induced losses have to be minimized. This can be achieved by constructing a pulse sequence which collects central k-space data first (such as a progression of concentric circles) or/and by increasing the strength (while reducing the duration) of the imaging gradients. Note that the magnetic field gradients cannot be increased pass the point at which the concomitant terms start to dominate over the holding magnetic field. When imaging at low magnetic field strengths, this limiting gradient strength might easily be reached. Alternatively, we can conclude that the need for stronger imaging gradients increases the ideal imaging field strength. On the other hand, diffusion losses in the background gradients are reduced at smaller imaging field values. Therefore, the need for smaller background inhomogeneities decreases the ideal imaging field strength. It is therefore worth investigating whether the two opposing requirements converge to a single field strength. If so, it would also be worthwhile to compare this limiting field strength with the field strength at which the body-noise starts to dominate over the coil-noise (for a specific coil), which is the ideal field strength from the SNR perspective.

Appendix A

Theoretical Estimation of Diffusion Coefficients for Binary Gas Mixtures

The diffusion coefficient D_{12} for the isothermal diffusion of *species 1* through constant-pressure binary mixture of *species 1* and *2* is defined by the relation

$$J_1 = -D_{12} \nabla c_1, \tag{A.1}$$

where J_1 is the flux of *species 1* and c_1 is the concentration of the diffusing species.

Mutual-diffusion, defined by the coefficient D_{12}, can be viewed as diffusion of *species 1* at infinite dilution through *species 2*, or equivalently, diffusion of *species 2* at infinite dilution through *species 2*. **Self-diffusion**, defined by the coefficient D_{11}, is the diffusion of a substance through itself.

There are different theoretical models for computing the mutual (self) diffusion coefficient of gases. For non-polar molecules, Lennard-Jones potentials provide a basis for computing diffusion coefficients of binary gas mixtures [30]. The mutual diffusion coefficient, in units of cm^2/s is defined as

$$D_{12} = 0.001858 \; T^{3/2} \sqrt{\frac{M_1 + M_2}{M_1 M_2}} \frac{f_D}{p \sigma_{12}^2 \Omega_D}, \tag{A.2}$$

where T is temperature of the gas in units of Kelvin; M_1 and M_2 are molecular weights of *species 1* and *2*; p is the total pressure of the binary mixture in units of atmospheres; f_D is the second-order correction, usually between 1.00 and 1.03; σ_{12} is the Lennard-Jones force constant for the gas mixture, defined by $\sigma_{12} = 1/2\,(\sigma_1 + \sigma_2)$; Ω_D is the collision integral defined by

$$\Omega_D = \frac{1.06036}{(T^*)^{0.15610}} + \frac{0.19300}{\exp\left(0.47635\ T^*\right)} + \frac{1.03587}{\exp\left(1.52996\ T^*\right)} + \frac{1.76474}{\exp\left(3.89411\ T^*\right)}, \qquad \text{(A.3)}$$

where $T^* \equiv kT/\epsilon_{o12}$, k is the Boltzman gas constant, $\epsilon_{o12} = (\epsilon_{o1}\epsilon_{o2})^{1/2}$ and $\epsilon_{o12} = \sqrt{\epsilon_{o1}\epsilon_{o2}}$.

Values of $\sigma_{1(2)}$, Ω_D and $\epsilon_{o1(2)}$ are tabulated for most naturally occurring gases [30].

The self-diffusion coefficient of a gas can be obtained from Eq. A.2, by observing that for a one-gas system: $M_1 = M_2 = M$, $\epsilon_{o1} = \epsilon_{o2}$ and $\sigma_1 = \sigma_2$. Thus,

$$D_{11} = 0.001858\ T^{3/2}\sqrt{\frac{2}{M}}\frac{f_D}{p\sigma_{11}^2\Omega_D}. \qquad \text{(A.4)}$$

It is useful to define **observable diffusion**, D_{obs}, which is diffusion that one observes in an experiment. Observable diffusion os *species 1* in the binary mixture of *species 1* and *species 2* is

$$\begin{aligned} \frac{1}{D_{obs,1}} &= \frac{p_1/\left(p_1+p_2\right)}{D_{11}(p=1atm)/\left(p_1+p_2\right)} + \frac{p_2/\left(p_1+p_2\right)}{D_{12}(p=1atm)/\left(p_1+p_2\right)} \\ &= \frac{p_1}{D_{11}(p=1atm)} + \frac{p_2}{D_{12}(p=1atm)} \\ &= \frac{1}{D_{11}(p=p_1)} + \frac{1}{D_{12}(p=p_2)}. \qquad \text{(A.5)} \end{aligned}$$

Equation A.5 has a simple physical explanation when applied to gases. The observable diffusion rate of gas *1* in the mixture of gases *1* and *2* is equal to the diffusion rate of one atom of gas *1* through the rest of atoms of gas *1*, plus the diffusion rate of one atom of gas *1* through the atoms of gas *2*. Equation A.5 enables the estimation of the diffusion coefficient for the binary mixture of ^{129}Xe-nitrogen and ^{3}He-nitrogen.

A.0.1 Observable Diffusion Constant for a Mixture of Xe-129 and Nitrogen

The relevant parameters [30] are:

$$\sigma_{Xe} = 4.047 \quad \epsilon_{\circ Xe}/k = 231.0 \quad M_{Xe} = 130.4$$
$$\sigma_{N2} = 3.798 \quad \epsilon_{\circ N2}/k = 71.4 \quad M_{N2} = 28$$

At $T = (303 \pm 10)$ K and $p = (p_{Xe} + p_{N2})$ atm,

$$\begin{array}{llll} \sigma_{Xe-N2} = 3.9225 & \frac{\epsilon_{\circ Xe-N2}}{k} = 128.42 & \frac{kT}{\epsilon_{\circ Xe-N2}} = 2.398 & \Omega_D = 1.0183 \\ \sigma_{Xe-Xe} = 4.047 & \frac{\epsilon_{\circ Xe-Xe}}{k} = 231 & \frac{kT}{\epsilon_{\circ Xe-Xe}} = 1.333 & \Omega_D = 1.2696. \end{array} \tag{A.6}$$

The above parameter values yield

$$D_{Xe-N2} = \frac{0.1303 \times 10^{-4}}{(p_{Xe} + p_{N2})} \text{ m}^2/\text{s} \tag{A.7}$$
$$D_{Xe-Xe} = \frac{0.0584 \times 10^{-4}}{(p_{Xe} + p_{N2})} \text{ m}^2/\text{s}. \tag{A.8}$$

The observable diffusion rate for a mixture of ^{129}Xe and Nitrogen gas is therefore

$$\frac{1}{D_{obs}} = \frac{p_{Xe}}{0.0584 \times 10^{-4} \text{ m}^2/\text{s}} + \frac{p_{N2}}{0.1303 \times 10^{-4} \text{ m}^2/\text{s}}. \tag{A.9}$$

The cell used in Xenon experiments had the following pressures: $p_{Xe} = (0.48 \pm 0.01)$ atm and $p_{N2} = (0.14 \pm 0.01)$ atm. The theoretical estimation of the observable diffusion constant is thus $D_{obs} = (1.08 \pm 0.08) \times 10^{-5}$ m^2/s.

A.0.2 Observable Diffusion Constant for a Mixture of He-3 and Nitrogen

The relevant parameters [30] are:

$$\sigma_{He} = 2.551 \quad \epsilon_{\circ He}/k = 10.22 \quad M_{He} = 4$$
$$\sigma_{N2} = 3.798 \quad \epsilon_{\circ N2}/k = 71.4 \quad M_{N2} = 28$$

At $T = (308 \pm 10)$ K and $p = (p_{He} + p_{N2})$ atm,

$$\begin{array}{llll} \sigma_{He-N2} = 3.1745 & \frac{\epsilon_{\circ He-N2}}{k} = 27.013 & \frac{kT}{\epsilon_{\circ He-N2}} = 11.587 & \Omega_D = 0.7260 \\ \sigma_{He-He} = 2.551 & \frac{\epsilon_{\circ He-He}}{k} = 10.22 & \frac{kT}{\epsilon_{\circ He-He}} = 30.626 & \Omega_D = 0.6231. \end{array} \tag{A.10}$$

The above parameter values yield

$$D_{He-N2} = \frac{0.7337 \times 10^{-4}}{(p_{He} + p_{N2})} \text{ m}^2/\text{s} \tag{A.11}$$
$$D_{He-He} = \frac{1.7513 \times 10^{-4}}{(p_{He} + p_{N2})} \text{ m}^2/\text{s}. \tag{A.12}$$

The observable diffusion rate for a mixture of ^{3}He and Nitrogen gas is therefore

$$\frac{1}{D_{obs}} = \frac{p_{He}}{1.7513 \times 10^{-4} \text{ m}^2/\text{s}} + \frac{p_{N2}}{0.7337 \times 10^{-4} \text{ m}^2/\text{s}}. \tag{A.13}$$

The cell used in Helium experiments had the following pressures: $p_{He} = (0.75 \pm 0.01)$ atm and $p_{N2} = (0.10 \pm 0.01)$ atm. The theoretical estimation of the observable diffusion constant is thus $D_{obs} = (1.77 \pm 0.12) \times 10^{-4}$ m^2/s.

Appendix B

Supplement on Fourier Transforms

The Fourier Transform of $e^{-2\pi k_\circ |x|}$, where $2\pi k_\circ = 1/T_2^*$, is given by:

$$\begin{aligned}
F\left[e^{-2\pi k_\circ |x|}\right] &= \int_{-\infty}^{\infty} e^{-2\pi k_\circ |x|} e^{-2\pi i k x} dx \\
&= \int_{-\infty}^{0} e^{-2\pi i k x} e^{2\pi k_\circ x} dx + \int_{0}^{\infty} e^{-2\pi i k x} e^{-2\pi k_\circ x} dx \\
&= \int_{-\infty}^{0} \left[\cos(2\pi k x) - i \sin(2\pi k x)\right] e^{2\pi k_\circ x} dx \\
&\quad + \int_{0}^{\infty} \left[\cos(2\pi k x) - i \sin(2\pi k x)\right] e^{-2\pi k_\circ x} dx
\end{aligned}$$

Let $u \equiv -x$ so that $du = -dx$, then:

$$\begin{aligned}
F\left[e^{-2\pi k_\circ |x|}\right] &= \int_{0}^{\infty} \left[\cos(2\pi k u) + i \sin(2\pi k u)\right] e^{-2\pi k_\circ u} du \\
&\quad + \int_{0}^{\infty} \left[\cos(2\pi k u) - i \sin(2\pi k u)\right] e^{-2\pi k_\circ u} du \\
&= 2 \int_{0}^{\infty} \cos(2\pi k u) e^{-2\pi k_\circ u} du \\
&= \frac{1}{\pi} \frac{k_\circ}{k^2 + k_\circ^2},
\end{aligned}$$

which is a Lorentzian function, with: $\text{FWHM} = 2k_\circ = 1/\pi T_2^*$.

Appendix C

Imaging Parameters

The following are the descriptions of some of the most common parameters in MR imaging:

1. **Bandwidth** (BW): Anti-aliasing filter bandwidth of the receiver.
2. **Sampling Period** (Δt): Sampling period of the A/D converters.
3. **Acquisition Time or Readout Interval** ($T_{AcqTime}$): Time interval during which the signal is acquired.
4. **Field-of-View** (FOV_x, FOV_y): Image size along the x and y-coordinates.
5. **Matrix Size** ($N_x \times N_y$): Number of pixels along the readout and phase-encode directions.
6. **Spatial Resolution** (Δx, Δy): Resolution in image space.
7. **Raw Data Resolution** (Δk_x, Δk_y): Resolution in k-space.
8. **Readout Amplitude** (G_x): Amplitude of the readout gradient.
9. **Maximum Amplitude in Y-Gradient** (G_y^{max}): Maximum amplitude of y-gradient used in imaging.
10. **Incremental Amplitude in Y-Gradient** (ΔG_y): Incremental amplitude of y-gradient used in imaging.
11. **Phase Encode Interval** (t_{Gy}): Time interval during which the phase encode gradient is applied.

Below, is a set of formulas which define and connect these parameters:

$$\begin{aligned}
\Delta t &= 1/BW && \text{(C.1)}\\
T_{AcqTime} &= \Delta t * N_x && \text{(C.2)}\\
G_y^{max} &= \Delta G_y * N_y && \text{(C.3)}\\
FOV_x &= 1/\Delta k_x && \text{(C.4)}\\
FOV_y &= 1/\Delta k_y && \text{(C.5)}\\
\Delta x &= FOV_x/N_x && \text{(C.6)}\\
\Delta y &= FOV_y/N_y && \text{(C.7)}\\
\Delta k_x &= \frac{\gamma}{2\pi}\, G_x\, \Delta t && \text{(C.8)}\\
\Delta k_y &= \frac{\gamma}{2\pi}\, \Delta G_y\, t_{Gy} && \text{(C.9)}
\end{aligned}$$

C.1 Bibliography

[1] W. Happer. *Reviews of Modern Physics*, 44(2):169–249, 1972.

[2] H. L. Middleton. PhD thesis, Princeton University, 1994.

[3] M. V. Romalis and G. D. Cates. *Physical Review A*, 58(4):3004–3011, 1998.

[4] N. R. Newbury, A. S. Barton, P. Bogorad, et al. *Physical Review A*, 48(1):558–568, 1993.

[5] S. R. Schaefer, G. D. Cates, T.-R. Chien, et al. *Physical Review A*, 39(11):5613–5623, 1989.

[6] T. E. Chupp and S. D. Swanson, 2000. Internet Article.

[7] M. S. Albert and D. Balamore. *Nuclear Instruments and Methods in Physics Research Section A–Accelerators Spectrometers Detectors and Associated Equipment*, 402(2-3):441–453, 1998.

[8] D. Guenther, G. Hanisch, and H.-U. Kauczor. *Acta Radiologica*, 41:519–528, 2000.

[9] E. E. De Lange, J. P. I. Mugler, J. R. Brookeman, et al. *Radiology*, 210:851–857, 1999.

[10] J. X. Chen, L. W. Hedlund, H. E. Moller, et al. *Proceedings of the National Academy of Sciences*, 97(21):11478–11481, 1999.

[11] T. A. Altes, P. L. Powers, J. Knight-Scott, et al. *Journal of Magnetic Resonance Imaging*, 13:378–384, 2001.

[12] L. F. Donnelly, J. R. MacFall, P. H. McAdams, et al. *Radiology*, 212(3):885–889, 1999.

[13] A. J. Deninger, B. Eberle, M. Ebert, et al. *NMR in Biomedicine*, 13(4):194–201, 2000.

[14] E. W. Hughes and R. Voss. *Annual Review of Nuclear and Particle Science*, 49:303–339, 1999.

[15] K. Abe, T. Akagi, B. D. Anderson, et al. *Physical Review Letters*, 79(1):26–30, 1997.

[16] M. S. Albert, G. D. Cates, B. Driehuys, et al. *Nature*, 370:199–201, 1994.

[17] W. Happer, E. Miron, S. R. Schaefer, et al. *Physical Review A*, 29(6):3092–3110, 1984.

[18] S. Appelt, B.-A. A. Baranga, C. J. Erickson, et al. *Physical Review A*, 58(2):1412–1439, 1998.

[19] T. G. Walker and W. Happer. *Reviews of Modern Physics*, 69(2):629–642, 1997.

[20] B. A. Chronik, R. D. Venook, S. M. Conolly, et al. In *Proc. Intl. Soc. Mag. Reson. Med.*, volume 10, page 58, Honolulu, Hawaii, USA, 2002.

[21] G. P. Wong, C. H. Tseng, V. R. Pomeroy, et al. *Journal of Magnetic Resonance*, 141:217–227, 1999.

[22] D. I. Hoult and P. C. Lauterbur. *Journal of Magnetic Resonance*, 34:425–433, 1979.

[23] D. I. Hoult and R. E. Richards. *Journal of Magnetic Resonance*, 24:71–85, 1976.

[24] P. Morgan, S. Conolly, G. Scott, et al. *Magnetic Resonance in Medicine*, 36(4):527–536, 1996.

[25] G. Scott, B. Chronik, N. Matter, et al. In *Proc. Intl. Soc. Mag. Reson. Med.*, volume 9, page 610, Glasgow, Scotland, UK, 2001.

[26] E. Durand, G. Guillot, L. Darrasse, et al. *Magnetic Resonance in Medicine*, 47:75–81, 2002.

[27] J. P. I. Mugler, M. Salerno, E. E. De Lange, et al. In *Proc. Intl. Soc. Mag. Reson. Med.*, volume 10, page 2019, Honolulu, Hawaii, USA, 2002.

[28] C. J. McGloin, A. Benattayallah, R. W. Bowtell, et al. In *Proc. Intl. Soc. Mag. Reson. Med.*, volume 9, page 947, Glasgow, Scotland, UK, 2001.

[29] B. Cowan. *Nuclear Magnetic Resonance and Relaxation*. Cambridge University Press, 1997.

[30] R. C. Reid and T. K. Sherwood. *The Properties of Gases and Liquids*, pages 2nd ed: 520–543, 632–633 4th ed: 577–597. McGraw-Hill Book Company, 1966, 1987.

[31] A. Kastler. *Proceedings of the Physical Society of London Section A*, 67(418):853–863, 1954.

[32] W. B. Hawkins. *Physical Review*, 98(2):478–486, 1955.

[33] H. G. Dehmelt. *Physical Review*, 105(5):1487–1489, 1957.

[34] M. A. Bouchiat, T. R. Carver, and C. M. Varnum. *Physical Review Letters*, 5(8):373–375, 1960.

[35] B. C. Grover. *Physical Review Letters*, 40(6):391–392, 1978.

[36] W. Happer and A. C. Tam. *Physical Review A*, 16(5):1877–1891, 1977.

[37] W. Happer and W. A. Van Wijngaarden. *Hyperfine Interactions*, 38:435–470, 1987.

[38] H. Middleton, R. D. Black, B. Saam, et al. *Magnetic Resonance in Medicine*, 33:271–275, 1995.

[39] J. X. Chen, M. S. Chawla, L. W. Hedlund, et al. *Magnetic Resonance in Medicine*, 39:79–84, 1998.

[40] Y.-Q. Song, H. C. Gaede, T. Pietrass, et al. *Journal of Magnetic Resonance, Series A*, 115:127–130, 1995.

[41] A. Bifone, Y.-Q. Song, R. Seydoux, et al. *Proceedings of the National Academy of Sciences USA*, 93:12932–12936, 1996.

[42] M. S. Albert, D. F. Kacher, D. Balamore, et al. *Journal of Magnetic Resonance*, 140:264–273, 1999.

[43] S. D. Swanson, M. S. Rosen, B. W. Agranoff, et al. *Magnetic Resonance in Medicine*, 38:695–698, 1997.

[44] B. Driehuys, G. D. Cates, E. Miron, et al. *Applied Physics Letters*, 69(12):1668–1670, 1996.

[45] U. Ruth, T. Hof, J. Schmidt, et al. *Applied Physics B*, 68:93–97, 1999.

[46] M. S. Rosen, T. E. Chupp, K. P. Coulter, et al. *Review of Scientific Instruments*, 70(2):1546–1552, 1999.

[47] L. Darrasse, G. Guillot, P. J. Nacher, et al. *C. R. Acad. Sci. Paris, Physique appliquee*, 324(Serie II b):691–700, 1997.

[48] E. Fukushima and S. B. W. Roeder. *Experimental Pulse NMR, A Nuts and Bolts Approach.* Perseus Books, Reading, Massachusetts, 1981.

[49] F. Xiong, D. Dutta, W. Xu, et al. *Physical Review Letters*, 8724(24):art. no.–242501, 2001.

[50] W. Xu, D. Dutta, F. Xiong, et al. *Physical Review Letters*, 85(14):2900–2904, 2000.

[51] W. Xu, B. Anderson, L. Auberbach, et al. *Physical Review C*, 67(1):art. no.–012201, 2003.

[52] M. Amarian, L. Auerbach, T. Averett, et al. *Physical Review Letters*, 89(24):art. no.–242301, 2002.

[53] M. V. Romalis. PhD thesis, Princeton University, 1997.

[54] J. S. Jensen. PhD thesis, California Institute of Technology, 2000.

[55] M. E. Wagshul and T. E. Chupp. *Physical Review A*, 49(5):3854–3869, 1994.

[56] B.-A. A. Baranga, S. Appelt, M. V. Romalis, et al. *Physical Review Letters*, 80(13):2801–2804, 1998.

[57] G. D. Cates, R. J. Fitzgerald, A. S. Barton, et al. *Physical Review A*, 45(7):4631–4639, 1992.

[58] Y. Y. Jau, N. N. Kuzma, and W. Happer. *Physical Review A*, 66(5):art. no.–052710, 2002.

[59] P. T. Callaghan. *Principles of Nuclear Magnetic Resonance Microscopy.* Clarendon Press, Oxford University Press, 1991.

[60] A. S. Barton, N. R. Newbury, G. D. Cates, et al. *Physical Review A*, 49(4):2766–2770, 1994.

[61] G. K. Woodgate. *Elementary Atomic Structure.* Oxford University Press, Oxford, UK, 1989.

[62] A. Macovski and S. Conolly. *Magnetic Resonance in Medicine*, 30(2):221–230, 1993.

[63] S. E. Ungersma, B. Chronik, A. Macovski, et al. In *Proc. Intl. Soc. Mag. Reson. Med.*, volume 10, page 616, Honolulu, Hawaii, USA, 2002.

[64] S. Conolly, R. Brown, and A. Macovski. In *Proc. Intl. Soc. Mag. Reson. Med.*, volume 3, Nice, France, 1995.

[65] N. I. Matter, S. M. Conolly, A. Macovski, et al. In *Proc. Intl. Soc. Mag. Reson. Med.*, volume 8, page 1152, Denver, Colorado, USA, 2000.

[66] S. Conolly, N. I. Matter, G. Scott, et al. In *Proc. Intl. Soc. Mag. Reson. Med.*, volume 7, page 473, Philadelphia, Pennsylvania, USA, 1999.

[67] T. Pavlin, A. B. Chronik, M. S. Conolly, et al. In *Proc. Intl. Soc. Mag. Reson. Med.*, volume 10, page 2008, Honolulu, Hawaii, USA, 2002.

[68] L. Zhao, R. Mulkern, C.-H. Tseng, et al. *Journal of Magnetic Resonance, series B*, 113:179–183, 1996.

[69] H. Y. Carr and E. M. Purcell. *Physical Review*, 94:630–638, 1954.

[70] S. Meiboom and D. Gill. *Review of Scientific Instruments*, 29(8):688–691, 1958.

[71] L. Darrasse, G. Guillot, P. J. Nacher, et al. In *Proc. Intl. Soc. Mag. Reson. Med.*, volume 5, page 308, Vancouver, British Columbia, Canada, 1997.

[72] L. Darrasse, G. Guillot, P. J. Nacher, et al. In *Proc. Intl. Soc. Mag. Reson. Med.*, volume 6, page 449, Sydney, Australia, 1998.

[73] R. W. Mair, D. Hoffmann, S. A. Sheth, et al. *NMR in Biomedicine*, 13(4):229–233, 2000.

[74] G. Santyr, G. Wilson, P. Sevigny, et al. In *Hyperpolarized Gases in Magnetic Resonance: Biomedical Investigations and Clinical Applications*, page B43, Les Houshes. France, 1999. European Radiology.

[75] A. K. Venkatesh, L. V. Kubatina, A. X. Zhang, et al. In *Proc. Intl. Soc. Mag. Reson. Med.*, volume 8, page 2189, Denver, Colorado, USA, 2000.

[76] L. Zhao, R. Mulkern, C.-H. Tseng, et al. In *Proc. Intl. Soc. Mag. Reson. Med.*, volume 5, page 2106, Vancouver, British Columbia, Canada, 1997.

[77] L. Zhao, R. Mulkern, A. Venkatesh, et al. In *Proc. Intl. Soc. Mag. Reson. Med.*, volume 6, page 451, Sydney, Australia, 1998.

[78] B. R. Patyal, J.-H. Gao, R. F. Williams, et al. *Journal of Magnetic Resonance*, 126:58–65, 1997.

[79] M. Bock. *Magnetic Resonance in Medicine*, 38(6):890–895, 1997.

[80] D. M. Schmidt, J. S. George, S. I. Penttila, et al. *Journal of Magnetic Resonance*, 129(2):184–187, 1997.

[81] J. Wolber, S. J. Doran, M. O. Leach, et al. *Chemical Physics Letters*, 296:391–396, 1998.

[82] S. Peled, C.-H. Tseng, A. A. Sodickson, et al. *Journal of Magnetic Resonance*, 140:320–324, 1999.

[83] R. W. Mair, D. G. Cory, S. Peled, et al. *Journal of Magnetic Resonance*, 135:478–486, 1998.

[84] M. C. Piton, R. G. Gilbert, B. E. Chapman, et al. *Macromolecules*, 26:4472–4477, 1993.

[85] G. Strang. *Linear Algebra and Its Applications*. Harcourt Brace Jovanovich, San Diego, third edition edition, 1988.

[86] M. Pfeffer and O. Lutz. *Journal of Magnetic Resonance Series A*, 108(1):106–109, 1994.

[87] K. D. Hagspiel, T. A. Altes, J. P. I. Mugler, et al. *Magnetic Resonance in Medicine*, 44:813–816, 2000.

[88] A. G. Johnson, G. P. Cofer, L. W. Hedlund, et al. *Magnetic Resonance in Medicine*, 45:365–370, 2001.

[89] E. Durand, G. Guillot, L. Darrasse, et al. In *Proc. Intl. Soc. Mag. Reson. Med.*, volume 8, page 2184, Denver, Colorado, USA, 2000.

[90] C. H. Tseng, G. P. Wong, V. R. Pomeroy, et al. *Physical Review Letters*, 81(17):3785–3788, 1998.

[91] M. P. Augustine, A. Wong-Foy, J. L. Yarger, et al. *Applied Physics Letters*, 72(15):1908–1910, 1998.

[92] W. Shao, G. Wang, R. Fuzesy, et al. *Applied Physics Letters*, 80(11):2032–2034, 2002.

[93] L. Zhao and M. S. Albert. *Nuclear Instruments and Methods in Physics Research Section A–Accelerators Spectrometers Detectors and Associated Equipment*, 402(2-3):454–460, 1998.

[94] R. N. Bracewell. *The Fourier Transform and Its Applications.* McGraw-Hill series in electrical and computer engineering. Circuits and systems. McGraw Hill, Boston, 3rd edition, 2000.

[95] K. Markstaller, B. Eberle, W. G. Schreiber, et al. *NMR in Biomedicine*, 13(4):190–193, 2000.

[96] W. Block, J. Pauly, and D. Nishimura. *Magnetic Resonance in Medicine*, 37(4):582–590, 1997.

[97] S. Conolly, G. Glover, D. Nishimura, et al. *Magnetic Resonance in Medicine*, 18(1):28–38, 1991.